Doctoral Dissertation
Doctoral Program in Materials Science and Technology (34th Cycle)

Mesoporous Silica Spheres as drug carrier for wound treatment

By

Sara Saber Younes Mohamed

******

Supervisor(s):
Prof. Barbara Onida, Supervisor
Prof. Mauro Banchero, Co-Supervisor

Politecnico di Torino
2022

Declaration

I hereby declare that the contents and organization of this dissertation constitute my own original work and does not compromise in any way the rights of third parties, including those relating to the security of personal data.

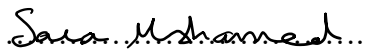

Sara Saber Younes Mohamed

Turin, 2022

* This dissertation is presented in partial fulfillment of the requirements for **Ph.D. degree** in the Graduate School of Politecnico di Torino (ScuDo).

Alla mia famiglia,
per il suo amore e incoraggiamento.

إلى عائلتي،
من أجل حبهم و تشجيعهم.

"Nella vita non bisogna mai rassegnarsi, arrendersi alla mediocrità,
bensì uscire da quella zona grigia in cui tutto è abitudine e rassegnazione passiva,
bisogna coltivare il coraggio di ribellarsi"
Rita Levi Montalcini

Acknowledgment

I would like to express my sincere gratitude to my supervisor Prof. Barbara Onida. Her continuous support, guidance and knowledge in the field of materials science have made this an amazing experience for me.

I would like to thank my co-supervisor Prof. Mauro Banchero for his insightful comments and suggestions.

Moreover, I would like to extend my thanks to all the members of the SMAC group, Prof. Silvia Ronchetti and Prof. Luigi Manna, for their assistance throughout my PhD project.

I would like to extend my sincere thanks to Prof. Marco Armandi for his technical support at every stage of the research work.

I would like to acknowledge Prof. Roberta Cavalli and her group for their contribution in the biological investigations.

My sincere thanks go to all my colleagues, Alberto, Marta and Paolo, for the nice moments spent together.

Abstract

Wound healing is a physiological process that is necessary to restore skin integrity. It is a complex and dynamic process, which involves various components such as cells, growth factors, and proteins; generally, it is divided into four overlapping phases: hemostasis, inflammatory, proliferative, and remodeling. Once the process is completed a healthy tissue should be obtained. However, in some cases, due to the presence of underlying conditions (such as diabetes, vasculitis and bacterial infection), the formation of a chronic non healed wound could be observed. Chronic wounds not only impair the physiological functions of the skin barrier, but they can also lead to sever consequences such as infections, amputations or even death. Several investigations have been concentrated on the improvement of wound treatment therapies. Various types of nanomaterials, including metal-based, non-metal-based, and metalloid-based materials, have been explored to treat wounds of various etiologies. Among them, mesoporous silica has received a great deal of attention in order to produce more effective wound dressing materials. Owing to their physicochemical proprieties, mesoporous silicas can act as carriers for the delivery of bioactive molecules. Besides that, in an aqueous environment they can dissolve so releasing orthosilicic acid $Si(OH)_4$, a small molecule, which can promote wound healing. Moreover, mesoporous silicas can also promote blood clotting and achieve hemostasis without causing any side effects. In this context, this PhD thesis aimed at studying the use of mesoporous silica spheres as a material to develop drug delivery systems that combine the beneficial intrinsic effects of the carrier with the therapeutic effects of the supported drug in the prospect of future wound healing applications

The first chapter provides a general overview of the properties of mesoporous silica and its applications in the dermatological field, focusing on the use of mesoporous silica in the treatment of various skin conditions. Particular attention was given to the employment of mesoporous silica in the field of wound healing.

The second chapter gives insights into the use of mesoporous silica-based materials as hemostats, highlighting the most recent research studies concerning their *in vitro* and *in vivo* hemostatic activity as well as their hemolytic ability.

The third chapter deals with the development of an agent that can exploit the hemostatic nature of mesoporous silica. Three different types of mesoporous silica spheres with different properties (i.e. different pore size) were synthesized and their hemostatic performances as well as their hemolytic activity were investigated.

The fourth chapter focuses on the fabrication of a novel material that combines the hemostatic ability of the mesoporous silica spheres with the antifibrinolytic activity of tranexamic acid, to be used for the control of hemorrhages in emergency. Mesoporous silica spheres with large pores were synthesized and, for the first time, loaded with tranexamic acid through an incipient wetness impregnation method.

The fifth chapter provides a brief overview of the role of arginine in wound healing as well as the adsorption of this amino acid on mesoporous silica-based materials.

The sixth chapter presents a research work concerning the development of a system based on spherical mesoporous silica particles for the delivery of arginine for future application in wound healing. The main objective of the study is to investigate how the pH of the impregnating solution may affect the structure of the carrier.

The seventh chapter describes the study of a second type of mesoporous silica particles, which should be less sensitive to the variation of the pH of the impregnating solutions, as a potential carrier for arginine.

Contents

Acronyms ..... **I**

List of figures ..... **V**

List of tables ..... **XI**

1. **Mesoporous silica for therapeutic applications in the skin** **1**

1.1 Introduction 1

1.2 Mesoporous silica: an overview 3

1.2.1 Synthesis of MS: the modified Stöber method 5

1.3 MS and skin disorders 11

1.3.1 Skin structure and skin-particle interaction 12

1.3.2 MS and topical delivery 18

1.3.3 MS and photoprotection 19

1.3.4 MS and skin cancer 21

1.4 MS and wound healing 22

1.4.1 The wound healing process 23

1.4.2 Wound classification 26

1.4.3 MS in wound healing applications 26

1.5 Conclusions 29

1.6 References 30

PART I 39

2. **Mesoporous silica-based materials as hemostatic materials** **41**

2.1 Introduction 41

2.1.1 The hemostatic process 42

2.2 Hemostatic properties of silica-based materials 46

2.3 Hemolytic activity of silica-based materials 54

2.4 Conclusions....60
2.5 References....62
3. **The influence of the physicochemical properties of mesoporous silica particles on hemostasis....65**
3.1 Introduction....65
3.2 Experimental....67
3.2.1 The synthesis of mesoporous silica microspheres (MSM)....67
3.2.2 The synthesis of spherical mesoporous silica particles (SMSP)....68
3.2.3 Instrumental characterization....68
3.2.4 *In vitro* blood coagulation test....69
3.2.5 Hemolysis assay....70
3.3 Results and Discussion....71
3.3.1 Characterization of MSM....71
3.3.2 Characterization of SMSP....77
3.3.3 Clotting blood time test....80
3.3.4 Hemolysis assay....81
3.4 Conclusions....82
3.5 References....84
4. **Mesoporous silica microspheres containing tranexamic acid....87**
4.1 Introduction....87
4.2 Experimental....89
4.2.1 Tranexamic acid loading....89
4.2.2 Characterization....90
4.2.3 Preliminary in vitro release test....91
4.3 Results and Discussion....91
4.3.1 Characterization of TXA@MSM-15°C/min....91
4.3.2 A preliminary in vitro release test....97

4.4 Conclusions....99
4.5 References....101
PART II....105
5. **Adsorption of arginine on mesoporous silicas....107**
5.1 Introduction....107
5.2 Arginine....109
5.3 The adsorption of arginine on mesoporous silica....116
5.4 Conclusions....120
5.5 References....121
6. **Impregnation of spherical mesoporous silica particles with l-arginine: the effect of the pH of the impregnating solutions on the stability of the carrier....125**
6.1 Introduction....125
6.2 Experimental....126
6.2.1 Synthesis of spherical mesoporous silica particles (SMSP)....126
6.2.2 The loading of ARG....126
6.2.3 Instrumental characterization....127
6.2.4 Preliminary desorption test....128
6.3 Results and Discussion....129
6.3.1 Characterization of ARG-11@SMSP....129
6.3.2 Characterization of ARG-x@SMSP....138
6.3.3 Preliminary desorption test....142
6.4 Conclusions....145
6.5 References....146
7. **Impregnation of Mesoporous Silica Microspheres with l-arginine....149**
7.1 Introduction....149
7.2 Experimental....150
7.2.1 MSM synthesis and ARG loading....150

7.2.2 Instrumental characterization.....150
7.2.3 Preliminary desorption test.....151
7.3 Results and Discussion.....151
7.3.1 Characterization of ARG-x@MSM-1°C/min.....151
7.3.2 Preliminary desorption test of ARG.....156
7.4 Conclusions.....159
7.5 References.....161
Conclusions and Outlooks.....163

Acronyms

AAs	Amino Acids
ANOVA	Analysis of Variance
APTT	Activated Partial Thromboplastin Time
ARG	Arginine
ASTM	American Society for Testing and Materials
BET	Barret-Emmett-Teller
BJH	Barlett-Joyner-Halenda
CBT	Clotting Blood Time
CMK	Carbon Mesostructured from Korea
CPC	Cetylpyridinium Chloride
CRASH-2	Clinical Randomization of an Antifibrinolytic in Significant Hemorrhage-2
CSA	Cooperative Self-Assembly
CTAB	Cetyltrimethylammonium Bromide
CTS	Chitosan
DFT	Density Functional Theory
DSC	Differential Scanning Calorimetry
ECM	Extracellular Matrix
ECO	Econazole Nitrate
EGF	Epidermal Growth Factor
FDA	Food And Drug Administration
FDU	Fudan University
FESEM	Field Emission Scanning Electron Microscopy
FGF	Fibroblast Growth Factor (FGF)
FSM	Folded Sheet Mesoporous
FT-IR	Fourier Transform Infrared Spectroscopy
hb	Hemoglobulin
HMWHA	High-Molecular-Weight Hyaluronic Acid
IGF 1	Insulin-Like Growth Factor 1
IND	Indomethacin
IUPAC	International Union of Pure and Applied Chemists
IWI	Incipient Wetness Impregnation
KIT	Korea Advanced Institute of Science and Technology

LMWHA	Low-Molecular-Weight Hyaluronic Acid
M41S	Molecular 41 Sieves
MCF	Mesocellular Foams
MCM	Mobile Crystalline Materials
MS	Mesoporous Silica
MSM	Mesoporous Silica Microspheres
MSNPs / MSNs	Mesoporous Silica Nanoparticles
MSP	Mesoporous Silica Particles
MSS	Mesoporous Silica Sphere
MTX	Methotrexate
NLC	Nanostructured Lipidic Carrier
NOS	Nitric oxide synthase
NPs	Nanoparticles
OMC	Octyl Methoxy Cinnamates
PDGF	Platelet-Derived Growth Factor
PDT	Photodynamic Therapy
PLGA	Poly Lactic-Co-Glycolic Acid
PT	Prothrombin Time
PTFE	Polytetrafluoroethylene
PU	Polyurethane
PVP	Polyvinyl Pyrrolidone
RBCs	Red Blood Cells
RES	Resveratrol
ROS	Reactive Oxygen Species
SBA	Santa Barbara Amorphous
SC	Stratum Corneum
SD	Standard Deviation
SDA	Structure Directing Agent
SEM	Scanning Electron Microscopy
Si	Silica
SMSP	Spherical Mesoporous Silica Particles
SSA	Specific Surface Area
TA	Tannic Acid
TEG	Thrombelastography
TEOS	Tetraethyl Orthosilicate
TF	Tissue Factor
TGA	Thermogravimetry Analysis

TGF	Transforming Growth Factor
TLCT	True Liquid Crystal Template
TMOS	Tetramethyl Orthosilicate
TXA	Tranexamic Acid
UV	Ultraviolet
UV-Vis	Ultraviolet-Visible
VEGF	Vascular-Endothelial Growth Factor
XRD	X-Ray Diffraction

List of figures

Figure 1.1 Classes of particles used in drug delivery [11]. 2

Figure 1.2 Different types of MSPs [19] 4

Figure 1.3 The hydrolysis and condensation reactions of silanes [27]. 6

Figure 1.4 XRD pattern and FESEM images of MCM-41 samples: (a) Sample 1 (template: CTAB) and (b) Sample 2 (template: CPC) [28]. 7

Figure 1.5 Formation of mesoporous structures: (a) via co-operative self-assembly, (b) via true liquid–crystal templating process [29]. 8

Figure 1.6 Schematic representation of various skin disorders and their origin [31] 11

Figure 1.7 Schematic representation of normal skin [41]. 13

Figure 1.8 (a) Topical application for locally acting drugs and (b) Transdermal application for systemically acting drugs [44] 14

Figure 1.9 The pathways of percutaneous absorption [47]. 16

Figure 1.10 The different phases of the wound healing process [83]. 25

Figure 2.1 Overview of the coagulation and clotting factor signaling [9]. 44

Figure 2.2 Current view on the coagulation cascade [11] 45

Figure 2.3 Number of documents related to silica as hemostatic material, in the range 1978 – 2022 [15]. 47

Figure 2.4 Effects of the MCF window size on the time to clot formation [17]. 48

Figure 2.5 (a) CBT time for MSN. (b) FXII surplus in poor platelet plasma after exposed to MSN. (c) Survival rate of animals exposed to a femoral artery injury. Animals were treated with MSN (●) and standard gauze (■) [1]. 49

Figure 2.6 Clotting time versus materials; (a) effect of materials ‘structure on APTT and PT, (b) effect of silica xerogels’ amount on APTT and PT, and (c) effect of Ca content on APTT and PT [20]. 50

Figure 2.7 (a) Water absorbability and (b) Coagulation time of samples [21]. . 52

Figure 2.8 (a) Hemostasis time and (b) Blood loss in the rat amputation model. (c) Antibacterial activity of TA-loaded MS [23]. 53

Figure 2.9 Representation of mesoporous silica nanoparticles hemocompatibility with RBCs [26]. 55

Figure 2.10 Hemolysis assay for amorphous silica (red lines) and Mesoporous silica nanoparticles (green lines), using water as a positive control (blue lines) and PBS as a negative control (dashed black lines). The materials were suspended at 60 (a, c) and 100µg/mL (b, d) [28]. 56

Figure 2.11 (a) Percentage of hemolysis of RBCs and photographs of hemolysis of RBCs incubated with four sizes of nonporous silica nanoparticles (SS), and (b) Percentage of hemolysis of RBCs and photographs of hemolysis of RBCs incubated with four sizes of mesoporous silica nanoparticles (MS) [29]. 57

Figure 2.12 Hemolysis assay for MCM-41 (green lines) and SBA-15 (red lines), using water as a positive control (blue lines) and PBS as a negative control (dashed black lines). The materials were suspended at 50 (a,c) and 100 µg /ml (b,d) [30]. 58

Figure 2.13 Hemolysis assay on bare SiO_2. (A) Relative rate of hemolysis in human RBCs upon incubation with nanoparticle suspension at incremental concentrations. Photographs of hemolysis of RBCs incubated with (B) Stöber suspension, (C) Meso S suspension, (D) AR2 suspension, (E) AR4 suspension, and (F) AR8 suspension. The tubes are lined up (from left to right) as negative control (PBS), positive control (water), 10 µg/mL suspension, 50 µg/mL suspension, 100 µg/mL suspension, 250 µg/mL suspension, and 500 µg/mL suspension [31]. 59

Figure 2.14 Hemolysis assay on amine modified SiO_2. (A) Relative rate of hemolysis in human RBCs upon incubation with amine-modified nanoparticle suspension at incremental concentrations. Photographs of hemolysis of RBCs incubated with (B) SA suspension, (C) MA suspension, (D) 2A suspension, (E) 4A suspension, and (F) 8A suspension. The tubes are lined up (from left to right) as negative control (PBS), positive control (water), 10 µg/mL suspension, 50 µg/mL suspension, 100 µg/mL suspension, 250 µg/mL suspension, and 500 µg/mL suspension [31] 60

Figure 3.1 Schematic representation of the hemolysis assay [12]. 70

Figure 3.2 (a) Negative control (0 % lysis) and (b) Positive control (100 % lysis). 71

Figure 3.3 The nitrogen adsorption- desorption isotherm of MSM-1°C/min (orange curve) and MSM-15°C/min (black curve). 72

Figure 3.4 The DFT pore size distribution of MSM-1°C/min (orange curve) and MSM-15°C/min (black curve). 73

Figure 3.5 The FESEM images of (a) MSM-1°C/min and (b) MSM-15°C/min (magnification: 1.00 K X, 20.00 K X). 74

Figure 3.6 The FT-IR spectra of MSM-1°C/min and MSM-15°C/min 75

Figure 3.7 The XRD pattern of MSM-1°C/min and MSM-15°C/min at low (inset) and wide angles. 76

Figure 3.8 The nitrogen adsorption- desorption isotherm with BJH pore size distribution (inset) of SMSP. 77

Figure 3.9 (a) The FESEM images (magnification: 25.00 K X, 250.00 K X) and (b) particles size distribution of SMSP. 78

Figure 3.10 The FT-IR spectrum of SMSP 79

Figure 3.11 The XRD pattern of SMSP at low (a) and wide angles (b). 80

Figure 3.12 The CBT for MSM-1°C/min, MSM-15°C/min, SMSP and control. Data are represented as mean ± SD (n=3). * Significant difference ($p < 0.05$) analysed by one-way ANOVA. 81

Figure 3.13 The hemolysis ratio for MSM-1°C/min, MSM-15°C/min and SMSP at two different concentrations (100 and 500 µg). 82

Figure 4.1 The chemical structure of tranexamic acid (TXA) [2]. 88

Figure 4.2 TGA curves of MSM-15°C/min and TXA@MSM-15°C/min. 92

Figure 4.3 (a) Nitrogen adsorption-desorption isotherms and (b) PSD of MSM-15°C/min and TXA@MSM-15°C/min. 94

Figure 4.4 XRD patterns of MSM-15°C/min, TXA@MSM-15°C/min and pure TXA. 95

Figure 4.5 FT-IR spectra of MSM-15°C/min, TXA@MSM-15°C/min, and pure TXA. 96

Figure 4.6 CBT for MSM-15°C/min, TXA@MSM-15°C/min and control. Data are represented as mean ± SD (n=3). * Significant difference ($p < 0.05$) analysed by one-way ANOVA. 97

Figure 4.7 FT-IR Spectra of TXA@MSM-15°C/min before and after release test. 98

Figure 4.8 Release profile of TXA@MSM-15°C/min. Data are represented as mean ± SD (n=3).....99

Figure 5.1 The chemical structure of L-arginine (ARG) [16].....110

Figure 5.2 Arginine metabolism in wounds [15]. 111

Figure 5.3 Macroscopic appearance of the surgical wound surface after 2 weeks [28].....114

Figure 5.4 The release profile of arginine from Arg-Lig-NF (F5) gel in phosphate buffer pH 7.4 (a) and (b) Photographs of macroscopic appearance of wounds treated with Arg-Lig-NF gel (F6), Lig-NF gel (F5), arginine solution, and normal saline; on the surgery day (0), 4 and 9 days [29].....115

Figure 5.5 ARG in vitro release profile from ARG-loaded CHITARG [30]....116

Figure 5.6 (a) Distribution of different protonated forms of ARG, and (b) adsorption of ARG on the surface of highly dispersed silica from (*1*) water, (*2*) 0.01 and (*3*) 0.1 M NaCl solutions [31].....117

Figure 5.7 (a) Adsorption amounts of ARG on SBA-15 at different pH, and (b) ARG adsorption on SBA-15 at pH 10 with different added NaCl concentrations [11]. 118

Figure 5.8 The release profile of ARG/MCM-48 at pH 1.2 and 7.4 [32]. 119

Figure 5.9 The release profile of ARG/TPA-MCM-41 (a) at pH 7.4 and (b) pH 2 [32].....119

Figure 6.1 The TGA curves of SMSP (black curve) and ARG-11@SMSP (purple curve).....130

Figure 6.2 (a) The nitrogen adsorption-desorption isotherms and (b) The PSD of SMSP (black curve) and ARG-11@SMSP (purple curve). 131

Figure 6.3 Schematic representation of the dissolution process of MSP in aqueous solution [19].....132

Figure 6.4 The nitrogen adsorption-desorption isotherms of SMSP (black curve), SMAP-H_2O (sky-blue curve) and SMSP-NH_4OH (brown curve).....134

Figure 6.5 The FESEM images of SMSP and ARG-11@SMSP (magnification 250.00 K X). 135

Figure 6.6 The XRD patterns of SMSP (black), ARG-11@SMSP (purple) and pure ARG (blue). 136

Figure 6.7 The FT-IR spectra of SMSP (in black), ARG-11@SMSP (in purple) and pure ARG (blue).....137

Figure 6.8 Ionization States of ARG in aqueous solution (adapted from [7])..137

Figure 6.9 (a) The nitrogen adsorption-desorption isotherms and (b) PSD of SMSP (black curve), ARG-5@SMSP (green curve), ARG-9@SMSP (red curve), ARG-10@SMSP (yellow curve) and ARG-11@SMSP (purple curve). 139

Figure 6.10 The FESEM image of SMSP and ARG-5@SMSP (magnification 250.00 K X). 140

Figure 6.11 The XRD patterns of SMSP (black), ARG-5@SMSP (green), ARG-9@SMSP (red) and ARG-10@SMSP (yellow). 141

Figure 6.12 The FT-IR spectra of SMSP (in black), ARG-5@SMSP (in green), ARG-9@SMSP (in red) and ARG-10@SMSP (in yellow). 142

Figure 6.13 The FT-IR Spectra of (a) ARG-5@SMSP and (b) ARG-11@SMSP at different desorption times. 143

Figure 7.1 (a) The nitrogen adsorption-desorption isotherms and (b) PSD of MSM-1°C/min, ARG-5@MSM-1°C/min and ARG-11@MSM-1°C/min. 152

Figure 7.2 The FESEM images of (a) MSM-1°C/min, (b) ARG-5@ MSM-1°C/min and (c) ARG-11@ MSM-1°C/min (magnification 20.00 K X). 154

Figure 7.3 The XRD patterns of MSM-1°C/min, ARG-5@MSM-1°C/min, ARG-11@MSM-1°C/min and pure ARG. 155

Figure 7.4 FTIR spectra of MSM-1°C/min, ARG-5@MSM-1°C/min, ARG-11@ MSM-1°C/min and pure ARG. 156

Figure 7.5 FT-IR Spectra of (a) ARG-5@MSM-1°C/min and (b) ARG-11@MSM-1°C/min at different desorption times. 157

List of tables

Table 1.1 Examples of types of interaction between template head group and inorganic precursor [29].....10

Table 2.1 List of the coagulation factors (adapted from [9]).....43

Table 3.1 SSA_{BET} and Pore volume of MSM-1°C/min and MSM-15°C/min. 72

Table 5.2 Summary of studies showing the effect of arginine supplementation on wound-healing [15].....112

Table 6.1 SSA_{BET} and Pore volume of SMSP and ARG-11@SMSP 133

Table 6.2 Results of the desorption test of ARG-5@SMSP and ARG-11@SMSP.....144

Table 7.1 SSA_{BET} and Pore volume of MSM-1°C/min, ARG-5@ MSM-1°C/min and ARG-11@ MSM-1°C/min. 153

Table 7.2 Results of the desorption test of ARG-5@MSM-1°C/min and ARG-11@MSM-1°C/min. 158

Chapter 1
Mesoporous silica for therapeutic applications in the skin

1.1 Introduction

Nanoporous materials could be defined as regular organic or inorganic frameworks which contain pores at the nanoscale, in the range of 1 - 100 nm. Some examples of nanoporous materials are zeolites, metal-organic frameworks, metal oxides, wood, and rubber [1]. Compared to bulk materials, nanoporous materials possess unique features such as, high surface to volume ratio, high active surface area, large porosity, low densities, and improved chemical and physical properties [2,3]. Based on their pore size, porous materials are classified by the International Union of Pure and Applied Chemists (IUPAC) into three groups: microporous (pore size < 2nm), mesoporous (pore size 2-50 nm) and macroporous materials (pore size > 50 nm). Mesoporous materials may be more interesting than the others due to their high specific surface area, intermediate pore dimension, narrow pore size distribution, good selectivity, easy access to pores, high adsorption capacity, and simple surface functionalization [4]. Because of the above-mentioned properties, mesoporous materials have found different uses in several fields like adsorption, catalysis, sensors, chemical separation, and biomedical applications [1,2]. As far as the biomedical area is concerned, both organic and inorganic mesostructured materials have been studied in several applications, in particular as drug delivery systems [5].

According to the American national institute of health, “drug delivery systems are defined as the formulation of a device that enables the introduction of therapeutic substances into the body and improves efficiency and safety by

controlling the rate, time and place of release of drug in the body" [6]. Conventional drug delivery involves the formulation of the drug into a suitable form, such as a compressed tablet for oral administration or a solution for intravenous administration. However, these forms present various limitations such as poor bioavailability, side effects, low drug loading capacity, plasma fluctuation of the drug levels, low therapeutic effectiveness, and lack of target delivery. Therefore, in the last years many researchers are trying to develop new drug delivery systems to overcome the inconveniences of the conventional ones. Among the different approaches, it has been found that the use of nanoporous systems drug carriers appears to be quite promising. Owing to their chemical and physical properties, these systems can incorporate different biomolecules and drugs as well as enhance their solubility which consequently results in higher dissolution rate and in an enhancement of their bioavailability [6–8]. Moreover, the possibility of functionalizing the surface by conjugating target molecules allows the loaded drug to be directed to the site of interest, thereby improving effectiveness and reducing side effects [9,10]. Different materials have been proposed as drug carriers, which include both organic and inorganic supports. Some of the most common studied systems are reported in figure 1.1.

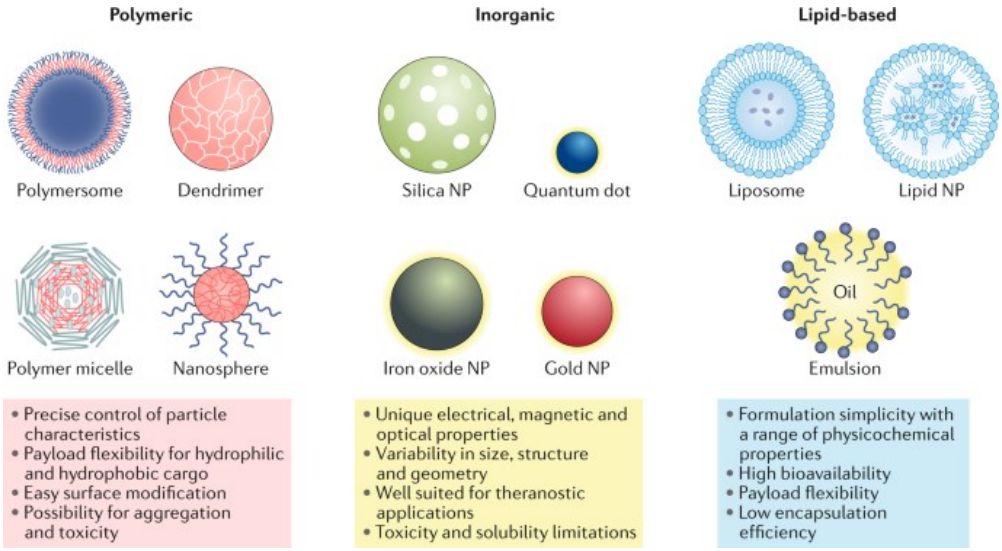

Figure 1.1 Classes of particles used in drug delivery [11].

Among mesoporous materials, mesoporous silica-base materials have been considered one of the most interesting materials for the development of drug carriers after their first report in 2001 by Vallet-Regì [12]. Since that moment, various

studies have been performed on MCM-41 silica material and its variety of modifications. Other mesoporous silicas have also been investigated as carriers for a variety of drugs, including nonsteroidal anti-inflammatories, antibiotics and chemotherapeutics [13–15]. Compared to other unconventional drug delivery systems (liposomes, polymeric micelles, and lipid-based nanoparticles), mesoporous silica (MS) offers unique properties such as:

- thermal, mechanical, and chemical stability;
- large pore volume and surface area, usually above 1 cm^3 and 700 m^2/g, respectively (these properties provide high potential for drug adsorption and loading within the pore channels);
- ordered mesoporous structure and narrow distribution of tunable pore size (2-30 nm), which allow better control of drug loading and release kinetics;
- tunable particle size, which is suitable for easy endocytosis by living cells;
- in principal two surfaces (inner pore surface and external particle surface) easily modifiable for both controlled and targeted drug delivery;
- good biocompatibility (Silica materials are "Generally Recognized as Safe" by the United States Food and Drug Administration (FDA). *In vivo* biosafety evaluation of cytotoxicity, biodegradation, biodistribution and excretion, showed low toxicity of these materials);
- integration with magnetic and/or luminescent substances, which enables bioimaging and drug delivery [16,17].

These unique features make MS a good candidate for developing drug delivery systems. In the next section, an overview of the common methods used for the synthesis of MS is reported. Besides that, the use of MS in the dermatological field (i.e., in topical drug delivery and wound healing) is reported as it represents the main topic of this PhD project.

1.2 Mesoporous silica: an overview

The first attempt of synthesis of MS goes back to the early 1970's. A patent dated back to 1971 reports the synthesis of low bulk density silica in the presence of a

cationic surfactant [18]. However, the importance of this material was not recognized due to the lack of information concerning its properties.

In 1992, the synthesis of a new family of ordered mesoporous silicas named as Molecular 41 Sieves (M41S), was reported by the scientists of the Mobile Research and Development Corporation. These materials exhibited amorphous walls, high surface area, large pore volume and tunable pore sizes. In the M41S family, three different meso-structures were distinguished: MCM-41 with hexagonal pore arrangement, MCM-48 with cubic structure, and MCM-50 with a lamellar geometry. Among these materials, the MCM-41 family is the most widely explored because it is more stable and easier to obtain than the other ones. This material possesses a highly ordered hexagonal array of pores with a very narrow pore size distribution, ranging from 2.5 to 6 nm.

After the discovery of the M41S family, significant efforts have been made to obtain MS with different pore size and morphology. Other types of MS materials were developed (figure 1.2), which include the Folded Sheet Mesoporous materials-16 (FSM-16), the Fudan University (FDU) material, the Korea Advanced institute of science and Technology (KIT) material, and the Santa Barbara Amorphous silica family (SBA-n).

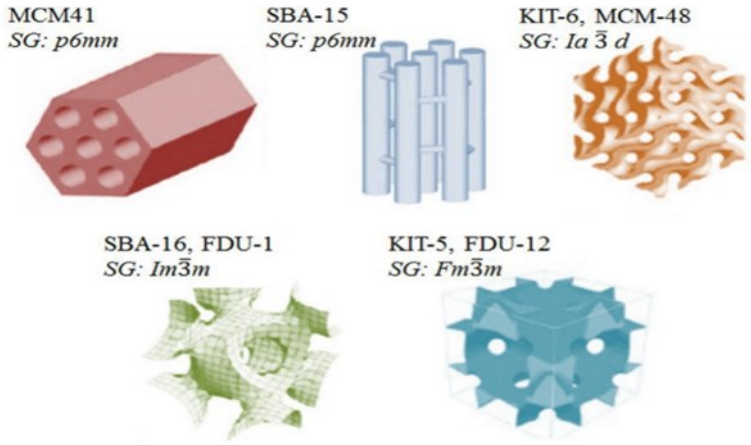

Figure 1.2 Different types of MSPs [19]

In 1998 an important material with a hexagonal structure was synthesized by the researchers of Santa Barbara university, and it was called SBA-15 (Santa Barbara Amorphous no 15). Compared to MCM-41, SBA-15 is characterized by larger pore size ranging from 4 nm to 30 nm, thicker walls, and better thermal,

mechanical, and chemical resistance. Owing to its features, SBA-15 is considered the best choice for different uses in different application fields [1,8,20].

1.2.1 Synthesis of MS: the modified Stöber method

There is a wide number of synthetic approaches for the synthesis of MS-based materials, which include the sol-gel process and hydrothermal synthesis. Most of them involve the use of three main elements, a surfactant as a structure directing agent (SDA), a silica precursor, and a catalyst. Other additive components, such as solvents and swelling agents can be used to regulate the properties of the synthesized material. Furthermore, by varying the synthesis conditions (i.e., temperature, choice of the silica precursor, concentration of reagents, pH, duration), materials with different morphologies, sizes and porous structures can be obtained [21].

Nowadays, majority of MS-based materials are synthesized by the modified Stöber method, which consists in the combination of two methods, i.e. the sol-gel and the soft templating methods. The process can be summarized in the following steps: 1) the hydrolysis and condensation of the silicon alkoxide in the presence of ordered assemblies of surfactant micelle templates; 2) the removal of the structure directing agent by calcination or solvent extraction to generate the mesoporous structure [22–24].

The *sol-gel* method is a wet chemical process also known as the chemical solution deposition method; it is widely explored in the field of material science for the synthesis of various inorganic materials like ceramics, glasses, and silica. It consists in the formation of a gel, a continuous inorganic network including a continuous liquid phase, starting from a sol, a colloidal of small particles dispersed into a liquid, by a bottom-up approach [8,20]. In 1968, *Stöber et al*. developed a set of chemical reactions based on sol-gel chemistry for the synthesis of monodispersed, micron size silica spheres [25]. The formation of silica particles through sol-gel chemistry occurs through a series of chemical reaction: the hydrolysis and condensation of a silicon alkoxide (figure 1.3) [26]. The most widely used silicon alkoxides are tetraethyl orthosilicate (TEOS) and tetramethyl orthosilicate (TMOS). Hydrolysis is the first reaction, which occurs once the silica precursor is contacted with a mixture of water and alcohol. The reaction between water and the silica precursor leads to the generation of a silanol group (Si-OH). In the second step, the silanol group reacts with either another silanol or an alkoxide group

through a condensation mechanism, so forming a strong covalent siloxane bridge (Si-O-Si) and progressively producing the entire silica structure [23].

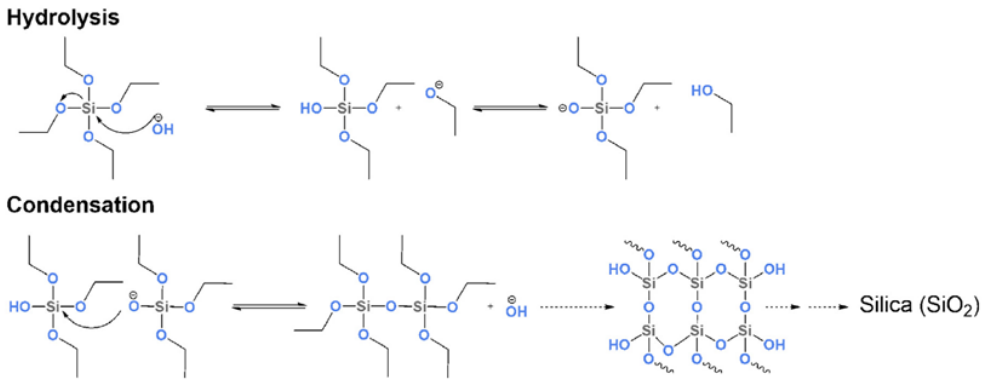

Figure 1.3 The hydrolysis and condensation reactions of silanes [27].

Typically, a sol-gel process takes place in the presence of an acid or base catalyst. Depending on the pH of the system, the rate of both the hydrolysis and condensation reactions can be affected and consequently the properties of the obtained material can be influenced. Generally, under acidic condition, hydrolysis is much faster than condensation, so resulting in the formation of many small particles that tend to form a gel-like structure. On the other hand, under basic condition, condensation proceeds faster than hydrolysis, which results in the formation of large silica particles [27].

To obtain spherical MS particles, the Stöber method was modified by the incorporation of organic surfactants, which act as a structure-directing agent for pores formation. In 1997, *Grun et al.* [28] first modified the Stöber method by introducing the use of cationic surfactants (Cetyltrimethylammonium Bromide CTAB and Cetylpyridinium chloride CPC) as templates to produce spherical shape silica particles with MCM-41 properties. Based on their results, the synthesized particles showed a spherical morphology and an ordered hexagonal pore structure as revealed by the scanning electron microscopy (SEM) images and the X-ray diffraction pattern, respectively (figure 1.4).

(a)

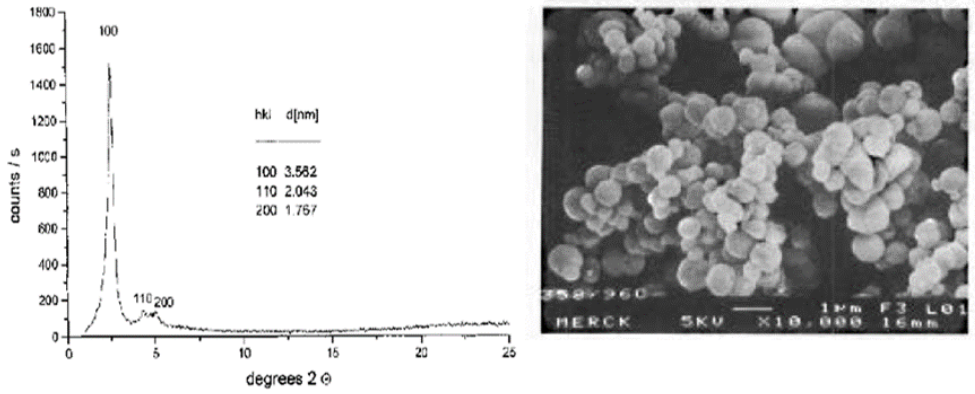

(b)

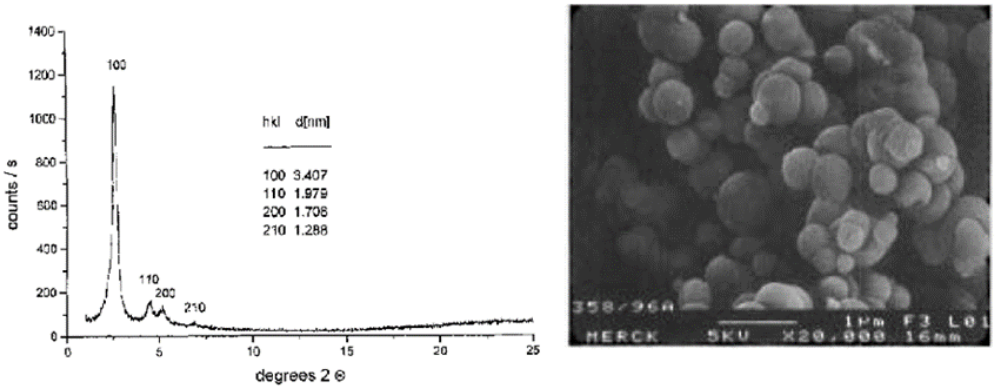

Figure 1.4 XRD pattern and FESEM images of MCM-41 samples: (a) Sample 1 (template: CTAB) and (b) Sample 2 (template: CPC) [28].

Two main mechanisms were proposed to describe the formation of mesoporous silica particles: the cooperative self-assembly (CSA) mechanism and the true liquid crystal template (TLCT) one (figure 1.5). In the CSA mechanism (figure 1.5a), the self-assembled SDA aggregates simultaneously with the already added silica precursor and a liquid-crystal phase containing both the organic micelle and the inorganic precursor is formed. In contrast, in the TLCT mechanism (figure 1.5b), the concentration of the surfactant is above the critical micellar concentration so that, under the prevailing conditions (temperature and pH) and without the presence of the inorganic precursor, the surfactant molecules arrange themselves and create a lyotropic liquid-crystalline phase. Then, silica precursor is added, and silicate

specie condense through electrostatic and hydrogen bonding interactions on the preformed liquid-crystalline phase, leading to the formation of mesostructured silica-micelle [29].

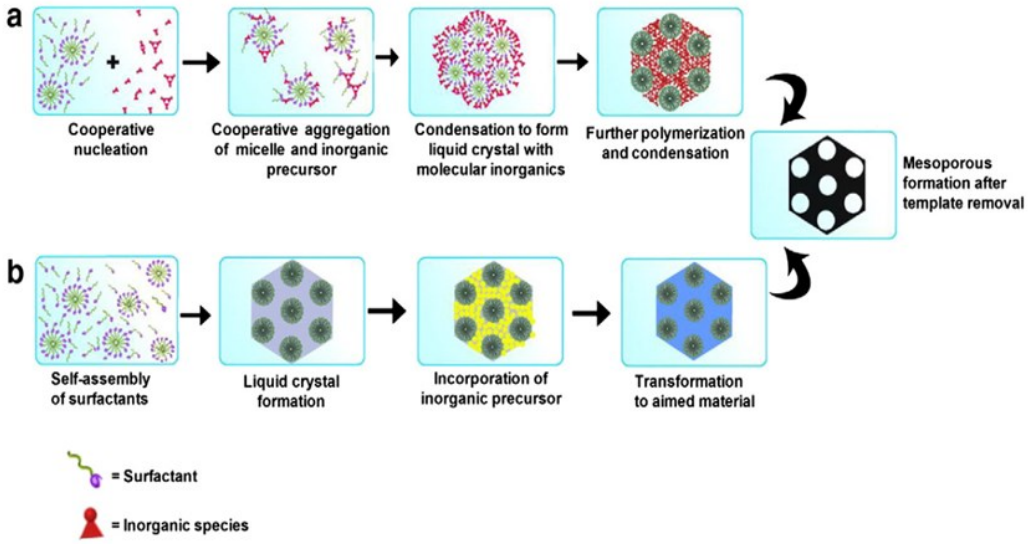

Figure 1.5 Formation of mesoporous structures: (a) via co-operative self-assembly, (b) via true liquid–crystal templating process [29].

As mentioned earlier, surfactants play an important role in the synthesis of mesoporous materials. Depending on their dissociation in the aqueous environment, these surfactants can be classified into three types:

1) Cationic surfactants that are dissociated in water into an amphiphilic cation and an anion, usually of halogen type.

2) Anionic surfactants that are dissociated in water in an amphiphilic anion, and a cation, which is generally an alkaline metal (Na^+, K^+), or a quaternary ammonium.

3) Non-ionic surfactants that do not ionize in aqueous solutions, because their hydrophilic group is non-dissociable, such as an alcohol or phenol.

Based on the surfactant type and the interaction between the inorganic phase and surfactant, different synthesis pathways have been identified for the preparation of mesoporous materials under a wide range of pHs, temperatures, and surfactant nature and concentration. There are six possible types of interaction, which depends

on the charge of the surfactant molecule, on the charge of the organic species, and on the presence of mediating ions. These pathways are S^+I^-, S^-I^+, $S^-M^+I^-$, $S^+X^-I^+$, S^0I^0 and N^0I^0, where S is the surfactant, I is the inorganic precursor, X is the mediating anionic species, M is the intermediate cation, S^0 is the neutral amine, I^0 is the hydrated inorganic oligomer and N^0 is non-ionic template [20,30]. For those pathways involving strong electrostatic interactions (i.e., S^+I^-, S^-I^+, $S^-M^+I^-$, $S^+X^-I^+$), the charge of the inorganic precursor is determined by the pH and isoelectric point. As far as silica species are concerned, they usually present a positive charge at pH<2, neutral charge at pH=2 and a negative charge at pH>2. Synthesizes routes which employ the use of a cationic surfactants are usually performed in an alkaline environment so that the anionic inorganic species stabilize with the cationic surfactant through S^+I^- strong interaction. On the other hand, those synthesis procedures involving the use of non-ionic surfactants are generally performed in a neutral or acidic environment. In this case, the inorganic species interact with the surfactant through H-bonding between the hydroxyl group of hydrolyzed silicate species and the polar surfactant head-groups [29].

Depending on the surfactant used for the synthesis and the interaction established between the inorganic species and the organic template molecules, different mesoporous materials can be obtained as examples reported in table 1.1.

Table 1.1 Examples of types of interaction between template head group and inorganic precursor [29].

Surfactant Type	Interaction Type	Interaction pathway	Examples
Cationic S^+ (CTAB, CPC)	Electrostatic interactions	S^+I^-	Tungsten oxide, MCM-41
		$S^+X^-I^+$	Lamellar zinc phosphate, cubic Pm3n silica
Anionic S^- (Alkylbenzene sulfonates)	Electrostatic interactions	S^-I^+	Lamellar Iron oxide
		$S^-M^+I^-$	Lamellar aluminum oxide, zinc oxide
Neutral S^0/N^0 (Pluronic p123, F127)	H-bonding interactions	S^0I^0	Hexagonal silica HMS
		N^0I^0	Silica MSU-X

The *hydrothermal synthesis* process is another approach used to synthesize MS particles. This method is similar to the sol-gel process, but the chemical reactions are carried out in a sealed container at elevated temperatures and high pressure. The advantages of this method include the enhancement of the hydrothermal stability and extended pore dimension of the synthesized material. However, the use of this technique is limited since it requires the use of specific equipment, high temperatures and longer reaction time, resulting in a high-cost procedure [21].

1.3 MS and skin disorders

Skin is the largest organ of the human body, and it represents the outmost barrier between the body and the surrounding environment. One of the main roles of the skin is to prevent invasion of pathogens by creating a physical barrier between the inside and the outside of the body [31]. Owing to its continuous exposure to the external environment, skin can undergo different damages. Aging, continuous exposure to oxidants, infectious pathogens, ultraviolet (UV) radiation and other environmental and genetic factors as well as trauma can lead to the development of a diverse set of skin disorders (figure 1.6) [32]. Skin diseases are considered to be one of the leading causes of global disease burden since they affect millions of people worldwide [33]. Despite the great efforts to improve dermatological treatments efficacy, many skin-related problems are still difficult to treat. Various molecules have been proposed for the treatment of skin-related problems; however, instability, high lipophilicity, poor aqueous solubility and low permeability have limited their application [32].

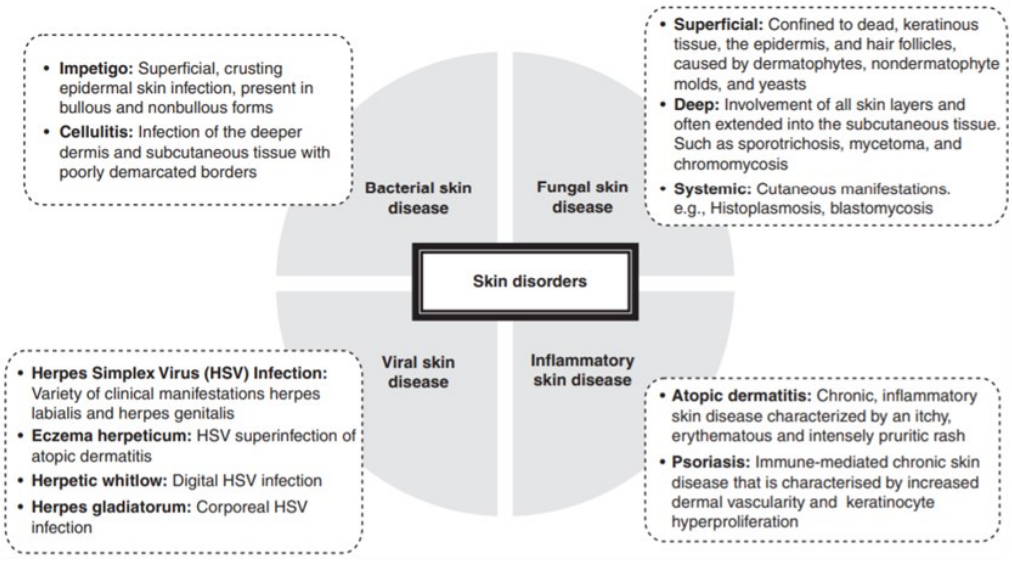

Figure 1.6 Schematic representation of various skin disorders and their origin [31].

To overcome these limitations, the use of carries able to control the release of therapeutic agents has been proposed. Owing to its unique features, many researchers have studied the administration of silica to the skin and have

demonstrated that the use of MS particles as drug carriers for the treatment of skin disorders showed beneficial effects in improving different therapies [34].

1.3.1 Skin structure and skin-particle interaction

Human skin is a complex tissue and, generally, it differs in structure and thickness from one person to another. Commonly, skin consists of two main layers: the epidermis and the dermis (figure 1.7) [35]. Each of these layers consists of different combinations of cells with various functions in the body [36].

The epidermis is the most external layer of the skin, and its thickness may vary from 0.5 mm (eyelid) to 1.5 mm (hand palms and foot soles). It is an avascular tissue composed mainly of two types of cells: keratinocytes, which accounts approximately for 90% and play an essential role in the synthesis of keratin and skin repair, and non-keratinocytes (i.e., melanocytes, Langerhans cells and Merkel cells), which are involved in ultraviolet protection and immunological functions [36,37]. The epidermis is a stratified squamous epithelium which is usually divided into four or five layers (or strata), depending on its position in the body. Starting from the deepest to the most superficial one, these layers are: the stratum basalis, stratum spinosum, stratum granulosum, stratum lucidum (present only in the thick skin of soles and palms) and stratum corneum (SC) [38]. The SC is the outermost layer of the epidermis; it is composed of corneocytes, i.e. terminally differentiated keratinocytes, surrounded by an extracellular lipid matrix in a brick-and-mortar arrangement. Owing to its composition and structure, the stratum corneum represents the main physical barrier of the skin. In fact, it modulates the absorption and permeation of drugs and particles across the skin. [39,40].

The dermis lies below the epidermis. It is a 0.3-5 mm thick layer of connective tissue, made of collagen and elastin, that provides strength and flexibility to the skin. Moreover, the dermis also includes nerve endings, hair follicles, sebaceous and sweat glands, and blood vessels, which supply nutrients to the epidermis [35,38].

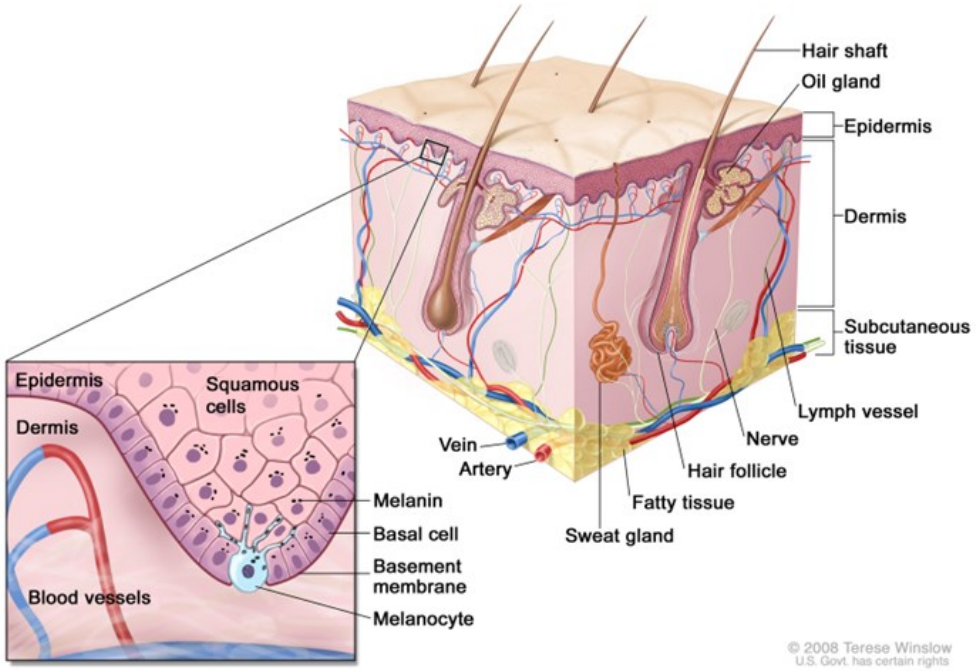

Figure 1.7 Schematic representation of normal skin [41].

The high surface area of the skin makes it a promising route of delivery for both local and systemic drugs. *Topical drug delivery* refers to a method where the drug containing formulation is applied directly to the skin for the treatment of local diseases. Examples of topical products include cutaneous antifungal treatments, local anesthetics, and analgesics [40]. Compared to other routes of administration, topical delivery presents several advantages, such as the improvement in the physiological and pharmacological response and patient compliance, a highly selective delivery of the drug to the site of action with consequent reduction of its systemic toxicity and a non-invasive technique and ease of application [42]. On the other hand, transdermal drug delivery refers to a method where a formulation applied onto intact skin delivers the drug in the systemic circulation. In this case, the drug penetrates through the SC, reaches the dermal layer, and then gets adsorbed via the dermal microcirculation so conveying in the blood (figure 1.8). The main advantage of this route lies in the avoidance of the hepatic first-pass metabolism, which improves drug bioavailability [43]. Examples of transdermal devices are the patches used to deliver opioid analgesics for the treatment of chronic pain [44].

(a)

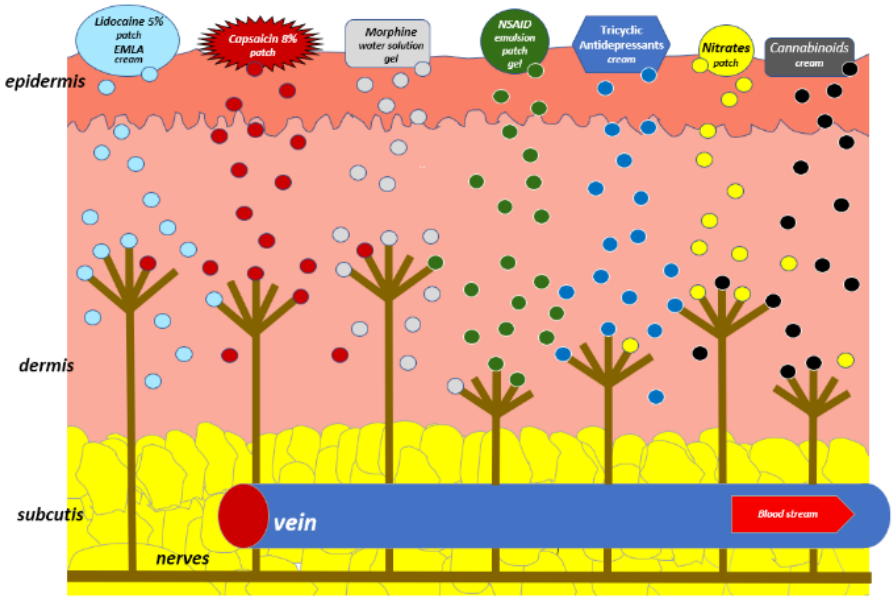

(b)

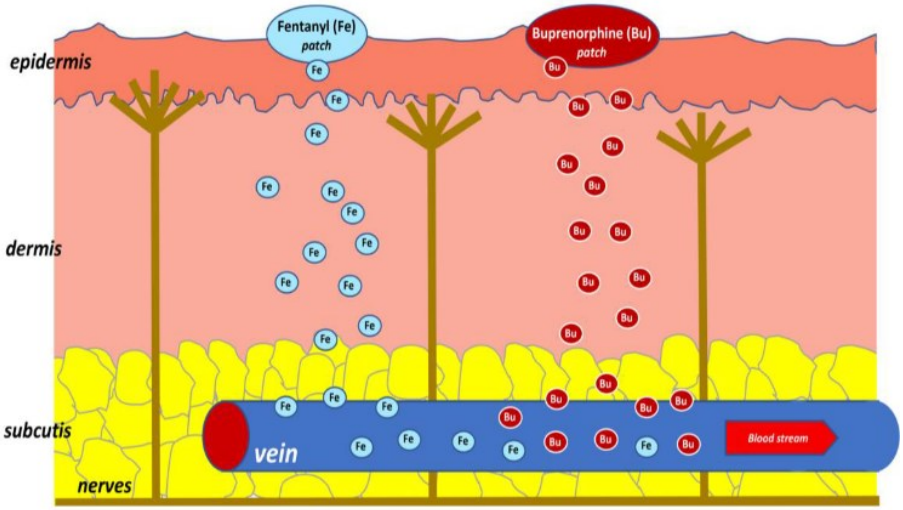

Figure 1.8 (a) Topical application for locally acting drugs and (b) Transdermal application for systemically acting drugs [44].

Due to the unique structure of the skin, the molecules that can penetrate successfully the SC are limited to small (both lipophilic and hydrophilic) ones. This excludes many potentially therapeutic compounds. Therefore, great efforts have been done to develop new strategies to enhance the penetration of large molecules through the skin (in topical delivery) or to improve molecules permeation into skin layers (in transdermal delivery). These strategies include both chemical enhancers and physical enhancers. Chemical enhancers like fatty acid, alcohol, and amides, can be used to improve drug penetration by perturbating the highly ordered structure of the SC or by solubilizing and extracting the keratin and/or lipid components of SC. However, the use of chemical enhancers has been limited as they tend to be skin irritants, because of their disruptive effect on the lipid structure of the skin. Physical enhancers, instead, involve the use of physical methods such as sonophoresis, laser and or thermal ablation, electroporation, radiofrequency treatment and iontophoresis, to temporary compromise the integrity of the skin and improve drug permeation. However, also these methods are invasive and they could cause long-term damage to the skin barriers [45]. Therefore, to overcome all the above-cited limitations, researchers proposed the use of nano and micro-particles as drug delivery systems for both topical and transdermal applications.

When micro- and nano-particles are applied to the skin, they can remain on the surface or penetrate it through three pathways (figure 1.9):

1) the intracellular pathway, which involves a direct path through the cell membranes of multiple layers of epidermis;

2) the intercellular pathway, which involves a more tortuous path between the epidermal cells;

3) the trans-appendageal route, which involves particles accumulation in hair follicles, sweat glands, or skin furrows for either penetration to the deeper skin layers or retention for increased drug release (figure 1.9) [46].

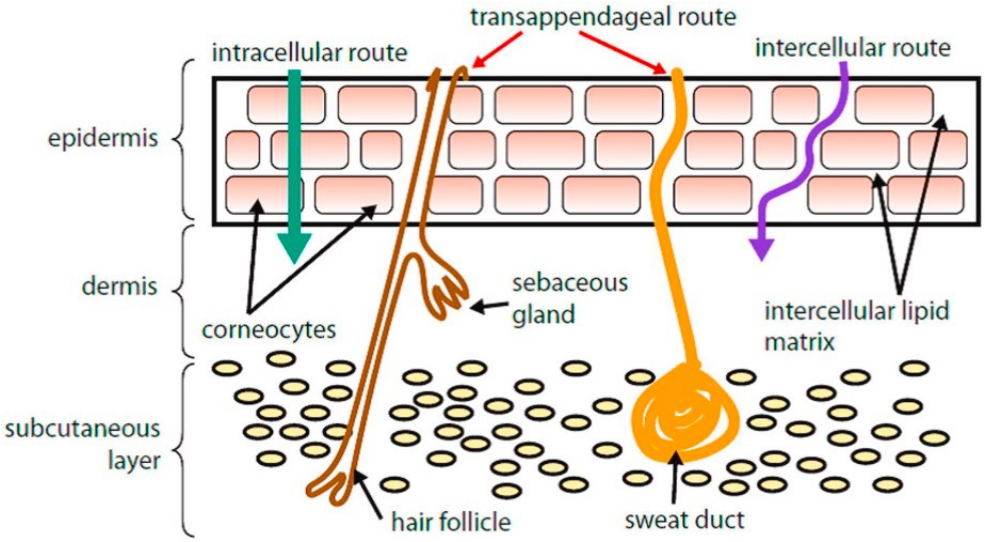

Figure 1.9 The pathways of percutaneous absorption [47].

Physicochemical properties of particles such as size, shape, and surface charge, are considered the most important factors affecting particles penetration/permeation through the SC, as well as their accumulation in furrows or appendages. Therefore, understanding the behavior of particles with different sizes, shapes, and surface chemistry in contact with the skin surface and their interaction is very important to design appropriate drug delivery systems for both topical and transdermal applications. Generally, particle size is considered the most important factor affecting particle penetration/permeation. It is known that only those particles whose size is below 1 nm are able to permeate the intact skin, while particles with an average size lower than 25 nm can penetrate but not permeate the skin, and those with higher diameters are not able to cross the normal or perturbed skin [48]. Several studies investigate the effect of particle size of silica on skin penetration. For example, *Valetti et al.*[49] studied the distribution of MS particles with different sizes (average size of 400–600 nm, 2, and 7 µm, respectively) topically applied to human and animal skin. The results of the study showed that the smallest particles i.e., those with an average size of 400- 600 nm, were able to reach furthest down in the furrows to a depth of about 25 µm, while the micron sized particles were found to remain on the surface. A similar result was found by *Rancan et al.* [50] who studied the skin penetration and cellular uptake of amorphous silica particles with positive and negative surface charge and different sizes (from 42 ± 3 to 291 ± 9). In their work, the authors observed that silica particles above 75 nm in size did not penetrate human skin and they concluded that skin penetration of silica was size-dependent

rather than surface-charge-dependent. Similarly, *Jung et al*. [51] observed that silica particles with size of 33 and 78 nm were not able to reach the epidermis, but they were retained in the SC. In a similar work, *Boonen et al.* [52] investigated the penetration of silica particles with a size of 3 μm both in water and in a 65% ethanolic plant extract on ex vivo human skin by scanning electron microscopy (SEM). Contrary to previous reported studies, the authors observed that 3 μm silica particles can penetrate the living epidermis. Moreover, when formulated in the ethanolic-based plant medium, silica particles were able to reach the dermis.

As stated earlier, hair follicles represent an interesting entry route into the skin for those topically applied substances that are not able to penetrate the skin via intercellular o intracellular pathway (for example large particles). *Patzelt et al.* [53] investigated the influence of the particle size of two different types of particles (PLGA- and silica particles) on the follicular penetration depth through *in vitro* tests on porcine skin. In the study, porcine skin was chosen as a model as the size of hair follicles corresponds to the size of human terminal hair follicles. The results indicated that particles with an average size of 643 and 646 nm, respectively, had optimal penetration depth in porcine hair follicles compared with those with smaller or larger size. In addition, it was observed that by varying the particle size, different sites within the porcine hair follicle can be selectively targeted. This result is very interesting since selective follicular targeting offers opportunities in the treatment of hair follicle-associated diseases, such as immunotherapy and even gene therapy [54]. Besides providing an efficient penetration pathway for topically applied substances, hair follicles can act as reservoirs for drug delivery. *Lademann et al.* [55] demonstrated that the storage reservoir capacity of hair follicles was 10 times longer than that of SC. This behavior was ascribed to the fact that in the SC topically applied particles are stored mainly within the upper cell layers in the intercellular spaces, and this reservoir is generally depleted quickly by textile contact, washing, and normal desquamation. On the other hand, the reservoir of the hair follicles is a long-term reservoir, because depletion can only occur by slow processes such as the flowing out with the sebum production.

1.3.2 MS and topical delivery

The use of MS has been explored for topical administration of several molecules. *Nafisi et al.* [56] reported the incorporation of lidocaine into MCM-41 and amine modified MCM-41. Lidocaine is a member of the Caine family that is used as a topical anesthetic but shows poor aqueous solubility and negligible skin uptake. The achieved materials were investigated for both *in vitro* drug release and *ex vivo* permeation studies. *In vitro* release test showed that the release of lidocaine from MCM-41 and MCM41-NH_2 was faster than pure lidocaine due to the mesopores of MCM-41, which change the crystalline state of lidocaine to a non-crystalline state. Comparing the dissolution profiles of lidocaine from MCM-41 and MCM41-NH_2, it was found that dissolution of lidocaine from MCM41-NH_2 was faster than that from MCM-41 probably due to different particles agglomeration in the case of amine-modified MCM-41. *Ex vivo* skin permeation was performed to explore the permeation ability of lidocaine through the skin and the results showed that MCM41-NH_2 resulted in enhanced lidocaine permeation with respect to MCM-41. The higher permeation of MCM41-NH_2 was attributed to the positively charged surface of MCM41-NH_2, which favors the absorption of the drug due to the electrostatic interactions between MCM41-NH_2 and the negatively charged skin.

To avoid the side effects associated with systemic administration of methotrexate (MTX) and improve its the cutaneous absorption, *Sapino et al.* [57] developed MTX-based formulations for the topical treatment of skin disorders. For this purpose, MCM-41 nanoparticles with average diameter of 200 nm were prepared and loaded with MTX through an impregnation method. The *in vitro* release profile obtained under physiological skin conditions (pH 6.5, 34 ± 1 °C) indicated that MTX release from MCM-41 was delayed, compared to free MTX (5–24 h), due to the weak drug-matrix interactions exiting between the silanol groups and the drug molecules. An *ex-vivo* study on porcine skin was performed using Franz cells to assess skin penetration. The study was carried out using phosphate buffer, pure shea butter, glycerolipidic lotions and several oil in water (O/W) and water in oil (W/O) emulsions as dermal formulations for the MTX-loaded silica nanoparticles. It was observed that epidermal accumulation of MTX was increased by its inclusion into MCM-41. Moreover, SEM analyses revealed traces of silica aggregates with a micrometric range on the epidermal side of the dermatomed skin slices, which highlights the ability of MS in overcoming the SC and reaching deeper epidermal layers. The authors concluded that the formation of

such silica aggregates may slow down the systemic absorption of silica and act a reservoir in the epidermal layers for prolonged release of the entrapped drug.

Ambrogi et al. [58] developed a topical formulation based on mesoporous silica for the delivery of econazole nitrate (ECO), a drug used in the treatment of fungal infections, whose efficacy is limited by its poor aqueous solubility and dissolution rate. MCM-41 with a size particle in the range of 3-6 μm was prepared and loaded with ECO through the melting method. *In vitro* dissolution tests and in vitro antifungal activity were performed using different formulations containing ECO-loaded MCM-41. The results showed a remarkable improvement in the dissolution rate of ECO as well as a higher antifungal activity when compared to the commercial product. Moreover, a storage stability study performed after 30-day indicated that the drug contained in MCM-41 pores maintained its original physical state.

1.3.3 MS and photoprotection

UV radiations (UVA and UVB) have beneficial effects for the skin, such as production of vitamin D, a vitamin essential to human health. However, excessive exposure to such radiations could cause serious skin disorders such as burns, skin cancer and photoaging [59]. Therefore, topical application of agents able to provide protection to the skin against these radiations is necessary. Currently used sunscreen ingredients for active UVA and UVB protection of the skin include both inorganic nanoparticles such as, ZnO and TiO_2 nanoparticles, which can protect the skin by absorbing, reflecting and scattering UV radiations, as well as organic molecules which act as UV absorbers. However, the increasing concern regarding the adverse health and environmental effects of conventional sunscreen ingredients has promoted the search for safer alternatives.

Generally, toxicity of inorganic materials such as ZnO and TiO_2 nanoparticles is ascribed to their reduced size, which results in a high photocatalytic activity and generation of highly oxidizing radicals and other reactive oxygen species (ROS) that are known to be cytotoxic and/or genotoxic [60]. Therefore, to reduce their toxicity, researchers suggested to modify the surface of these nanoparticles through direct coating with compounds such as alumina, silica, and zirconia that can form hydrated oxides able to capture hydroxyl radicals and thus reduce photosensitivity [60–62]. For example, to increase the safety of ZnO, *Sotiriou et al.* [63] suggested the

coating of ZnO with silica layers. The results of the study showed that the presence of silica coating did not influence the optoelectronic properties of ZnO nanorods, which make them suitable for UV blocking applications. In addition, the toxicological data indicated that the silica-coating on the ZnO nanorods reduced the strong DNA damage that is otherwise observed for the pure uncoated ZnO nanorods.

As far as organic sunscreens are concerned, these are usually classified with respect to the mostly absorbed radiation, i.e. they are divided into UVA (e.g., benzophenones, anthranilates and dibenzoylmethanes) or UVB filters (e.g., salicylates, cinnamates and camphor derivatives) [60]. However, these compounds suffer from limited lifetime due to photodegradation and they can also be phototoxic or photo-allergenic [64]. One approach to improve their stability and reduce their toxicity is to encapsulate these molecules in different matrices. In the study conducted by *Tolbert et al.* [64], hybrid organic/inorganic silica particles encapsulating salicylate and curcuminoid sunscreens were prepared. The effect of the incorporation method on dye leaching, UV stability, and UV protective ability of organic sunscreens was then investigated. The authors showed that presence of a covalent attachment, particularly with the bridged sunscreen monomers, could decrease leaching and photodegradation, so demonstrating that encapsulation of organic sunscreens in silica nanoparticles can provide them longer lifetime. In a similar work, *Wu et al.* [65] reported the incorporation of octyl methoxy cinnamates (OMC), one of the most used Ultraviolet B (UVB) filters, in silica particles.

Antioxidants such as flavonoids have received a great deal of attention in sunscreen formulations due to their anti-inflammatory, antioxidant, anticancer and sun protection properties. However, their cutaneous use is limited by their low solubility, poor stability, and weak release after application [32]. To overcome these drawbacks different researchers proposed the use of MS particles as topical carriers to maintain the physico-chemical and biological properties of the active ingredients until their release on the skin is completed. In *Berlier et al.* work [66], MCM-41 and aminopropyl functionalized MCM-41 were employed to prepare inclusion complexes with rutin. The result of the *ex vivo* experiments showed a greater accumulation in porcine skin in the case of rutin complexed with NH_2-MCM-41. In addition, antioxidant properties of rutin were maintained after immobilization, and the metal-chelating activity was higher in the case of aminopropyl silica. A similar result was achieved by *Sapino et al.* [67] who evaluated the potential of aminopropyl functionalized mesoporous silica nanoparticles (NH_2-MSN) as topical carriers for

quercetin delivery. The results of the study showed that immobilization of quercetin in NH_2-MSN improved its photostability.

1.3.4 MS and skin cancer

Skin cancer represents one of the leading types of cancers in the world, which causes a high impact on the global burden of health and the economy [68]. There are two main types of skin cancer: (1) the melanomas, which originate from the melanocytes and are caused either by the exposure to harmful ultraviolet radiation or by mutations in several genes, (2) the non-melanomas, which originate from epidermally-derived cells and are mainly caused by alterations in the hedgehog pathway or by genotoxic stress and the consequent DNA damage [69]. Various approaches including surgical excision, radiation chemotherapy and phototherapy exist for treating skin cancer. Surgical procedures such as cryosurgery, laser therapy and curettage are still considered the best standard treatment of any type of skin cancer. However, they can cause complications like pain, serious disfigurement, chronic ulcer formation, blister formation, hypopigmentation, scarring and radiodermatitis with nonhealing ulcerations. Moreover, surgical treatment results inadequate for lesions that are spread all over the body. In such cases, topical, or systemic chemotherapy, radiation or photodynamic therapy (PDT) represent alternative approaches for skin cancer treatment [68].

Generally, topical therapies are used when there are multiple lesions, the treatment area is large, or for lesions that take long time to heal. However, the efficacy of topical drugs is much lower compared to the surgical removal of cancers. In addition, available topical therapies do not allow the drugs penetrate well the skin barrier and consequently they require frequent and prolonged applications, which could result in the development of severe inflammation and/or high systemic toxicity. To overcome these drawbacks, nanostructured materials were studied as carriers for topical treatment of skin cancers. These systems can improve both skin and tumor penetration of bioactive molecules and enhance drug retention in the skin and tumor, resulting in reduced dosage and minimal toxicity [70]. Different nanoparticles were tested for the treatment of skin cancers. They include liposomes, dendrimers, carbon-based nanoparticles, inorganic nanoparticles, and protein-based nanoparticles. Among them, MS-based materials have gained growing interest as

an efficient drug delivery system, owing to their outstanding properties, for the treatment of skin cancer using various types of therapies [71].

Ferreira et al. [72] investigated the antitumor efficiency of indomethacin (IND) incorporated into mesoporous silica nanoparticles (MSNPs), and the toxic effect of the treatments in melanoma-bearing mice. The results suggested that the treatment with MSNPs + IND could inhibit tumor growth and decrease the frequency of mitosis in tumor tissues compared to the treatment with only IND. In addition, a genotoxicity study indicated the absence of noticeable systemic toxicity of MSNPs + IND.

To improve the bioavailability of Resveratrol (RES), a natural polyphenol with recognized anti-cancer properties, *Marinheiro et al.* [73] prepared RES-loaded MS nanoparticles (MSNs) and investigated their therapeutic potential in the treatment of human melanoma. RES was efficiently encapsulated (efficiency > 93%) into spheroidal MSNs (size~60 nm) using the rotary evaporation method. The loading favored the formation of amorphous RES, resulting in an enhanced RES release from encapsulated RES compared to the bulk form. The authors found that RES release was pH-dependent, and it was faster at pH 5.2 than at pH 7.4; this behavior is of high interest as some tumors exhibit acidic environment. Finally, *in vitro* cytotoxicity studies on human A375 and MNT-1 melanoma cellular cultures were performed, and they showed a decrease in the cell viability with increasing concentration of RES-loaded MSNs, indicating the potent action of the released RES in both cell lines.

1.4 MS and wound healing

As previously reported, skin is the largest organ in the human body, it accounts for about 10 - 15 % of the total body weight in adults and covers a surface area of approximately 1.7 m^2 [37]. It plays an important role in maintaining bodies homeostasis by regulating temperature and water loss. Eventually, it also carries out a neurosensory function thanks to specific receptors for heat, touch and pain [74,75]. Since skin is always in contact with the external environment, it is understandable that it could undergo different damages[76]. Although skin possesses optimal regenerative ability, in some cases, different underlying pathologies such as diabetes, could impair the healing process so resulting in non-healed wounds [77]. Cutaneous injuries, in particular chronic wounds and burns are considered one of

the most common lesions, which affect a lot of people every year all over the world. In recent years, the prevalence of people suffering from chronic wounds has dramatically increased due to the growing incidence of obesity, chronic diseases, and aging population. It has been estimated that chronic wounds affect about 1-2 % of the European and USA population[76]. Non-healing wounds not only limit the physiological functions of the skin barrier but can also lead to awful consequences such as severe infections, amputations or even death. The treatment of these wounds represents a burden for the healthcare system as it requires intensive and long-term care with high-cost products. In the USA, it was estimated that over $25 billion are annually spent to manage chronic wounds.

Various strategies, which include traditional therapies, such as the application of natural substances, as well as modern approaches, such as the hyperbaric oxygen therapy, are employed in wound treatment. However, most of them results inadequate or expensive; therefore, there is still a need to develop alternative therapies for trying to enhance the wound healing process[78,79]. Due to the progress in micro and nanotechnology, various drug delivery systems based on lipids, polymers and inorganic particles have emerged as an alternative approach to enhance skin regeneration. In particular, MS-based materials have gained much attention due to their unique properties and biocompatibility[32].

1.4.1 The wound healing process

Wound healing is a natural physiological process that aims at restoring skin integrity. It is a dynamic phenomenon, which involves complex interactions between different cell types, extracellular matrix components, growth factors, and cytokines. Generally, the wound healing process is divided into four overlapping phases (figure 1.10) [79], which are briefly described below:

1. ***Hemostasis*** occurs immediately after a trauma to skin. During this phase, vasoconstriction occurs to minimize blood loss [79]. At the same time, intravascular plasma platelets aggregate to form a clot at the wound site to stop bleeding. Furthermore, platelets release different growth factors, which include epidermal growth factor (EGF), insulin-like growth factor 1 (IGF 1), platelet-derived growth factor (PDGF), and fibroblast growth factor (FGF). These factors act as wound healing promotors by attracting and

activating white blood cells, endothelial cells, and fibroblasts, which are involved in the following phase [76,80].

2. The ***inflammatory phase*** is the second stage of wound healing and starts once hemostasis is achieved. The aim of this phase is to establish an immune barrier against pathogens to protect the skin from infections [80]. It lasts two to five days after skin trauma [76]. During the inflammatory phase, local blood vessels dilate to increase vascular permeability, which allows the wound site to be occupied by white blood cells [81]. Neutrophils are the first population of white blood cells that reach the wound. They secrete various proteases and antimicrobial peptides within the wound to decontaminate and remove damaged cells, pathogens, bacteria, and all foreign material from the wound. Upon completing their job, neutrophils undergo spontaneous apoptosis as their prolonged presence in the injured site could impair the wound healing process so leading to the conversion of an acute wound into a nonhealing chronic wound [82]. After that, monocytes predominate the wound site, and they differentiate into macrophages. Macrophages remove apoptotic neutrophils and other dead cells. In addition, they secrete different growth factors, including TGF-β, TGF-α, basic FGF (bFGF), VEGF and PDGF, which stimulate wound healing by inducing cell proliferation, synthesis of ECM and angiogenesis [82].

3. The ***proliferative phase*** starts around two days after the injury, and it persists for two or three weeks. In this phase, the wound area is rebuilt with new tissue composed of collagen and extracellular matrix [82]. During this phase, a new network of blood vessels and capillaries is formed due to the action of proangiogenic factors, such as PDGF, released by inflammatory cells in the wound during the previous phase [76]. At the same time, fibroblasts proliferate and produce different components including proteins collagen, fibronectin, and hyaluronic acid, which are necessary for the formation of the granulation tissue [82]- The color of the granulation tissue is considered an indicator of tissue health: a pink or red color usually indicates a healthy granulation tissue, while a dark-colored tissue is typically a sign of an infected or ischemic wound. In addition, some fibroblasts differentiate into myofibroblasts, which cause wound contraction by pulling the wound edging and promoting wound healing. The final stage of the proliferative phase is re-epithelialization when epithelial cells proliferation and migration occur so resulting in the coverage of the wound area. Typically, re-

epithelialization is more efficient and faster when the wound environment is kept moist and hydrated [79].

4. The ***maturation phase***, also known as *remodeling phase*, is the final stage of the wound healing process. It begins around three weeks after the injury, and it may last months or years, depending on the complexity of the wound. In this phase, the collagen type III present in the extracellular matrix is replaced by collagen type I, which further evolves into a more organized structure with enhanced tensile strength. The cells, blood capillaries, macrophages and fibroblasts that had been involved in the previous stages and are no longer needed are removed from the wound site by apoptosis [76,79]. The final result is a fully maturated scar with a low number of cells and blood vessels and a tensile strength of about 80 % of the strength of unwound tissue [80].

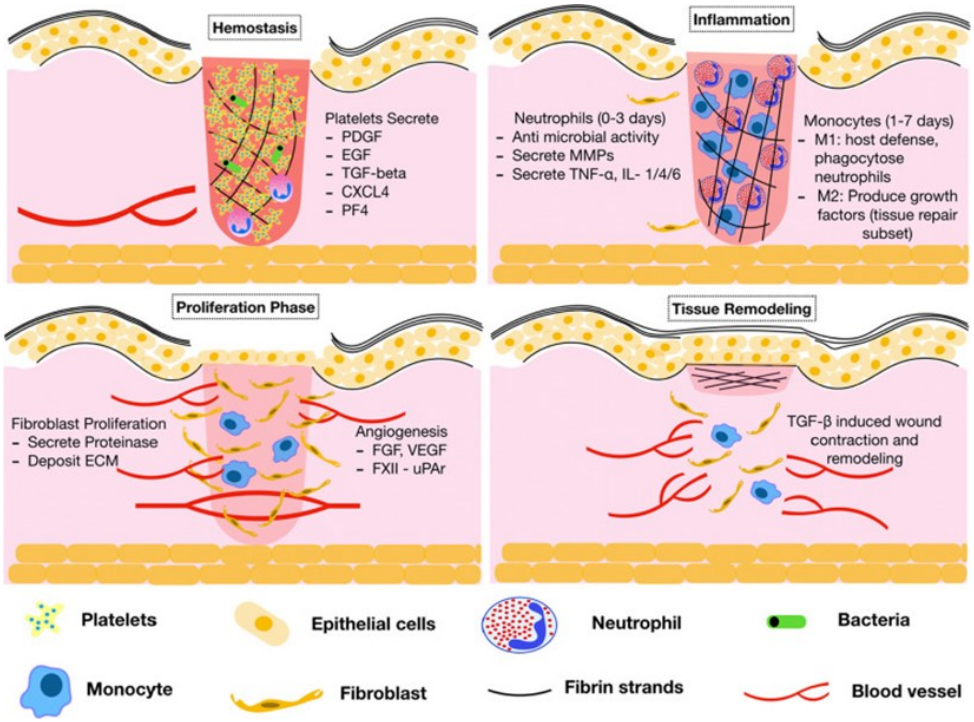

Figure 1.10 The different phases of the wound healing process [83].

1.4.2 Wound classification

A wound can be defined as a damage or disruption to the normal anatomical structure and function of the skin, which may result from physical, chemical, thermal damage or from the presence of an underlying pathological condition[80,84–86].

A skin wound can be classified according to different criteria including healing time and degree of contamination. Healing time represents an important factor in wound management. Based on their time frame of healing, wounds fall into two categories: acute wounds and chronic wounds [80]. Acute wounds are tissue damages usually caused by mechanical injuries, surgical procedures, burns and chemical injuries. These wounds heal following the physiological healing pathway within the expected time frame (8-12 weeks), with minimal scarring and complete restoration of the anatomical structure and functions of the skin.

Chronic wounds are injuries that fail to heal through the normal phases of the wound healing process in a timely manner or wounds that progress through the healing process without restoring the anatomic and functional results[86]. The pathophysiology of chronic wounds is still unclear, but it is known that their insurgence is associated with a prolonged inflammation state that stimulates a continuous recruitment of inflammatory cells at the wound site, with a resultant increased production of proteases and ROS [87]. The presence of high levels of proteases and ROS in the wound bed leads to the destruction of the ECM and damage of the proteins so impeding wound healing. Chronic wounds usually arise from various underlying pathological conditions such as diabetes, arterial and venous insufficiency, and vasculitis [78,87].

1.4.3 MS in wound healing applications

Silicon is the third most common trace element in the human body after iron and zinc. However, unlike iron and zinc, its biochemical and physiological functions are still unknown. For this reason, there is an increasing interest in understanding the biological and therapeutic effects of silicon on the human body. It has been suggested that silicon could have a pivotal role in maintaining skin and bone health since high levels of this element are found in these tissues [88,89]. Indeed, *Seaborn et al.* [90] reported that silicon deficiency could affect wound repair by decreasing the

synthesis of collagen. Moreover, some studies reported that silicon supplementation could improve skin and bone health [91–93]. In light of these consideration, various silicon-based devices, which include silicone gels [94] and bioactive glass ointments [95], have been studied for wound healing applications.

In particular, MS represents a promising candidate for wound healing applications, as it can act in different ways. The first mechanism is related with fact that, in an aqueous environment, silica reacts with water and forms orthosilicic acid, a small molecule that represents the main source of silicon for both humans and animals. In a study conducted by *Quignard et al.* [96], the effect of soluble silicic acid and silica nanoparticles (NPs) with different degrees of surface charge and dissolution rates on the migration and proliferation of human skin fibroblasts cells, which are two processes involved in wound healing, was investigated. The results of the study showed that silica-treated cells were able to migrate and proliferate more rapidly than the untreated control ones. In particular, positively charged silica NPs were more efficient in promoting wound closure with respect to soluble silicic acid alone, suggesting that the particles themselves could have a beneficial effect on wound closure beyond being simply a source of silicic acid in the medium. The authors suggested that silicic acid is the bioactive form of silica, but it is slowly taken up by the cells so leading to a delay in wound healing. On the other hand, positively charged silica NPs are easily internalized by the cells and dissolved intracellularly, which results in the release of silicic acid inside the cells. The ability of silica NPs to promote wound closure was also investigated by *Mytych et al.* [97]. The result of their study indicated that low doses of silica NPs were able to increase the proliferation and metabolic activity of human facial skin fibroblasts, leading to an improvement in the *in vitro* wound healing ability. In another approach, *Pan et al.* [98] designed a new tissue adhesive based on MS particles for wound healing. The authors noted that MS nanoparticles (MSNs) could form a nanocomposite with body fluids in the wound site. The formation of this nanocomposite allowed the reconnection of the wound edges without the need of sutures to be obtained. They also demonstrated that MSN could induce a proper inflammatory response, which allowed the infiltration of inflammatory cells and fibroblasts to be achieved so accelerating the healing process. Finally, the authors observed that the elimination of MSNs occurred at a rate that is compatible with tissue regeneration. The elimination rate of adhesives represents an important aspect since too slow elimination of these material generally leads to the insurgence of chronic inflammation, which consequently results in delayed healing.

MS may influence the wound healing process in a second way. In fact, owing to their unique physicochemical properties and high loading capacity, mesoporous silica can be loaded with different bioactive molecules, aiming at obtaining a device with enhanced wound healing properties. *Hamam et al.* [99] investigated the efficiency of a curcumin-loaded mesoporous silica as an *in vivo* wound healing agent. The results of the study indicated that the developed systems could enhance wound healing by inhibiting the inflammatory response, stimulating angiogenesis, inducing fibroblast proliferation as well as enhancing reepithelization and synthesis of collagen. In a recent study, *Masood et al.* [100] designed a device based on MSN loaded with salicylic acid and ketoconazole for the treatment of highly resistant fungal infections. The developed system demonstrated enhanced antifungal activity both *in vitro* and *in vivo* as well as a rapid healing of the infection.

Lastly, silicas can also be used as additives in different matrices to achieve wound dressing materials with enhanced mechanical properties and/or wound healing capability. For example, *Park et al.* [101] reported the preparation of advanced wound dressing materials based on the hybridization of chitosan with silica (CTS-Si) xerogel, and the evaluation of their wound healing capability through *in vitro* and *in vivo* tests. The *in vitro* tests showed that the material could improve fibroblast proliferation with respect to pure chitosan and other commercial dressing materials such as gauze, polyurethane (PU), and silver-containing hydro-fiber (HF-Ag). Moreover, the results of the *in vivo* test performed using rat models, indicated that CTS-Si sponges were able to stimulate the recruitment of the inflammatory cells to the wound site due to the release of silicon ions from the sponge, leading to enhanced secretion of growth factors (TGF-beta) during the early stage. The release of TGF-beta is necessary as it promotes fibroblasts proliferation and consequently accelerates wound closure. In another work performed by the same research group, the therapeutic effect of chitosan-silica hybrid membranes was investigated using a full-thickness skin wound in a porcine model to predict their behavior in human skin treatment. Pig skin was used as it is very similar to human skin from an anatomical, physiological, biochemical, and immunological point of view. The authors demonstrated that CTS-Si membranes were also efficient in large-scale animal models, suggesting that this material could be effective for the treatment of cutaneous wounds in humans [102]. Similarly, *Song et al.* [103] developed a polyurethane-silica (PU-Si) hybrid foam in order to improve the poor healing ability of polyurethane-based dressing materials. The authors reported that the presence of silica significantly improved the mechanical properties of the fabricated material,

which resulted in better flexibility and durability when compared with pure PU. The healing capability of the PU-Si was studied with the in vivo excision wound model. The results of the test indicated that the full thickness wounds treated with PU-Si foams showed faster wound closure rate and accelerated collagen and elastin fibers regeneration in the new tissue, suggesting that PU-Si hybrid foams could be considered a promising material for wound treatment.

1.5 Conclusions

This chapter provided a general overview of MS properties and their applications in the dermatological field, focusing on the use of MS in the treatment of various skin conditions. Particular attention was given to the employment of MS in the field of wound healing. From the analysis of the literature, it has emerged that MS materials have been widely studied to produce more effective wound dressing since they can act as drugs that are intrinsically involved in the therapy of the wound healing process as well as carriers to deliver bioactive agents for wound treatment.

In this context, the present PhD thesis aims at studying the use of MS spheres as a material to develop drug delivery systems that combine the beneficial intrinsic effects of the MS spheres with the therapeutic effects of the supported drug in the prospect of future wound healing applications.

1.6 References

1. Kumar, S., Malik, M. M. & Purohit, R. Synthesis Methods of Mesoporous Silica Materials. *Mater. Today Proc.* **4**, 350–357 (2017).
2. Jibowu, T. A Review on Nanoporous Metals. *Front. Nanosci. Nanotechnol.* **2**, 165-168 (2016).
3. Mirzaei, M. *et al.* Silica Mesoporous Structures: Effective Nanocarriers in Drug Delivery and Nanocatalysts. *Appl. Sci.* **10**, 7533 (2020).
4. Ding, Q. & Hu, X. Mesoporous Materials as Catalyst support for Wastewater Treatment. *Madridge J. Nanotechnol. Nanosci.* **4**, 160–167 (2019).
5. Sábio, R. M., Meneguin, A. B., Martins dos Santos, A., Monteiro, A. S. & Chorilli, M. Exploiting mesoporous silica nanoparticles as versatile drug carriers for several routes of administration. *Microporous Mesoporous Mater.* **312**, 110774 (2021).
6. Farjadian, F., Roointan, A., Mohammadi-Samani, S. & Hosseini, M. Mesoporous silica nanoparticles: Synthesis, pharmaceutical applications, biodistribution, and biosafety assessment. *Chem. Eng. J.* **359**, 684–705 (2019).
7. Mamaeva, V., Sahlgren, C. & Lindén, M. Mesoporous silica nanoparticles in medicine-Recent advances. *Adv. Drug Deliv. Rev.* **65**, 689–702 (2013).
8. Narayan, R., Nayak, U. Y., Raichur, A. M. & Garg, S. Mesoporous silica nanoparticles: A comprehensive review on synthesis and recent advances. *Pharmaceutics* **10**, 1–49 (2018).
9. Witharana, C. & Wanigasekara, J. Drug Delivery Systems: A New Frontier in Nano-technology. *Int. J. Med. Res. Heal. Sci.* **6**, 11–14 (2017).
10. Bhagwat, R. R. & Vaidhya, I. S. Novel Drug Delivery Systems: An Overview. *Int. J. Pharm. Sci. Res.* **4**, 970–982 (2013).
11. Mitchell, M. J. *et al.* Engineering precision nanoparticles for drug delivery. *Nat. Rev. Drug Discov.* **20**, 101–124 (2021).
12. Vallet-Regi, M., Rámila, A., del Real, R. P. & Pérez-Pariente, J. A New Property of MCM-41: Drug Delivery System. *Chem. Mater.* **13**, 308–311 (2001).
13. Žid, L. *et al.* Mesoporous Silica as a Drug Delivery System for Naproxen:

Influence of Surface Functionalization. *Molecules* **25**, 4722 (2020).

14. Mosselhy, D. A. et al. Silica–gentamicin nanohybrids: combating antibiotic resistance, bacterial biofilms, and in vivo toxicity. *Int. J. Nanomedicine* Volume **13**, 7939–7957 (2018).

15. Roik, N. V, Belyakova, L. A. & Dziazko, M. O. Adsorption of antitumor antibiotic doxorubicin on MCM-41-type silica surface. *Adsorpt. Sci. Technol*. **35**, 86–101 (2017).

16. Wang, Y. et al. Mesoporous silica nanoparticles in drug delivery and biomedical applications. Nanomedicine Nanotechnology, *Biol. Med.* **11**, 313–327 (2015).

17. Zhou, Y. et al. Mesoporous silica nanoparticles for drug and gene delivery. *Acta Pharm. Sin. B* **8**, 165–177 (2018).

18. V. Chiola, J.E. Ritsko, C. D. V. Process for producing low-bulk density silica. (1969).

19. Savic, S. et al. Hard Template Synthesis of Nanomaterials Based on Mesoporous Silica. *Metall. Mater. Eng.* **24**, 225-241 (2018).

20. Alothman, Z. A. A review: Fundamental aspects of silicate mesoporous materials. *Materials* **5**, 2874–2902 (2012).

21. Mohamed Isa, E. D., Ahmad, H., Abdul Rahman, M. B. & Gill, M. R. Progress in Mesoporous Silica Nanoparticles as Drug Delivery Agents for Cancer Treatment. *Pharmaceutics* **13**, 152 (2021).

22. Ghaferi, M. et al. Mesoporous silica nanoparticles: synthesis methods and their therapeutic use-recent advances. *J. Drug Target.* **29**, 131–154 (2021).

23. Chircov, C. *et al.* Mesoporous Silica Platforms with Potential Applications in Release and Adsorption of Active Agents. *Molecules* **25**, 3814 (2020).

24. Asefa, T. & Tao, Z. Biocompatibility of Mesoporous Silica Nanoparticles. *Chem. Res. Toxicol.* **25**, 2265–2284 (2012).

25. Werner, S. & Arthur, F. Controlled Growth of Monodisperse Silica Spheres in the Micron Size Range. *J. Colloid Interface Sci.* **26**, 62–69 (1968).

26. Ghimire, P. P. & Jaroniec, M. Renaissance of Stöber method for synthesis of colloidal particles: New developments and opportunities. *J. Colloid Interface Sci.* **584**, 838–865 (2021).

27. Downing, M. A. & Jain, P. K. Mesoporous silica nanoparticles: Synthesis, properties, and biomedical applications. Nanoparticles for Biomedical Applications: Fundamental Concepts, Biological Interactions and Clinical Applications (Elsevier Inc., 2019).

28. Grun, M., Lauer, I. & Unger, K. K. The Synthesis of Micrometer- and Submicrometer-Size Spheres of Ordered Mesoporous Oxide MCM-41. *Adv. Mater.* **9**, 254–257 (1997).

29. Pal, N. & Bhaumik, A. Soft templating strategies for the synthesis of mesoporous materials: Inorganic, organic-inorganic hybrid and purely organic solids. *Adv. Colloid Interface Sci.* **189**–**190**, 21–41 (2013).

30. Huang, B., Schliesser, J., Olsen, R., Smith, S. & Woodfield, B. Synthesis and Thermodynamics of Porous Metal Oxide Nanomaterials. *Curr. Inorg. Chem.* **4**, 40–53 (2014).

31. Gupta, M., Agrawal, U. & Vyas, S. P. Nanocarrier-based topical drug delivery for the treatment of skin diseases. *Expert Opin. Drug Deliv.* **9**, 783–804 (2012).

32. Arriagada, F., Nonell, S. & Morales, J. Silica-based nanosystems for therapeutic applications in the skin. *Nanomedicine* **14**, 2243–2267 (2019).

33. Lim, H. W. *et al.* The burden of skin disease in the United States. *J. Am. Acad. Dermatol.* **76**, 958-972.e2 (2017).

34. Sanjay, C., Ghate, V. M. & Lewis, S. A. Mesoporous silica particles for dermal drug delivery: A review. *Int. J. Appl. Pharm.* **10**, 23–26 (2018).

35. Prow, T. W. *et al.* Nanoparticles and microparticles for skin drug delivery. *Adv. Drug Deliv. Rev.* **63**, 470–491 (2011).

36. Aljghami, M. E., Saboor, S. & Amini-Nik, S. Emerging Innovative Wound Dressings. *Ann. Biomed. Eng.* **47**, 659–675 (2019).

37. Benson, H. A. E., Mohammed, Y., Grice, J. E. & Roberts, M. S. *Formulation Effects on Topical Nanoparticle Penetration*. *Nanoscience in Dermatology* (2016).

38. Agarwal S, Krishnamurthy K. *Histology, Skin. [Updated 2021 May 10]. In: StatPearls [Internet]. Treasure Island (FL): StatPearls Publishing; 2021 Jan. Available from: https://www.ncbi.nlm.nih.gov/books/NBK537325/.*

39. Nastiti, C. M. R. R. *et al.* Topical nano and microemulsions for skin delivery.

Pharmaceutics **9**, 1–25 (2017).

40. Goyal, R., Macri, L. K., Kaplan, H. M. & Kohn, J. Nanoparticles and nanofibers for topical drug delivery. *J. Control. Release* **240**, 77–92 (2016).

41. PDQ® Adult Treatment Editorial Board. PDQ Melanoma Treatment. Bethesda, MD: National Cancer Institute. Available at: https://www.cancer.gov/types/skin/patient/melanoma-treatment-pdq. [PMID: 26389388].

42. Joshi, M., Butola, B. S. & Saha, K. Advances in Topical Drug Delivery System: Micro to Nanofibrous Structures. *J. Nanosci. Nanotechnol.* **14**, 853–867 (2014).

43. Alkilani, A., McCrudden, M. T. & Donnelly, R. Transdermal Drug Delivery: Innovative Pharmaceutical Developments Based on Disruption of the Barrier Properties of the Stratum Corneum. *Pharmaceutics* **7**, 438–470 (2015).

44. Leppert, W., Malec–Milewska, M., Zajaczkowska, R. & Wordliczek, J. Transdermal and Topical Drug Administration in the Treatment of Pain. *Molecules* **23**, 681 (2018).

45. Olldashi, F. *et al.* Effects of tranexamic acid on death, vascular occlusive events, and blood transfusion in trauma patients with significant haemorrhage (CRASH-2): A randomised, placebo-controlled trial. *Lancet* **376**, 23–32 (2010).

46. Palmer, B. & DeLouise, L. Nanoparticle-Enabled Transdermal Drug Delivery Systems for Enhanced Dose Control and Tissue Targeting. *Molecules* **21**, 1719 (2016).

47. Jain, S., Patel, N., Shah, M. K., Khatri, P. & Vora, N. Recent Advances in Lipid-Based Vesicles and Particulate Carriers for Topical and Transdermal Application. *J. Pharm. Sci.* **106**, 423–445 (2017).

48. Nigro, A. et al. Dealing with skin and blood-brain barriers: The unconventional challenges of mesoporous silica nanoparticles. *Pharmaceutics* 10, 250 (2018).

49. Valetti, S. et al. Can mesoporous nanoparticles promote bioavailability of topical pharmaceutics? *Int. J. Pharm.* **602**, 120609 (2021).

50. Rancan, F. *et al.* Skin Penetration and Cellular Uptake of Amorphous Silica Nanoparticles with Variable Size, Surface Functionalization, and Colloidal

Stability. *ACS Nano* **6**, 6829–6842 (2012).

51. Jung, E. *et al.* Effect of iron and silica nanoparticles' size on in vitro human skin binding and penetration. *Toxicol. Res. Appl.* **3**, 239784731989305 (2019).

52. Boonen, J.; Baert, B.; Lambert, J.; De Spiegeleer, B. Skin penetration of silica microparticles. *Int. J. Pharm. Sci.* **66**, 463–464 (2011).

53. Patzelt, A. *et al.* Selective follicular targeting by modification of the particle sizes. *J. Control. Release* **150**, 45–48 (2011).

54. Patzelt, A., Knorr, F., Blume-Peytavi, U., Sterry, W. & Lademann, J. Hair follicles, their disorders and their opportunities. *Drug Discov. Today Dis. Mech.* **5**, e173–e181 (2008).

55. Lademann, J. *et al.* Hair Follicles – A Long-Term Reservoir for Drug Delivery. *Skin Pharmacol. Physiol.* **19**, 232–236 (2006).

56. Nafisi, S., Samadi, N., Houshiar, M. & Maibach, H. I. Mesoporous silica nanoparticles for enhanced lidocaine skin delivery. *Int. J. Pharm.* **550**, 325–332 (2018).

57. Sapino, S., Oliaro-Bosso, S., Zonari, D., Zattoni, A. & Ugazio, E. Mesoporous silica nanoparticles as a promising skin delivery system for methotrexate. *Int. J. Pharm.* **530**, 239–248 (2017).

58. Ambrogi, V. *et al.* Econazole Nitrate-Loaded MCM-41 for an Antifungal Topical Powder Formulation. *J. Pharm. Sci.* **99**, 4738–4745 (2010).

59. Sivamani, R. K., Crane, L. A. & Dellavalle, R. P. The Benefits and Risks of Ultraviolet Tanning and Its Alternatives: The Role of Prudent Sun Exposure. *Dermatol. Clin.* **27**, 149–154 (2009).

60. Serpone, N., Dondi, D. & Albini, A. Inorganic and organic UV filters: Their role and efficacy in sunscreens and suncare products. *Inorganica Chim. Acta* **360**, 794–802 (2007).

61. Zaccariello, G. *et al.* Bismuth titanate-based UV filters embedded mesoporous silica nanoparticles: Role of bismuth concentration in the self-sealing process. *J. Colloid Interface Sci.* **549**, 1–8 (2019).

62. Knežević, N. Ž., Ilić, N., Dokić, V., Petrović, R. & Janaćković, D. Mesoporous Silica and Organosilica Nanomaterials as UV-Blocking Agents. *ACS Appl. Mater. Interfaces* **10**, 20231–20236 (2018).

63. Sotiriou, G. A. *et al.* Engineering safer-by-design silica-coated ZnO nanorods with reduced DNA damage potential. *Environ. Sci. Nano* **1**, 144 (2014).

64. Tolbert, S. H., McFadden, P. D. & Loy, D. A. New Hybrid Organic/Inorganic Polysilsesquioxane–Silica Particles as Sunscreens. *ACS Appl. Mater. Interfaces* **8**, 3160–3174 (2016).

65. Wu, P.-S., Lee, Y.-C., Kuo, Y.-C. & Lin, C.-C. Development of Octyl Methoxy Cinnamates (OMC)/Silicon Dioxide (SiO2) Nanoparticles by Sol-Gel Emulsion Method. *Nanomaterials* **7**, 434 (2017).

66. Berlier, G. *et al.* MCM-41 as a useful vector for rutin topical formulations: Synthesis, characterization and testing. *Int. J. Pharm.* **457**, 177–186 (2013).

67. Sapino, S. *et al.* Mesoporous silica as topical nanocarriers for quercetin: characterization and in vitro studies. *Eur. J. Pharm. Biopharm.* **89**, 116–125 (2015).

68. Trinh, H. T. *et al.* Silica-based nanomaterials as drug delivery tools for skin cancer (melanoma) treatment. *Emergent Mater.* 1067–1092 (2021).

69. Lalan, M. *et al.* Skin cancer therapeutics: nano-drug delivery vectors—present and beyond. *Futur. J. Pharm. Sci.* **7**, 179 (2021).

70. Krishnan, V. & Mitragotri, S. Nanoparticles for topical drug delivery: Potential for skin cancer treatment. *Adv. Drug Deliv. Rev.* **153**, 87–108 (2020).

71. Dianzani, C. *et al.* Drug Delivery Nanoparticles in Skin Cancers. *Biomed Res. Int.* **2014**, 1–13 (2014).

72. Ferreira, N. H. *et al.* Anti-Melanoma Activity of Indomethacin Incorporated into Mesoporous Silica Nanoparticles. *Pharm. Res.* **37**, 172 (2020).

73. Marinheiro, D., Ferreira, B., Oskoei, P., Oliveira, H. & Daniel-da-Silva, A. Encapsulation and Enhanced Release of Resveratrol from Mesoporous Silica Nanoparticles for Melanoma Therapy. *Materials (Basel).* **14**, 1382 (2021).

74. Yousef H, Alhajj M, Sharma S. Anatomy, Skin (Integument), Epidermis. [Updated 2021 Jul 26]. In: StatPearls [Internet]. Treasure Island (FL): StatPearls Publishing; 2021 Jan. Available from: https://www.ncbi.nlm.nih.gov/books/NBK470464/.

75. Larese Filon, F., Mauro, M., Adami, G., Bovenzi, M. & Crosera, M.

Nanoparticles skin absorption: New aspects for a safety profile evaluation. *Regul. Toxicol. Pharmacol.* **72**, 310–322 (2015).

76. Wang, W., Lu, K. J., Yu, C. H., Huang, Q. L. & Du, Y. Z. Nano-drug delivery systems in wound treatment and skin regeneration. *J. Nanobiotechnology* **17**, 1–15 (2019).

77. Saghazadeh, S. *et al.* Drug delivery systems and materials for wound healing applications. *Adv. Drug Deliv. Rev.* **127**, 138–166 (2018).

78. Kim, H. S. *et al.* Advanced drug delivery systems and artificial skin grafts for skin wound healing. *Advanced Drug Delivery Reviews* vol. **146**, 209–239 (2019).

79. Nethi, S. K., Das, S., Patra, C. R. & Mukherjee, S. Recent advances in inorganic nanomaterials for wound-healing applications. *Biomater. Sci.* **7**, 2652–2674 (2019).

80. Velnar, T., Bailey, T. & Smrkolj, V. The wound healing process: An overview of the cellular and molecular mechanisms. *J. Int. Med. Res.* **37**, 1528–1542 (2009).

81. Han, G. & Ceilley, R. Chronic Wound Healing: A Review of Current Management and Treatments. *Adv. Ther.* **34**, 599–610 (2017).

82. Thiruvoth, F., Mohapatra, D., Sivakumar, D., Chittoria, R. & Nandhagopal, V. Current concepts in the physiology of adult wound healing. *Plast. Aesthetic Res.* **2**, 250 (2015).

83. Opneja, A., Kapoor, S. & Stavrou, E. X. Contribution of platelets, the coagulation and fibrinolytic systems to cutaneous wound healing. *Thromb. Res.* **179**, 56–63 (2019).

84. Thiel, R. *et al.* NII-Electronic Library Service. *J. Geotech. Geoenvironmental Eng.* **1**, 1–11 (2013).

85. Thakur, R., Jain, N., Pathak, R. & Sandhu, S. S. Practices in Wound Healing Studies of Plants. *Evidence-Based Complement. Altern. Med.* **2011**, 1–17 (2011).

86. Lazarus, G. S. *et al.* Definitions and guidelines for assessment of wounds and evaluation of healing. *Arch. Dermatol.* **130**, 489–493 (1994).

87. Frykberg, R. G. & Banks, J. Challenges in the Treatment of Chronic Wounds. *Adv. Wound Care* **4**, 560–582 (2015).

88. Jurkić, L. M., Cepanec, I., Pavelić, S. K. & Pavelić, K. Biological and therapeutic effects of ortho-silicic acid and some ortho-silicic acid-releasing compounds: New perspectives for therapy. *Nutr. Metab. (Lond).* **10**, 2 (2013).

89. Martin, K. R. Silicon: The Health Benefits of a Metalloid. in 451–473 (2013).

90. Seaborn, C. D. & Nielsen, F. H. Silicon Deprivation Decreases Collagen Formation in Wounds and Bone, and Ornithine Transaminase Enzyme Activity in Liver. *Biol. Trace Elem. Res.* **89**, 251–262 (2002).

91. Macdonald, H. M. *et al.* Dietary silicon interacts with oestrogen to influence bone health: Evidence from the Aberdeen Prospective Osteoporosis Screening Study. *Bone* **50**, 681–687 (2012).

92. Barel, A. *et al.* Effect of oral intake of choline-stabilized orthosilicic acid on skin, nails and hair in women with photodamaged skin. *Arch. Dermatol. Res.* **297**, 147–153 (2005).

93. Jugdaohsingh, R. *et al.* Dietary Silicon Intake Is Positively Associated With Bone Mineral Density in Men and Premenopausal Women of the Framingham Offspring Cohort. *J. Bone Miner. Res.* **19**, 297–307 (2003).

94. Puri, N. & Talwar, A. The efficacy of silicone gel for the treatment of hypertrophic scars and keloids. *J. Cutan. Aesthet. Surg.* **2**, 104 (2009).

95. Lin, C., Mao, C., Zhang, J., Li, Y. & Chen, X. Healing effect of bioactive glass ointment on full-thickness skin wounds. *Biomed. Mater.* **7**, 045017 (2012).

96. Quignard, S., Coradin, T., Powell, J. J. & Jugdaohsingh, R. Silica nanoparticles as sources of silicic acid favoring wound healing in vitro. *Colloids Surfaces B Biointerfaces* **155**, 530–537 (2017).

97. Mytych, J., Wnuk, M. & Rattan, S. I. S. Low doses of nanodiamonds and silica nanoparticles have beneficial hormetic effects in normal human skin fibroblasts in culture. *Chemosphere* **148**, 307–315 (2016).

98. Pan, Z. *et al.* Activating proper inflammation for wound-healing acceleration via mesoporous silica nanoparticle tissue adhesive. *Nano Res.* **13**, 373–379 (2020).

99. Hamam, F. & Nasr, A. Curcumin-loaded mesoporous silica particles as wound-healing agent: An In vivo study. *Saudi J. Med. Med. Sci.* **8**, 17 (2020).

100. Masood, A. *et al.* Pharmaco-Technical Evaluation of Statistically Formulated and Optimized Dual Drug-Loaded Silica Nanoparticles for Improved Antifungal Efficacy and Wound Healing. *ACS Omega* **6**, 8210–8225 (2021).

101. Park, J.-U. *et al.* The accelerating effect of chitosan-silica hybrid dressing materials on the early phase of wound healing. *J. Biomed. Mater. Res. Part B Appl. Biomater.* **105**, 1828–1839 (2017).

102. Park, J. U. *et al.* Acceleration of the healing process of full-thickness wounds using hydrophilic chitosan–silica hybrid sponge in a porcine model. *J. Biomater. Appl.* **32**, 1011–1023 (2018).

103. Song, E.-H. *et al.* Polyurethane-silica hybrid foams from a one-step foaming reaction, coupled with a sol-gel process, for enhanced wound healing. *Mater. Sci. Eng. C* **79**, 866–874 (2017).

PART I

Chapter 2
Mesoporous silica-based materials as hemostatic materials

2.1 Introduction

Uncontrolled bleeding is considered one of the most common causes of potentially preventable death either in the military field, where more than 50 % of battlefield victims result from hemorrhage, or in the civilian arena where it was estimated that severe bleeding is responsible for over 35 % of pre-hospital deaths [1,2]. Besides that, in the case of victims' survival, uncontrolled hemorrhages can impair wound healing, increase the risk of infections and organ failure resulting in late morbidity and mortality risk and high economic cost of care [3]. Accordingly, early bleeding management is considered vital to decrease the risk of mortality during pre-hospital treatments in both military and civilian field. Therefore, there is an urgent need to develop new hemostatic materials able to prevent hemorrhages during first-aid procedures.

An ideal hemostat needs to meet some specific requirements: (a) the hemostat should be able to limit blood loss in few minutes; (b) it should be biocompatible, biodegradable, and bacteriostatic; (c) it should be stable, safe, efficient, low cost and easy to manufacture and use. A large variety of agents including drugs, biological active agents and zeolites-based hemostats are available for clinical use, but most of them present some limitations, such as adverse side effects. So, there is still a need to develop alternative hemostatic agent [4]. Recently, mesoporous silica (MS) and their composites start to gain attention in the field of hemostasis. These

materials have shown great ability in promoting blood clotting and achieving hemostasis without inducing dangerous side-effects [5].

As a part of this research project deals with the development of hemostats based on MS particles, this chapter aims at evidencing the hemostatic ability of different MS based materials and the influence of their physicochemical properties on the achievement of hemostasis.

2.1.1 The hemostatic process

Hemostasis (from Greek, haemo 'blood' and stasis 'to stop') is a physiological response of the human body, which leads to the formation of a stable clot that seals the injury in order to limit blood loss. It is a complex and dynamic process that involves different physical and chemical interactions of different components like platelets, cells, plasma coagulation factors, fibrinolytic, proteins, and cytokine mediators. Traditionally, the hemostatic process is divided into two main phases: primary hemostasis and secondary hemostasis [6,7].

Primary hemostasis consists in the formation of a primary platelet plug by means of two mechanisms, vasoconstriction and platelet plug formation.

1. **Vasoconstriction** - Vascular spasm is the first response of blood vessels after injury. Smooth muscle cells contract to limit blood flow to the injured area so resulting in the slowdown of bleeding.

2. **Platelets plug formation -** Platelets are disc shaped, anucleate cellular fragments that circulate in the blood. Normally, platelets do not adhere to blood vessels due to the presence of antithrombic molecules (nitric oxide and prostacyclin) on the vascular endothelium [8]. However, when the endothelium is interrupted, collagen fibers are exposed, and the extracellular matrix becomes thrombogenic. The presence of a thrombogenic surface stimulates platelets adhesion, activation, and aggregation. This phase of hemostasis is temporary, and it results in the formation of a weak platelet plug that will be stabilized by a fibrin network during secondary hemostasis [7].

Secondary hemostasis refers to the deposition of an insoluble fibrin network around the platelet plug to stabilize and strengthen the clot. It involves different clotting factors (table 2.1), which are activated in a cascade to generate a fibrin mesh. The generation of the fibrin network requires three fundamental steps: the activation of the clotting factors, conversion of prothrombin in thrombin and conversion of fibrinogen into fibrin. The activation of the coagulation cascade initiates through two main pathways: the extrinsic pathway (tissue factor pathway) and the intrinsic pathway (contact activation pathway). Then the two pathways converge into factor X activation, and they continue in a common pathway (figure 2.1).

Table 2.1 List of the coagulation factors (adapted from [9]).

Factor number	Name	Type of molecule	Pathway(s)
I	Fibrinogen	Plasma protein	Common; converted into fibrin
II	Prothrombin	Plasma protein	Common; converted into thrombin
III	Tissue thromboplastin or tissue factor	Lipoprotein mixture	Extrinsic
IV	Calcium ions	Inorganic ions in plasma	Entire process
V	Proaccelerin	Plasma protein	Extrinsic and intrinsic
VI	Not used	Not used	Not used
VII	Proconvertin	Plasma protein	Extrinsic
VIII	Antihemolytic factor A	Plasma protein factor	Intrinsic; deficiency results in hemophilia A
IX	Antihemolytic factor B (plasma thromboplastin component)	Plasma protein	Intrinsic; deficiency results in hemophilia B
X	Stuart–Prower factor (thrombokinase)	Protein	Extrinsic and intrinsic
XI	Antihemolytic factor C (plasma thromboplastin antecedent)	Plasma protein	Intrinsic; deficiency results in hemophilia C
XII	Hageman factor	Plasma protein	Intrinsic; initiates clotting in vitro also activates plasmin
XIII	Fibrin-stabilizing factor	Plasma protein	Stabilizes fibrin; slows fibrinolysis

The extrinsic pathway initiates when tissue factor TF, which is exposed in the sub-endothelium, binds factor VII (FVII) and converts it into its activated form (FVIIa). FVIIa and TF form a complex which transforms, in the presence of calcium ions, factor X from its inactive form to the active one Xa. In contrast, the intrinsic pathway starts when a negatively charged surface activates factor XII, upon blood vessel injury, leading then to the activation of other coagulation factors. Then, both

the intrinsic and extrinsic pathways converge into a common pathway that starts once factor X is activated. FXa with its cofactor FVa, calcium ions, tissue phospholipids and platelet phospholipids form a prothrombinase complex, a complex that is responsible for the conversion of prothrombin (factor II) to thrombin. Thrombin activations transform soluble fibrinogen into insoluble fibrin and activates factor XIII, which crosslinks with fibrin forming a stabilized clot [10].

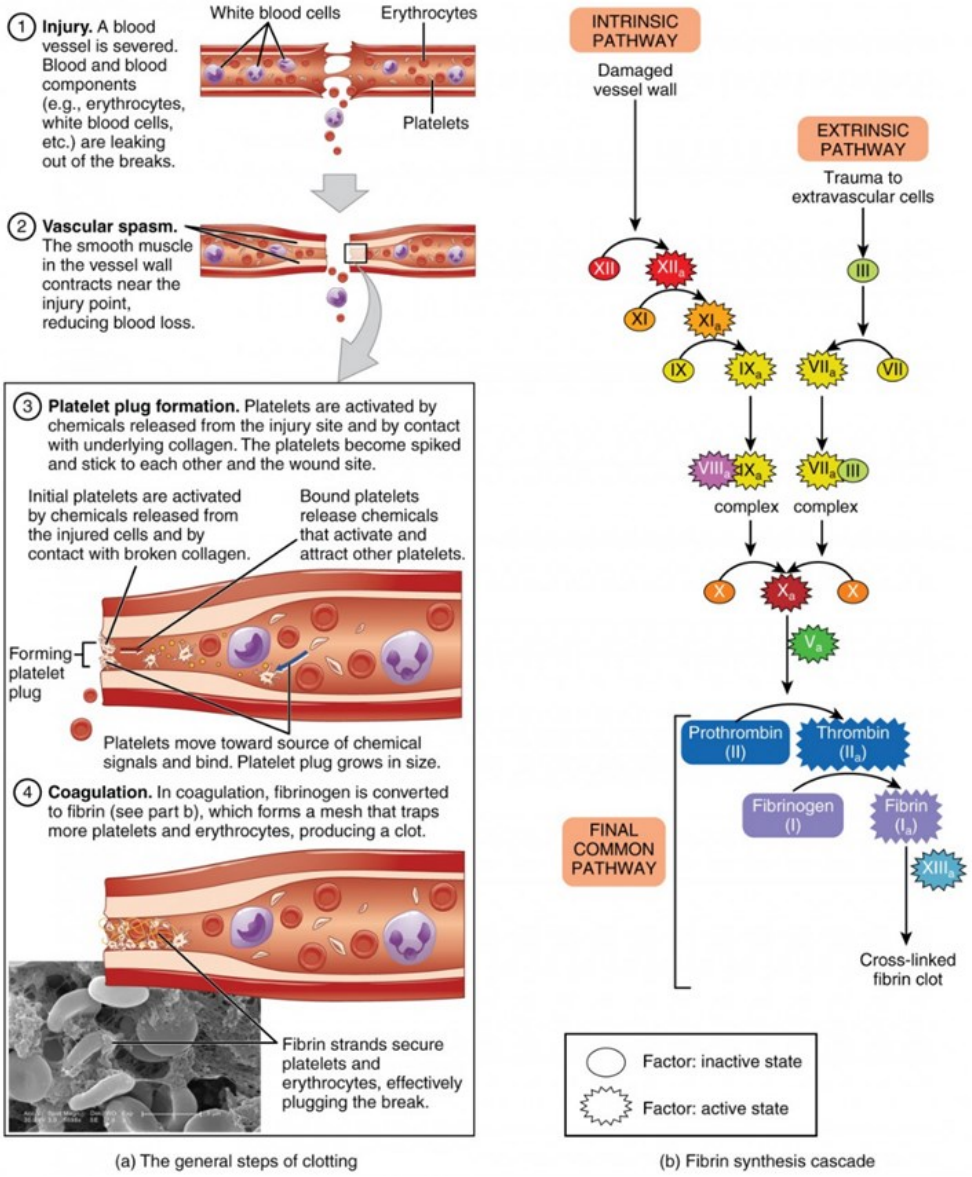

Figure 2.1 Overview of the coagulation and clotting factor signaling [9].

Recently, different studies have questioned the above-cited subdivision and have discussed different interactions between the cofactors by paying greater attention to the in vivo process. In particular, the role of FXII in the initiation of the intrinsic pathway is currently questioned as it has been recently demonstrated that FXII is mainly involved in the thrombus propagation and final stabilization together with factors XI and XIII. So, in recent years the classical view of the coagulation cascade has been replaced with a new more physiological scheme, which divided the coagulation process into four stages: the initiation, amplification, propagation, and stabilization steps (figure 2.2). Respect to the original scheme, the most significant changes are related to the existence of both the extrinsic and intrinsic pathways of the coagulation system, the role of tissue factor (TF) as well as FXI, FXII and FXIII [11].

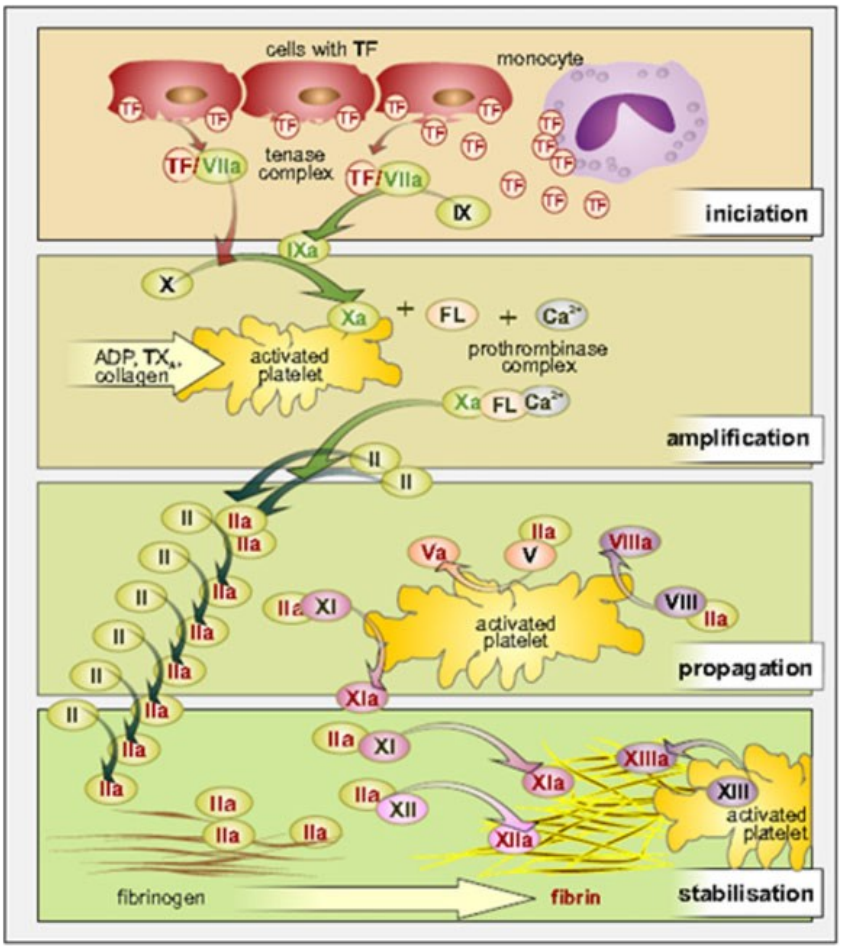

Figure 2.2 Current view on the coagulation cascade [11].

Once the vessel heals, the clot is removed by fibrinolysis**.** Fibrinolysis is an enzymatic process that gradually dissolves the fibrin mesh into fibrin degradation products, which are then cleared by other enzymes or by the liver and kidney. The process starts when plasminogen activator converts plasminogen to plasmin which cleaves fibrin and degrades the clot. This process clears the injured vessel and restores the normal blood flow [7,8].

Normally, a fine balance exists between fibrin formation and lysis to maintain and remold the hemostatic seal to prevent bleeding during tissue repair [12]. However, in some situations like major traumas, the fibrinolytic activity increases with respect to fibrin formation (hyperfibrinolysis) resulting in poor clot integrity, excessive or recurrent bleeding, and increased morbidity and mortality. To prevent excessive bleeding resulting from hyperfibrinolysis, antifibrinolytic drugs such as tranexamic acid (TXA) and ε-aminocaproic acid are administered [12,13].

2.2 Hemostatic properties of silica-based materials

Although it has been known for a long time that silica-based materials are able to accelerate blood coagulation, as it reported in the study of Margolis (1961) [14], only in the last decade their application as a hemostatic material has started to gain attention (figure 2.3). Similarly to zeolites and clay-based hemostatic materials, MS-based materials are able to promote blood clotting and hemostasis without causing those adverse side effects that can be observed for inorganic hemostats (thermal tissue injuries, thrombotic complications and poor biodegradability). The hemostatic properties of MS-based materials are mainly attributed to their high porosity and high specific surface area, which enhance their adsorption capacity so leading to higher concentration of the blood components at the hemorrhagic site (factor concentration ability). Moreover, the presence of high concentration of polar silanol groups and negative charges on the surface of MS materials is beneficial for blood coagulation, since it is considered important to stimulate the activation of factor XII and other clotting proteins (procoagulant ability).

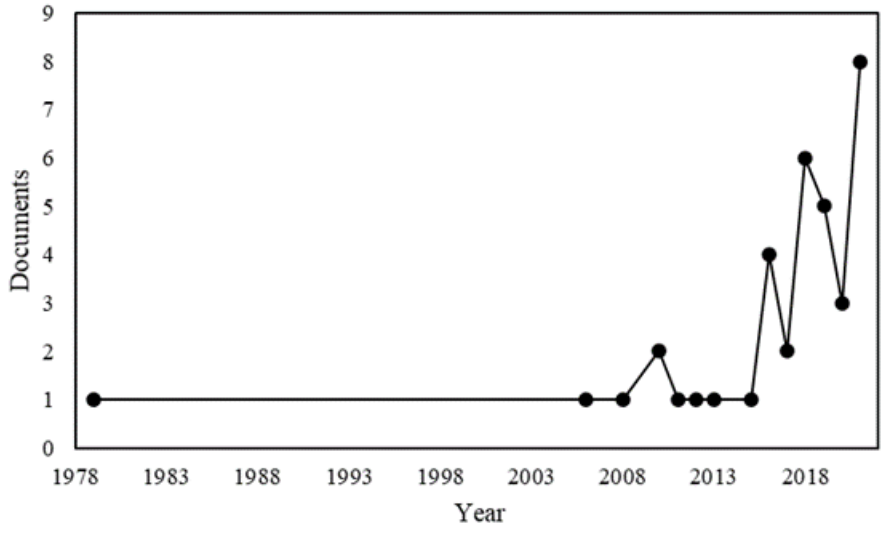

Figure 2.3 Number of documents related to silica as hemostatic material, in the range 1978 – 2022 [15].

In the literature, several studies have investigated the hemostatic ability of MS-based materials. In particular, the effect of specific surface area and pore dimension have been studied as they are considered important factors in improving the adsorption capacity of the materials. Also, the inclusion of calcium ions has been evaluated since it contributes to the hemostatic efficiency of the material. Calcium ions, or clotting factor IV, play an important role in the regulation of the clotting cascade and in the maintenance of hemostasis. In addition to their role in platelets activation and aggregation, calcium ions are involved in the activation of both the intrinsic and extrinsic pathways of the coagulation cascade by acting as a cofactor for other coagulation factors [5,16].

The effect of mesocellular foams (MCF) with different cell-window sizes (5.9 to 33.1 nm) on blood clot initiation was studied by *Baker et al.* [17] using thrombelastography (TEG) measurements in frozen pooled human plasma. Results revealed that the time required to initiate clot formation decreased from 9.8 to 6 min as the cell-window size increased from 6 to 33 nm; in particular, when the cell-window size was greater than 20 nm, the time to clot formation was considerably shortened (figure 2.4). The positive effect of a higher MCF window size on the reduction of the blood clot initiation time was attributed to the fact that larger cell-window diameters may increase the protein-accessible surface area.

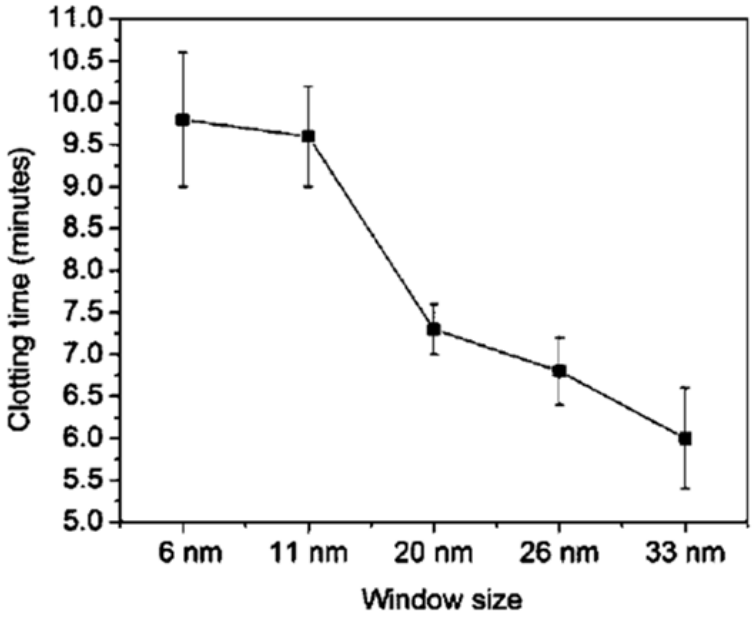

Figure 2.4 Effects of the MCF window size on the time to clot formation [17].

Similarly, *Li et al.* [18] investigated the hemostatic potential as well as the cytotoxicity of MCF with a cell-window diameter of 26 nm (MCF-26) and compared the results with those obtained with layered clays (Kaolin, bentonite, and montmorillonite). They found that MCF-26 was effective in promoting blood clotting. Moreover, the study evidenced that MCF-26 was less cytotoxic to human endothelial and skin cells with respect to layered clays. The results of their study were in accordance with the outcomes reported by *Baker et al.* [17]. This indicates that MCF with large cell-window diameters (i.e., greater than 20 nm) can be considered promising materials as hemostatic agents.

Chen et al. [1] investigated the effect of pore and particle dimensions on the hemostatic efficiency of mesoporous silica nanoparticles (MSN). In their study, spherical mesoporous silica nanoparticles with different pore and particle diameters were synthesized using a vesicle-organic template method. Results of the clotting blood time (CBT) tests (figure 2.5a) showed that the variation of the pore size from 5 to 15 nm significantly influenced the blood clot rate by shortening the CBT time when compared to control. However, the variation of the particle size from 60 to 220 nm did not seem to affect the coagulation time. The TEG results indicated that MSN with pore size above 10 nm were able to reduce the clot formation time and to increase the clot strength. The extent of adsorption of factor XII was also

evaluated by the authors. The results of the test demonstrated that the accessibility and diffusion of factor XII depended on pore size; MSN with pore size larger than 10 nm showed less FXII surplus in the blood with respect to other samples (figure 2.5b). The authors concluded that the presence of large pores allowed FXII and other contact activation proteins to diffuse into them, adhere, activate, and diffuse out, which resulted in the acceleration of blood coagulation. The hemostatic efficiency was also evaluated in rabbit femoral artery injuries and the results indicated that MSN with pore size of 15 nm could achieve rapid hemostasis and decrease the mortality rate (figure 2.5c). To further enhance the hemostatic ability of MSN, *Chen et al.* [1] developed a hemostatic sponge based on N-alkylated chitosan and MSN with large pores (MSN-GACS). The obtained material exhibited improved hemostasis when compared to MSN and chitosan [19].

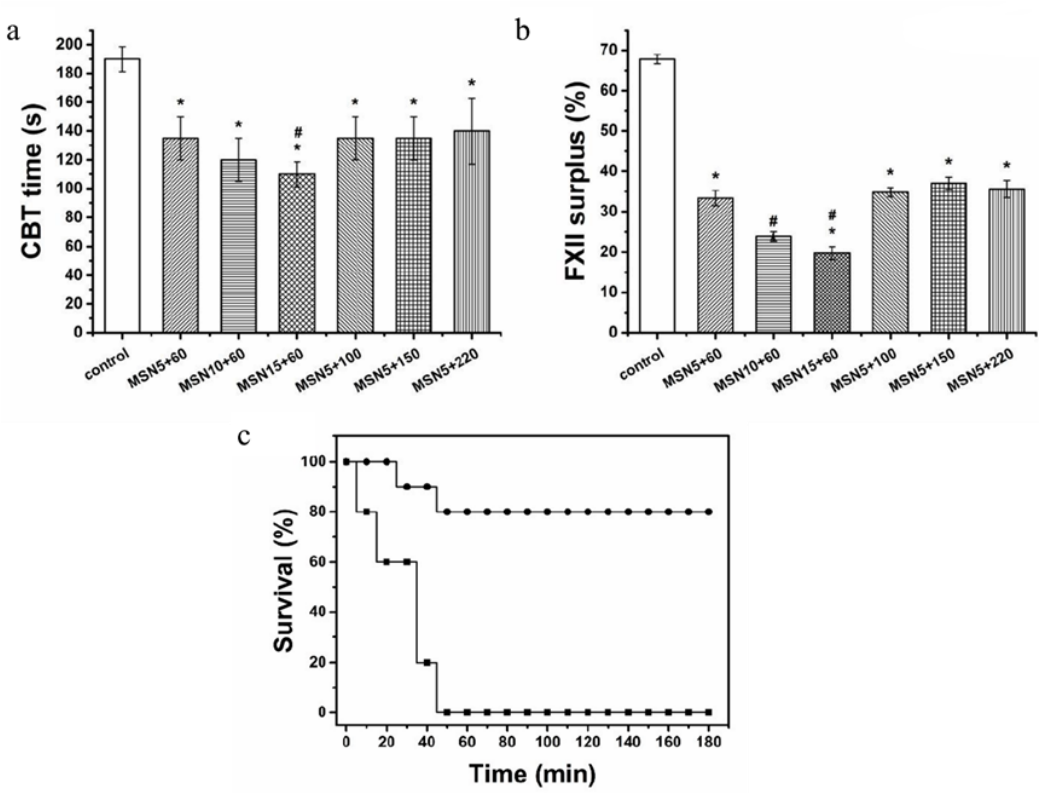

Figure 2.5 (a) CBT time for MSN. (b) FXII surplus in poor platelet plasma after exposed to MSN. (c) Survival rate of animals exposed to a femoral artery injury. Animals were treated with MSN (●) and standard gauze (■) [1].

The effect of specific surface area and the inclusion of calcium ions (Ca^{2+}) on the hemostatic efficiency of mesoporous silica xerogels was investigated by *Wu et al.* [20]. The ordered mesoporous silica calcium-doped xerogel (m-SXC) was prepared by sol-gel process. The hemostatic activity of the synthesized materials was evaluated by measuring the prothrombin time (PT) and activated partial thromboplastin time (APTT). The results indicated that PT and APTT were shortened by the presence of m-SXC0 (mesoporous silica xerogel without Ca^{2+}) xerogel with respect to non-mesoporous silica xerogel and control (figure 2.6a). The blood clotting ability of the mesoporous silica xerogel was ascribed to its high surface area, which improved the water absorption capability of the material so resulting in higher concentration of the blood components and reduced clotting time. In addition, the APTT and PT significantly decreased with the increase of the m-SXC5 amount (figure 2.6b) Moreover, the inclusion of Ca^{2+} also showed a significant decrease in APTT and PT (figure 2.6c), revealing that calcium ions had a remarkable effect on clotting time. The authors of the study concluded that both high a surface area and the inclusion of Ca^{2+} could improve the hemostatic performances of silica-based materials.

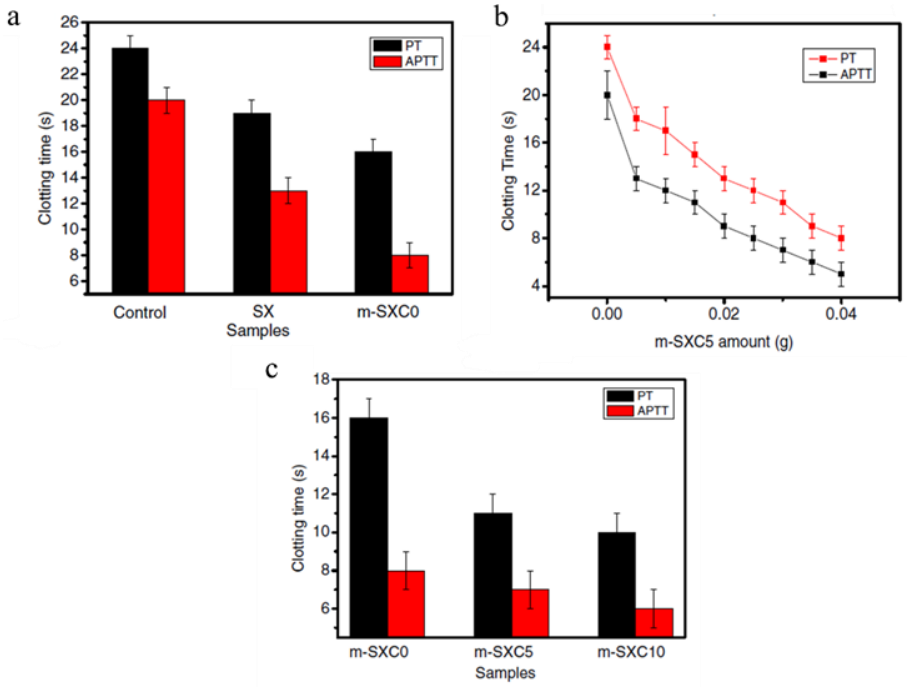

Figure 2.6 Clotting time versus materials; (a) effect of materials 'structure on APTT and PT, (b) effect of silica xerogels' amount on APTT and PT, and (c) effect of Ca content on APTT and PT [20].

The pore size and the extent of the surface area of MS are not the only parameters that may affect the hemostatic efficiency. The role of the form of mesoporous silica-based materials was also investigated in the literature. It was in fact found that when mesoporous silica is in powder form, it may present some drawbacks [21]:

- Due to their low density and poor flowability, powders cannot be immersed properly in the blood, and they can be washed away by blood flow.
- The dust generated from these powders could be harmful for the operators and the environment.
- If debridement has to be performed, this may be hindered by the presence of thick calluses, which are formed when powder is mixed with blood and make this procedure painful for the patient.
- The voids between the particles could be modified during water absorption leading to a decrease in the hemostatic efficacy because of the decreasing capillary motion.

To overcome the above-mentioned limitations an alternative approach could be the production/preparation of granules. *Hong et al.* [21] studied the flowability, water absorption and the *in vitro* as well as the *in vivo* hemostatic performances of different porous silica spherical-like granules with sizes in the 0.40 - 1.10 mm (G_{40} and G_{44}) range. The granules (G_{40} and G_{44}) were prepared starting from mesoporous silica particles (MSP), polyurethane, sodium pyrophosphate and clay via dry mixing and wet granulation. Results showed that granulation enhanced the infiltration ability of the mesoporous material with fluids, stabilized their capillary structure, increased the density of the particles, and eliminated the formation of dust. Moreover, water absorption ability was better in the case of granules (figure 2.7a), which is an important aspect in the initial phase of the stop-bleeding process. The *in vitro* hemostatic efficacy of granules was higher than that of MS particles; the clotting time decreased from 150 s for mesoporous silica particles to 30 s for granules (figure 2.7b). The *in vivo* hemostatic performance of granules indicated that granules were able to accelerate hemostasis. The high efficacy was ascribed to the ability of granules to absorb a high quantity of water at the early stage so resulting in a rapid concentration of blood components and a decrease in the bleeding time.

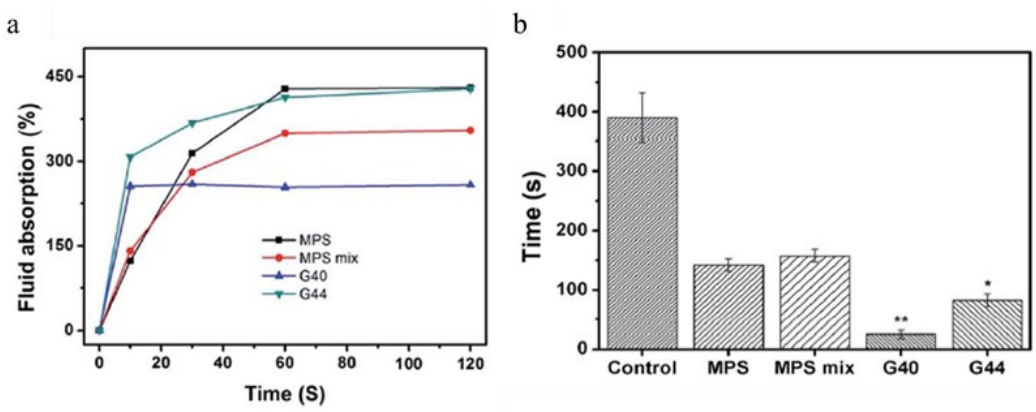

Figure 2.7 (a) Water absorbability and (b) Coagulation time of samples [21].

As mentioned earlier, in addition to promoting blood coagulation, an ideal hemostat should also prevent wound infection. One possible approach could be the incorporation of bioactive molecules or therapeutic elements, which confer antibacterial properties to the material. *Dai et al.* [22] investigated the effect of the inclusion of calcium and silver ions on the hemostatic and antibacterial performances of mesoporous silica sphere (MSS). To produce the silver-calcium doped mesoporous silica spheres (AgCaMSS), a calcium doped MSS (CaMSS) was first synthesized by a one-step based catalyzed self-assembly process using cetyltrimethylammonium bromide (CTAB) as a template, tetraethyl orthosilicate (TEOS) as the silica precursor and $Ca(NO_3)_2.4H_2O$ as the calcium precursor; subsequently the material was loaded with silver ions via an ion exchange method. The hemostatic activity was investigated both *in vitro* and *in vivo* and the antibacterial ability was investigated against *Escherichia coli* (gram negative bacteria) and *Staphylococcus aureus* (gram positive bacteria). The results of the *in vitro* hemostatic tests indicated that AgCaMSS could promote blood clotting, induce platelets adhesion, and activate the intrinsic pathway of the coagulation cascade. The *in vivo* study showed that AgCaMSS was able to control hemorrhage in the femoral artery and liver injuries in rabbits; the time required for complete hemostasis in severe liver injuries was shortened from 161.2 s in the control group to 9.2 s in the animals treated with AgCaMSS. The antibacterial experiments revealed that AgCaMSS had better antibacterial activity against *Escherichia coli* and *Staphylococcus aureus* with respect to CaMSS.

In another approach, *Wang et al.* [23] studied the possibility of using tannic acid (TA) - loaded ordered mesoporous silica spheres (MS) as a hemostatic and antibacterial material. The MS were synthesized by a one-step basic catalyzed self-assembly process using CTAB as a structure directing agent and TEOS as the silica precursor; TA was loaded via covalent conjugation (15T-g-MS) and electrostatic adsorption (5TMS and 15TMS). The results suggested that the TA-absorbed MS (i.e., 5TMS and 15TMS, where 5 and 15 indicate the percentage of loaded TA in each sample) were able to achieve hemorrhage control by promoting protein adherence and by facilitating the contact activation pathway of the coagulation cascade without inducing hemolysis. Moreover, they could also enhance the antibacterial activity. In particular, the 15TMS samples demonstrated the best hemostasis performance both *in vitro* and *in vivo*. They shortened the bleeding time (figure 2.8a), which leaded to lower blood loss (figure 2.8b) and showed superior antibacterial activity against *Staphylococcus aureus* and *Staphylococcus epidermidis* (figure 2.8c). However, TA-g-MS showed inferior hemostatic and antibacterial ability when compared to TA-absorbed MS. The authors attributed these phenomena to the fact that the chemical grafting of TA, whose molecules replace the silanol groups present on the surface, leads to a reduction in the surface area of MS and this results in poor hemorrhage control.

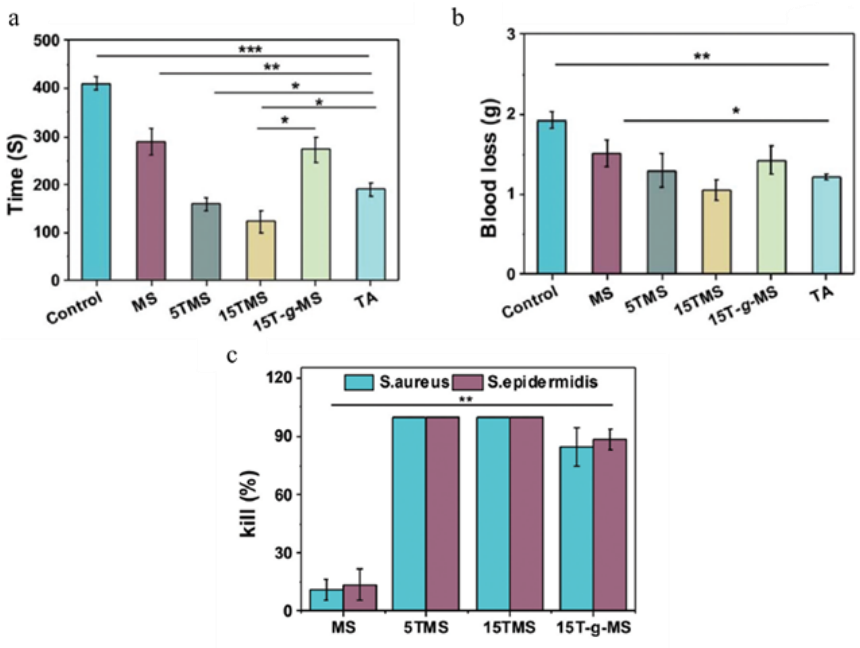

Figure 2.8 (a) Hemostasis time and (b) Blood loss in the rat amputation model. (c) Antibacterial activity of TA-loaded MS [23].

In a similar work, *Li et al.* [24] developed a polyvinyl pyrrolidone nanofiber where curcumin-loaded mesoporous silica was incorporated (CCM-MSNs@PVP) for hemostasis and antibacterial treatment. The inorganic-organic hybrid material was prepared by incorporating the curcumin-loaded mesoporous silica nanoparticles into polyvinylpyrrolidone nanofibers using electrospinning. The hemostatic efficiency and antibacterial activity of the hybrid nanofibers were investigated by both *in vitro* and *in vivo* experiments. Results of the whole blood absorption test showed that the CCM-MSNs@PVP possessed higher liquid absorption ability than the standard hemostatic gauze, and the outcomes of the PT and APPT tests revealed that the material could activate both the extrinsic and intrinsic coagulation pathways. *In vivo* hemostasis tests showed that the CMM-MSNs@PVP was able to achieve hemorrhage control in liver injuries. Moreover, CMM-MSNs@PVP showed an improved antibacterial effect against methicillin-resistant *Staphylococcus aureus*.

2.3 Hemolytic activity of silica-based materials

Hemolysis is mainly defined as the rupture of red blood cells (RBCs) with the consequent release of hemoglobulin (hb) and other intracellular contents into plasma [25]. In 2008, the American Society for Testing and Materials (ASTM) proposed a standard method to evaluate the hemolytic activity of materials. This standard test aims at evaluating the percentage of hemoglobin (Hb) released into the plasma when a material is incubated with RBCs [26]. Generally, when hemolysis occurs, different degrees of red tinge in serum or plasma can be observed once the blood specimen has been centrifuged. The extent and intensity of this interference depends on the degree of hemolysis [27] (figure. 2.9.). Therefore, it is important to check the hemocompatibility of any material before its use. As MS-based material are good candidates in biomedical applications, it is important to understand if they hemocompatible and the to identify those parameters that are responsible for interfering the hemocompatibility. Different parameters such as particles shape, size and concentration might influence the hemocompatibility or toxicity of MS [26]. Therefore, various studies were conducted to investigate the effect of these parameters on the hemocompatibility of MS particles.

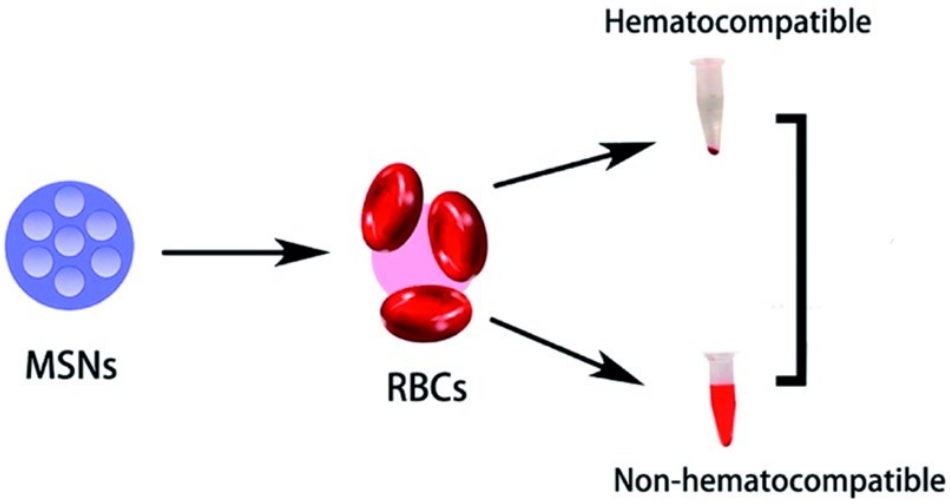

Figure 2.9 Representation of mesoporous silica nanoparticles hemocompatibility with RBCs [26].

Slowing et al. [28] investigated the hemolytic behavior of mesoporous silica nanoparticles at a series of concentrations, up to 100 µg/ml, with rabbit RBCs, and compared it with the hemolytic properties of other nonporous silica materials. The results of the study indicated that amorphous silica showed high hemolytic activity at a concentration of 100 µg/ml. On the other hand, no hemolysis of RBCs was observed in the samples of mesoporous silica nanoparticles at concentrations ranging from 20 to 100 µg/ml (figure 2.10).

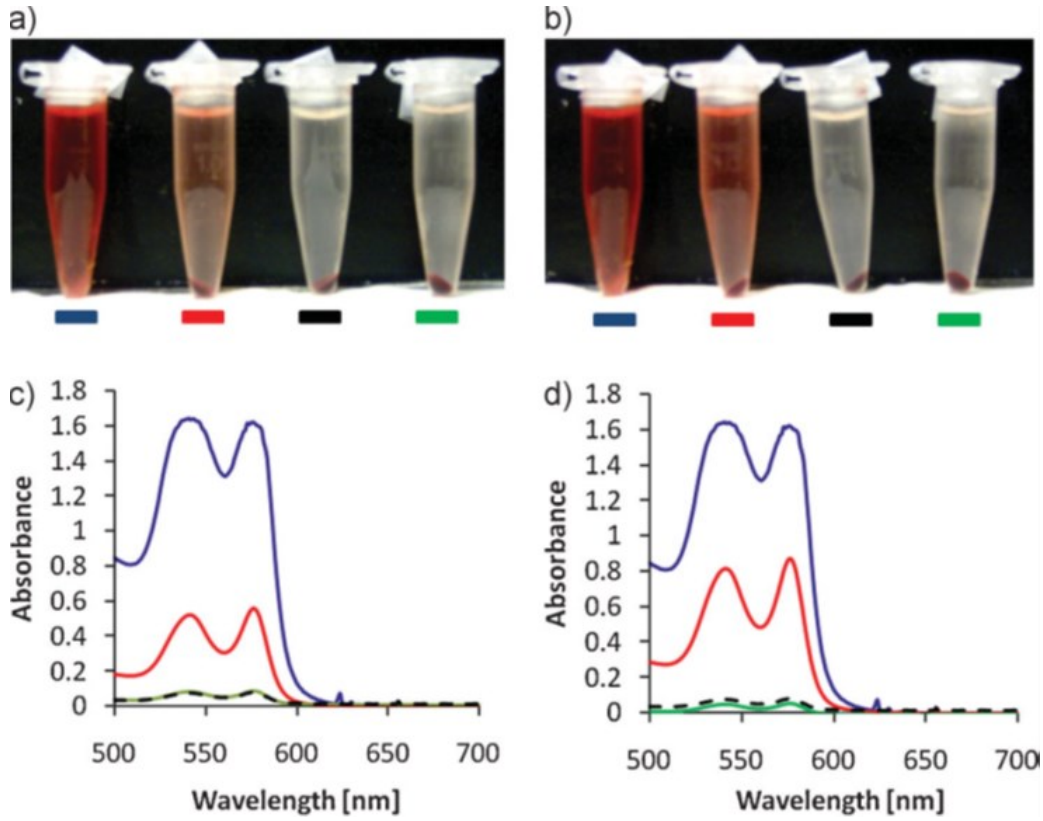

Figure 2.10 Hemolysis assay for amorphous silica (red lines) and Mesoporous silica nanoparticles (green lines), using water as a positive control (blue lines) and PBS as a negative control (dashed black lines). The materials were suspended at 60 (a, c) and 100µg/mL (b, d) [28].

In a similar work, *Lin et al.* [29] evaluated the toxicity of nonporous and porous silica nanoparticles with varied sizes (ranging from 25 to 250 nm) using a simple hemolysis assay. The results indicated that both nonporous and porous nanoparticles showed dose- and size-dependent hemolytic activity on RBCs. Generally, smaller particles showed higher toxicity than larger particles. The only exception to this trend was that of the smallest mesoporous silica nanoparticles (particles size 25 nm), which demonstrated a lower hemolytic activity than expected may be due to their lowered amount of cell-contactable silanol group, owing to the presence of large pores and high pore volume. Moreover, mesoporous silica nanoparticles exhibited a reduced hemolytic activity with respect to their nonporous counterparts of similar size, may be due to the voids on the surface of mesoporous nanoparticles (figure 2.11).

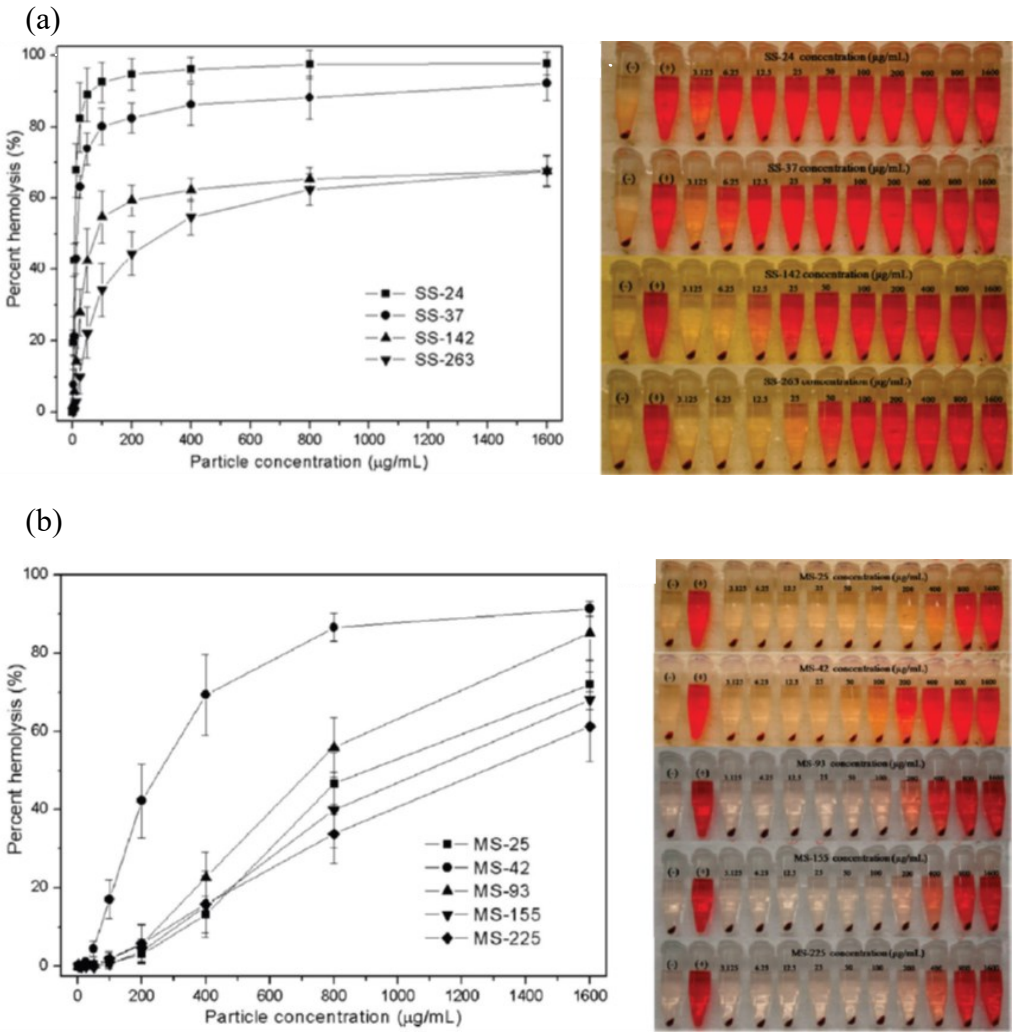

Figure 2.11 (a) Percentage of hemolysis of RBCs and photographs of hemolysis of RBCs incubated with four sizes of nonporous silica nanoparticles (SS), and (b) Percentage of hemolysis of RBCs and photographs of hemolysis of RBCs incubated with four sizes of mesoporous silica nanoparticles (MS) [29].

Zhao et al. [30] investigated the interaction between mesoporous silica nanoparticles (MCM-41 and SBA-15) and RBCs membranes. In the study, the authors compared the hemocompatibility of two of the most familiar types of mesoporous silica nanoparticles (MCM-41 and SBA- 15). The results of the study showed that small MCM-41 (particle size of about 100 nm) did not cause any disturbance or membrane deformation of RBCs. In contrast, large SBA-15 (particle size of about 600 nm) induced a significant local membrane deformation, which consequently caused hemolysis (figure 2.12).

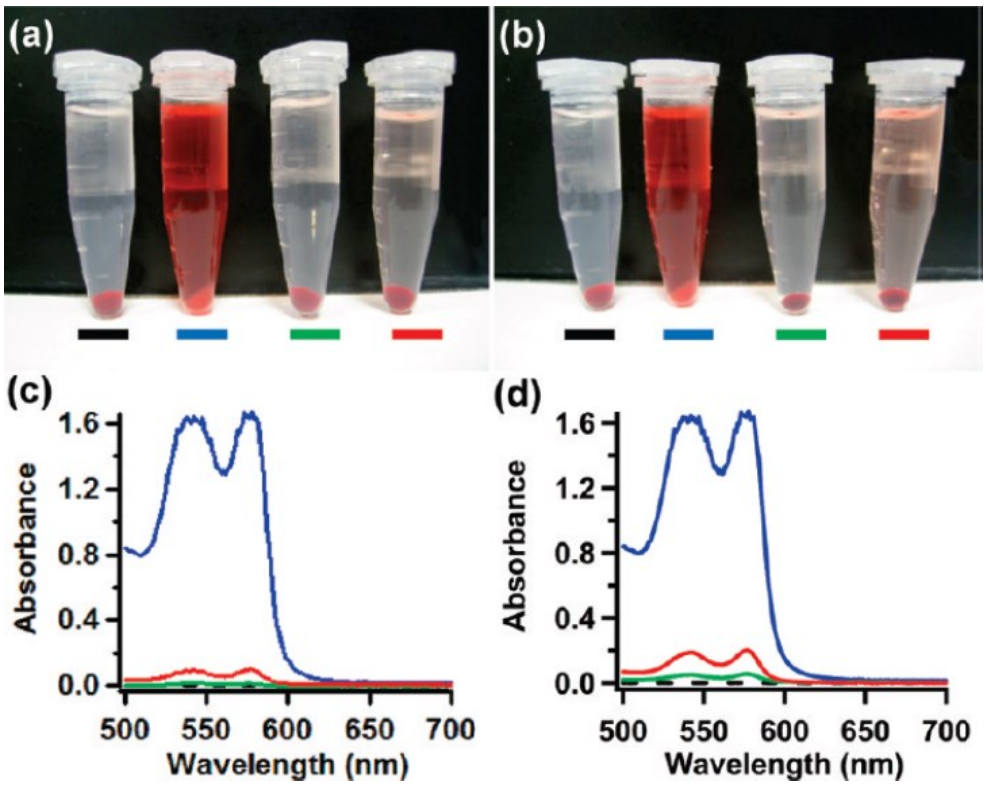

Figure 2.12 Hemolysis assay for MCM-41 (green lines) and SBA-15 (red lines), using water as a positive control (blue lines) and PBS as a negative control (dashed black lines). The materials were suspended at 50 (a,c) and 100 µg /ml (b,d) [30].

The impacts of geometry, porosity, and surface charge on the hemolytic activity of silica were investigated by *Yu et al.* [31]. In their work, the authors selected nonporous Stöber silica nanospheres (115 nm diameter), mesoporous silica nanospheres (Meso S, 120 nm diameter, aspect ratio 1), mesoporous silica nanorods with aspect ratio of 2, 4, and 8 (AR2 width by length 80 × 200 nm, AR4 150 × 600 nm and AR8 130 × 1000 nm), and their cationic counterparts (SA, MA, 2A, 4A 8A), and evaluated their impacts on and human RBCs by a hemolysis assay. The outcomes of the study showed that the hemolytic activity was concentration-, porosity-, and geometry-dependent for bare SiO_2 (figure 2.13). No hemolytic toxicity was observed for mesoporous silica samples below 100 µg/ml. By increasing the concentration, the impact of the geometry became important. Spherical or low aspect ratio mesoporous silica showed a higher hemolytic activity than mesoporous silica with high aspect ratio. This behavior could be ascribed to the fact that spheres had a large external surface area and small curvature, which might render the hemolysis process thermodynamically more favorable. However,

from the comparison of the hemolytic activity of Stöber and mesoporous silica spheres (which had similar curvature), it emerged that mesoporous silica spheres did not lead to a higher hemolytic rate than Stöber ones until the mass concentration exceeded *ca*. 190 µg/ml, suggesting that there could be a threshold in the density of silanol groups above which this could cause membrane damage. On the other hand, the hemolytic activity of amine-modified SiO_2 was surface charge- and concentration-dependent (figure 2.14). By increasing the concentration, a rapid onset of hemolysis for all types of nanoparticles was observed. Stöber silica exhibited the lowest hemolytic activity may be due to lowest surface charge (zeta potential 17.0 ± 0.7 mV), while amine-modified mesoporous silica (zeta potential in the range 32.4 ± 0.9 - 40.3 ± 1.0 mV) caused similar rates of hemolysis, which reveals that increasing the surface charge beyond a certain threshold (>30 mV) might lead to elevated hemolysis by amine-modified mesoporous silica.

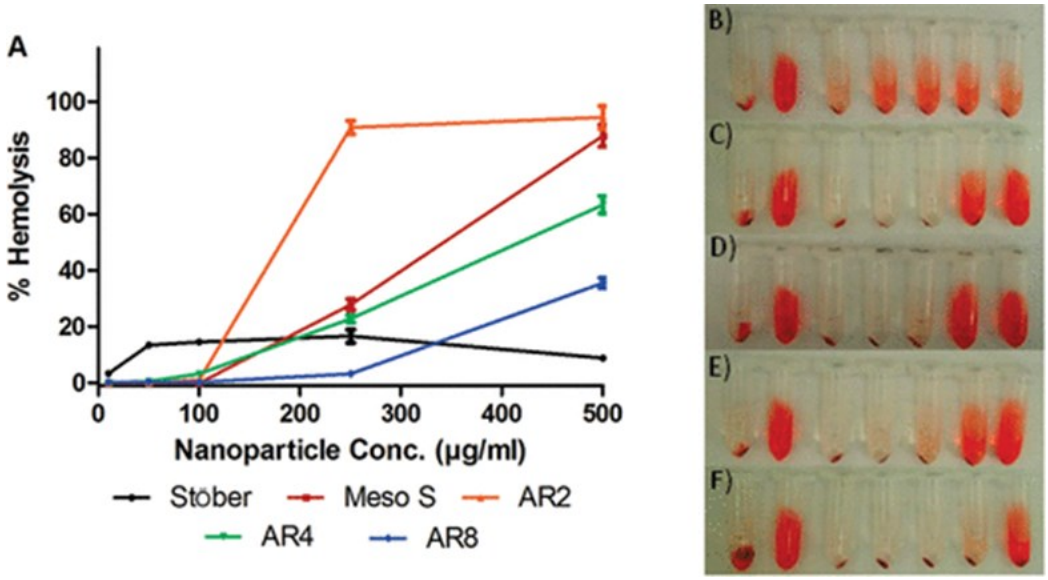

Figure 2.13 Hemolysis assay on bare SiO_2. (A) Relative rate of hemolysis in human RBCs upon incubation with nanoparticle suspension at incremental concentrations. Photographs of hemolysis of RBCs incubated with (B) Stöber suspension, (C) Meso S suspension, (D) AR2 suspension, (E) AR4 suspension, and (F) AR8 suspension. The tubes are lined up (from left to right) as negative control (PBS), positive control (water), 10 µg/mL suspension, 50 µg/mL suspension, 100 µg/mL suspension, 250 µg/mL suspension, and 500 µg/mL suspension [31].

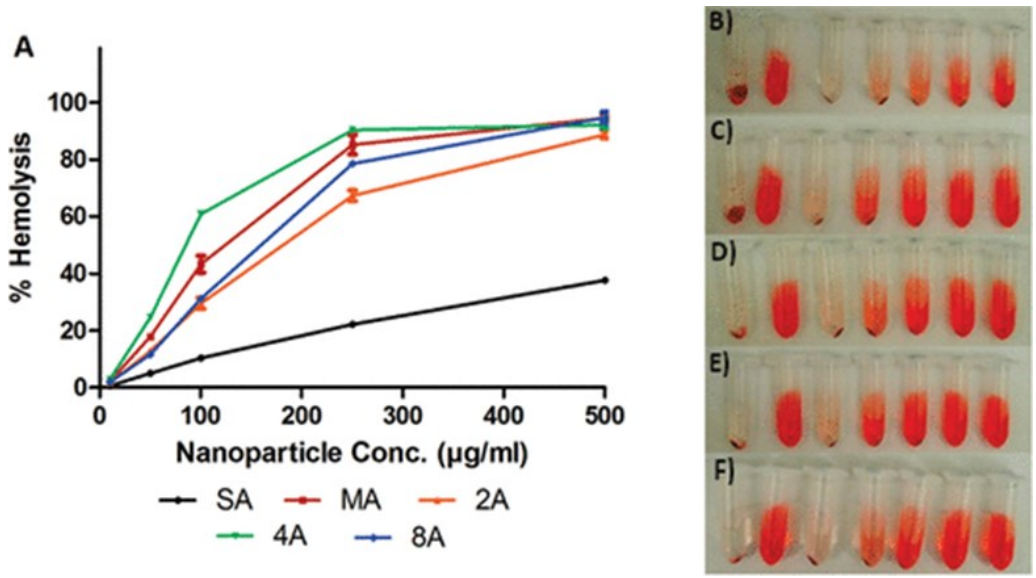

Figure 2.14 Hemolysis assay on amine modified SiO_2. (A) Relative rate of hemolysis in human RBCs upon incubation with amine-modified nanoparticle suspension at incremental concentrations. Photographs of hemolysis of RBCs incubated with (B) SA suspension, (C) MA suspension, (D) 2A suspension, (E) 4A suspension, and (F) 8A suspension. The tubes are lined up (from left to right) as negative control (PBS), positive control (water), 10 µg/mL suspension, 50 µg/mL suspension, 100 µg/mL suspension, 250 µg/mL suspension, and 500 µg/mL suspension [31] .

2.4 Conclusions

The main objective of this chapter was to provide insights into the use of mesoporous silica-based materials as hemostatic materials. After describing the hemostasis process, some of the most recent research studies concerning their *in vitro* and *in vivo* hemostatic activity as well as their hemolytic ability have been reviewed.

It has been found that mesoporous silica-based materials possess great potential for hemostatic applications since they present various properties, which are important in achieving hemostasis. These materials have high surface area, large volume and large pores, which provides them a higher water adsorption capacity with respect to other inorganic materials (zeolites and clays). This is an important feature for the acceleration of blood clot formation. In addition, mesoporous silica can be doped with small quantities of trace elements (for example, calcium and

silver ions), which can potentiate their hemostatic ability and provide them an antibacterial effect.

The effect of particle morphologies and porosity on the hemolytic activity of MS is also emphasized in this chapter. From the analysis of the literature, it has emerged that concentrations up to 100 μg/ml of various kinds of MS particles showed good hemocompatibility. These remarkable features of MS-based materials make them interesting for developing new hemostats that could be used in bleeding control.

2.5 References

1. Chen, Z. *et al.* Blood clot initiation by mesoporous silica nanoparticles: Dependence on pore size or particle size? *J. Mater. Chem. B* **4**, 7146–7154 (2016).

2. Donley ER, Loyd JW. Hemorrhage Control. [Updated 2021 Jul 23]. In: StatPearls [Internet]. Treasure Island (FL): StatPearls Publishing; 2021 Jan. Available from: https://www.ncbi.nlm.nih.gov/books/NBK535393/.

3. Schreiber, M. A. & Neveleff, D. J. Achieving hemostasis with topical hemostats: Making clinically and economically appropriate decisions in the surgical and trauma settings. *AORN J.* **94**, S1–S20 (2011).

4. Pourshahrestani, S., Zeimaran, E., Djordjevic, I., Kadri, N. A. & Towler, M. R. Inorganic hemostats: The state-of-the-art and recent advances. *Mater. Sci. Eng. C* **58**, 1255–1268 (2016).

5. Pourshahrestani, S., Kadri, N. A., Zeimaran, E. & Towler, M. R. Well-ordered mesoporous silica and bioactive glasses: Promise for improved hemostasis. *Biomater. Sci.* **7**, 31–50 (2019).

6. Hangge, P. *et al.* Hemostasis and nanotechnology. *Cardiovasc. Diagn. Ther.* **7**, S267–S275 (2017).

7. Periayah, M. H., Halim, A. S. & Saad, A. Z. M. Mechanism action of platelets and crucial blood coagulation pathways in Hemostasis. *Int. J. Hematol. Stem Cell Res.* **11**, 319–327 (2017).

8. Palta, S., Saroa, R. & Palta, A. Overview of the coagulation system. *Indian J. Anaesth.* **58**, 515–523 (2014).

9. Module 2: The Cardiovascular System: Blood. https://courses.lumenlearning.com/ap2/chapter/hemostasis/.

10. Chaudhry R, Usama SM, Babiker HM. Physiology, Coagulation Pathways. 2021 Sep 1. In: StatPearls [Internet]. Treasure Island (FL): StatPearls Publishing; 2021 Jan. PMID: 29489185.

11. Vojacek, J. F. Should We Replace the Terms Intrinsic and Extrinsic

Coagulation Pathways With Tissue Factor Pathway? *Clin. Appl. Thromb.* **23**, 922–927 (2017).

12. McCormack, P. L. Tranexamic Acid: A review of its use in the treatment of hyperfibrinolysis. *Drugs* **72**, 585–617 (2012).

13. Gall, L. S., Brohi, K. & Davenport, R. A. Diagnosis and Treatment of Hyperfibrinolysis in Trauma (A European Perspective). *Semin. Thromb. Hemost.* **43**, 224–234 (2017).

14. Margolis, J. & Alexandra, R. The effect of colloidal silica on blood coagulation. *Aust J Exp Biol Med Sci.* **39,** 249–258 (1961).

15. Elsevier. Scopus.

16. Singh, S. *et al.* Structure functional insights into calcium binding during the activation of coagulation factor XIII A. *Sci. Rep.* **9**, 11324 (2019).

17. Baker, S. E. *et al.* Blood clot initiation by mesocellular foams: Dependence on nanopore size and enzyme immobilization. *Langmuir* **24**, 14254–14260 (2008).

18. Li, Y. *et al.* Cytotoxicity and potency of mesocellular foam-26 in comparison to layered clays used as hemostatic agents. *Toxicol. Res. (Camb).* **2**, 136–144 (2013).

19. Chen, Z. *et al.* A rapid hemostatic sponge based on large, mesoporous silica nanoparticles and: N -alkylated chitosan. *Nanoscale* **10**, 20234–20245 (2018).

20. Wu, X. *et al.* Chemical characteristics and hemostatic performances of ordered mesoporous calcium-doped silica xerogels. *Biomed. Mater.* **5**, 035006 (2010).

21. Hong, H. *et al.* Novel porous silica granules for instant hemostasis. *RSC Adv.* **6**, 78930–78935 (2016).

22. Dai, C. *et al.* Degradable, antibacterial silver exchanged mesoporous silica spheres for hemorrhage control. *Biomaterials* **30**, 5364–5375 (2009).

23. Wang, C. *et al.* Tannic acid-loaded mesoporous silica for rapid hemostasis and antibacterial activity. *Biomater. Sci.* **6**, 3318–3331 (2018).

24. Li, D. *et al.* Fabrication of curcumin-loaded mesoporous silica incorporated polyvinyl pyrrolidone nanofibers for rapid hemostasis and antibacterial treatment. *RSC Adv.* **7**, 7973–7982 (2017).

25. Munnix, I. C. A., Schellart, M. & Kleinveld, H. A. Factors reducing hemolysis rates at the emergency department. **35**, 196–197 (2010).

26. Mukhopadhyay, S. *et al.* Synthesis and compatibility evaluation of versatile mesoporous silica nanoparticles with red blood cells: an overview. *RSC Adv.* **9**, 35566–35578 (2019).

27. Deneyimi, A. Experience in Reducing Hemolysis in the Emergency Laboratory Acil Laboratuvarda Hemoliz Oranlar ı n ı. **19**, 71–76 (2021).

28. Slowing, I. I., Wu, C. W., Vivero-Escoto, J. L. & Lin, V. S. Y. Mesoporous silica nanoparticles for reducing hemolytic activity towards mammalian red blood cells. *Small* **5**, 57–62 (2009).

29. Lin, Y. S. & Haynes, C. L. Impacts of mesoporous silica nanoparticle size, pore ordering, and pore integrity on hemolytic activity. *J. Am. Chem. Soc.* **132**, 4834–4842 (2010).

30. Zhao, Y. *et al.* Interaction of mesoporous silica nanoparticles with human red blood cell membranes: Size and surface effects. *ACS Nano* **5**, 1366–1375 (2011).

31. Yu, T., Malugin, A. & Ghandehari, H. Impact of Silica Nanoparticle Design on Cellular Toxicity and Hemolytic Activity. *ACS Nano* **5**, 5717–5728 (2011).

Chapter 3
The influence of the physicochemical properties of mesoporous silica particles on hemostasis

Part of the information reported in this chapter has been previously published in *Mohamed et al*. **2021**, *Journal of Molecular Sciences,* 22, 13403 [1].

3.1 Introduction

Uncontrolled hemorrhage in the surgical and trauma settings could result in a significant clinical and economic impact. Controlling this phenomenon is important to assure the achievement of surgical success and positive patient outcomes. Indeed, a poor management of bleeding can extend the length of the surgical procedure, impair wound healing and increase the risk of infection. Moreover, it is associated with increased mortality rates and high costs of care. Therefore, achieving hemostasis becomes a crucial focus for those clinicians working in surgical and trauma settings [2]. Various products, which include both organic and inorganic materials, have been applied to control bleeding. Mineral zeolites and kaolin have already been used as hemostatic agents in clinical settings [3]. However, these materials suffered from some side effects such as poor biodegradability and a high exothermic phenomena, which might result in thermal injuries and inflammation [4].

At variance with zeolites, MS presents a silica matrix with higher porosity, larger surface area and a negatively charged surface. Moreover, MS based materials have shown great potential in promoting the coagulation cascade and achieving desirable hemostasis. Furthermore, they are able to overcome those dangerous side-effects that are typical of inorganic hemostats [4,5]. Taking into account all these aspects, it can be concluded that MS based materials might be considered as promising hemostatic materials.

As stated in chapter 2, there are several variables including particle morphology, particle size, surface properties and pore size that may possibly affect the hemostatic performance of mesoporous silica-based materials. Among these, the pore size probably represents one of the most important parameters. Various studies suggested that particles with large pore size (> 10 nm) present better hemostatic ability than those with small pore size [6,7].

Based on the above consideration, the aim of this research work was the development of a topical hemostat based mesoporous silica spheres with large pores (> 10 nm) to be used in the management of massive bleeding in emergency situations. To this purpose, mesoporous silica microspheres (MSM) with large pores were synthesized and characterized by means of different techniques: nitrogen sorption analysis, field emission scanning electron microscopy (FESEM) and Fourier transform infrared spectroscopy (FT-IR). The hemostatic performance of the system was evaluated by means of a clotting blood time (CBT) test; a hemolysis assay was carried out to investigate the hemocompatibility of the material. To assess the effect of pore size on hemostasis, spherical mesoporous silica particles (SMSP) with small pore size (about 2.4 nm) were also synthesized and their hemostatic ability was also evaluated.

The CBT tests and the hemolysis assays were performed in collaboration with the research group of Prof. Roberta Cavalli at the Department of Drug Science and Technology of the University of Turin.

3.2 Experimental

3.2.1 The synthesis of mesoporous silica microspheres (MSM)

The procedure used for the preparation of MSM was adapted from that proposed by *Wang et al.* [8]. This synthesis method provides a high yield (ca. 100 %) of well-defined SBA-15 spheres with a diameter of a few micrometers and large pores, using mesitylene and an inorganic salt under acid condition. In particular, the use of mesitylene and potassium chloride (KCl) allows large-pore SBA-15 with a spherical morphology to be obtained.

Briefly, 4.0 g of Pluronic P123 ($EO_{20}PO_{70}EO_{20}$, Aldrich) and 6.1 g of KCl were dissolved in 120 g of H_2O and 23.6 g of HCl (conc. 37%, Aldrich) at room temperature, which was followed by the addition of 3.0 g of mesitylene (98%, Aldrich). After 2 h of stirring, 8.5 g of tetraethyl orthosilicate (TEOS, Aldrich) was added dropwise and the mixture was stirred vigorously for 10 min. The final molar ratios of the reactants were 1 TEOS: 0.017 P123: 0.6 mesitylene: 2 KCl: 5.85 HCl: 165 H_2O. After, the mixture was maintained under static condition at 35 °C for 24 h. Then, differently from what reported by the authors, the mixture was transferred in a sealed PTFE bottle, and a hydrothermal treatment was performed at 100 °C for 24 h. The white precipitate was recovered by filtration, washed with water, and dried at 60 °C in an oven overnight.

Finally, the obtained product was calcined to remove the template. In the original work, the final product was calcined at 500 °C for 6 h at a heating rate of 1 °C/min with a total duration of the treatment of 14 h. Herein, in order to decrease the duration of calcination, a second treatment (the same used for the calcination of mesoporous silica particles presented in 3.2.2) with a shorter duration was carried out. In this case the powder was calcined at 500 °C for 6 h with a faster rate of heating of 15 °C/min, with a total duration of the treatment of 7 h.

The obtained samples were named MSM-1°C/min and MSM-15°C/min. From the above-described procedure an amount of about 2.0 g of material was obtained.

3.2.2 The synthesis of spherical mesoporous silica particles (SMSP)

SMSP were synthesized through a base-catalyzed reaction by a sol–gel process involving the use of hexadecyltrimethylammonium bromide (CTAB) as the surfactant and tetraethyl orthosilicate (TEOS) as the silica precursor. The material was prepared following the procedure reported by *Ambati et al.* [9], except for the amount of the employed reagents, which was doubled to obtain a larger quantity of material.

In detail, 2.2 g of CTAB were dissolved in 41.8 g of deionized water, 53.6 g of absolute ethanol and 13.8 g of an aqueous ammonia solution (28.0-30.0% NH_3 basis). The mixture was stirred for 30 minutes, then 4.2 g of TEOS were added dropwise with a continuous stirring. The reactant molar ratio was 1 TEOS: 0.3 CTAB: 11 NH_3: 58 C_2H_5OH: 144 H_2O. The solution was aged at room temperature under magnetic stirring for 2 h. The resulting white solid was filtered, washed with deionized water, and dried overnight. The dried powder was calcined in air at 500°C for 4 hours in a muffle furnace to remove the template.

From the above-described procedure an amount of about 1.0 g of SMSP was obtained.

3.2.3 Instrumental characterization

Nitrogen sorption analysis

Nitrogen adsorption-desorption analysis was performed using a Micromeritics ASAP 2020 Plus Physisorption analyser (Micromeritics, Norcross, GA, USA). Before the adsorption measurement, the samples were outgassed at 150 °C for 2 h. the specific surface area was calculated using the Barret-Emmett-Teller (BET) method in the relative pressure range of 0.099 - 0.179. The pore size distribution was achieved through the density functional theory (DFT) method. The average pore size was determined from the distribution. The total pore volume was determined at a relative pressure of about 0.99.

Field emission scanning electron microscopy

FESEM images were recorded with a Supra 40 instruments (Carl Zeiss, Oberkochen, Germany). Particle size distribution was calculated using the software "ImageJ." (Open source, https://imagej.net/).

Powder X-ray diffraction analysis

X-ray diffraction (XRD) patterns were achieved with a PANalytical X'Pert diffractometer (Malvern Panalytical, Almelo, The Neatherlands) using Cu Kα radiation (wavelength = 1.54187 Å). For low angle XRD patterns, the data were obtained from 0.3° to 5° (2θ) with a step size of 0.013° (2θ). For wide angle XRD patterns, the data were collected from 5° to 60° (2θ) with a step size of 0.026° (2θ).

Fourier Transform Infrared Spectroscopy

FT-IR analysis was performed using a Bruker Equinox 55 spectrometer (Bruker, Billerica, MA, USA). FT-IR spectra of pure materials were obtained on self-supported pellets, prepared by pressing the powder with a hydraulic press. All samples were outgassed in high vacuum (residual pressure: 0.1 Pa) at room temperature for 1 h. Spectra were obtained from 4000 cm^{-1} to 600 cm^{-1} with a resolution of 2 cm^{-1}.

3.2.4 *In vitro* blood coagulation test

The clotting blood time (CBT) test is a simple *in vitro* method used to evaluate the whole blood coagulation process. The test was performed according to the procedure reported in literature [5,7]. Briefly, 3 mg of sample was put in an Eppendorf tube and kept at 37 °C for 5 min. Then 250 µl of 3.2 % sodium citrate rat blood was added to the sample, which was followed by vortexing for 10 s, and incubated at 37 °C for 3 min. After, 25 µl of a 0,25 M calcium chloride ($CaCl_2$) aqueous solution was pipetted into the tube to activate the coagulation pathway. The tube was tilted every 15 s until the blood stopped to flow through the wall of the tube. The clotting time was used as the result of the CBT test.

3.2.5 Hemolysis assay

Hemolysis assay is a standard method used to study the effects that a material can produce on the blood. This method evaluates the percentage of hemoglobin (Hb) released into the plasma when a material is incubated with red blood cells (RBCs) [10]. Generally, when hemolysis occurs, different degrees of red tinge in serum or plasma can be observed once the blood specimen has been centrifuged. The extent and intensity of this interference depends on the degree of hemolysis [11]. To measure hemolysis rate, spectrophotometric analysis is performed on materials incubated with RBCs, as reported in Figure 3.1.

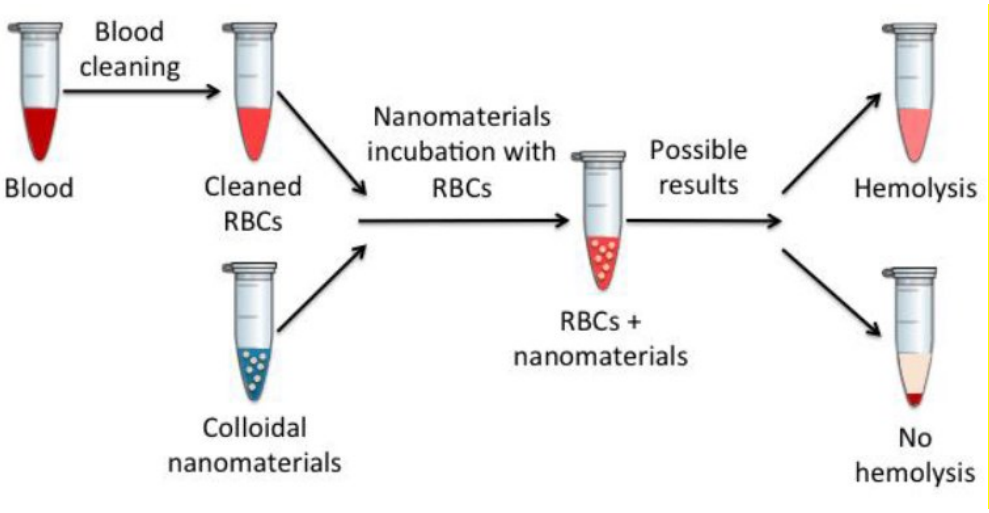

Figure 3.1 Schematic representation of the hemolysis assay [12].

The hemolytic activity of the samples was evaluated on rat blood diluted with PBS pH 7.4 (1:10 v/v). 100 µl of the samples prepared in saline solution (NaCl 0.9% w/v) at two different concentrations (1 mg/ml and 5 mg/ml) were incubated with 900 µl of diluted blood at 37 °C for 90 min, so that the final concentrations were 100 µg/ml and 500 µg/ml, respectively. After incubation, the samples were centrifuged at 2000 rpm for 10 min to separate the plasma. The amount of hemoglobin released in the supernatant due to hemolysis was measured spectrophotometrically at 543 nm (Du 730 spectrophotometer, Beckman). Saline solution (NaCl 0.9 % w/v) was used as negative control (i.e. 0% lysis, figure 3.2a) and complete hemolyzed sample (i.e. 100 % lysis, induced by the addition of Triton X-100 1 % w/v to the blood, figure 3.2b) was employed as positive control. The hemolysis rate was calculated according to the following equation:

$$\text{Hemolysis (\%)} = \frac{(\text{Abs sample} - \text{Abs neg})}{(\text{Abs pos} - \text{Abs neg})} \times 100$$

where Abs sample, Abs neg and Abs pos are the absorbance of the tested samples, negative control and positive control, respectively.

(a) (b)

Figure 3.2 (a) Negative control (0 % lysis) and (b) Positive control (100 % lysis).

3.3 Results and Discussion

3.3.1 Characterization of MSM

The physicochemical characterization of the as synthesized materials was performed by means of various techniques, among which the nitrogen sorption analysis, field emission scanning microscopy (FESEM) and FT-IR spectroscopy.

Nitrogen sorption analysis was used to evaluate the specific surface area, pore volume and pore size of the materials. Figure 3.3 reports the nitrogen adsorption-desorption isotherms of the MSM-1°C/min (orange lines) and MSM-15°C/min (black lines) samples. Sample MSM-1°C/min exhibits a type IV isotherm, according to IUPAC classification, with a broad H2 hysteresis loop associated to the presence of ink-bottle pores. Differently from what reported in the original work where a type IV isotherm with a H2(b) hysteresis was observed, sample MSM-1°C/min shows a hysteresis loop with features of both an H2(a) loop and an H2(b) loop. In particular, the desorption branch presents the characteristic features of an H2(a) loop (sharp step-down) as well as that of an H2(b) one suggesting the presence of necks with both narrow and large width [13]. On the other hand, sample MSM-15°C/min exhibits a type IV isotherm with an H5 hysteresis loop that

indicates the presence of both open and partially blocked mesopores [13]. The values of the BET surface area, pore volume, and average pore diameter are summarized in table 3.1. The pore size distribution of sample MSM-1°C/min is heterogeneous with the main contribution of mesopores diameter at 25 nm. Instead, sample MSM-15°C/min presents a unimodal pore size distribution with an average pore size of 25 nm (figure 3.4).

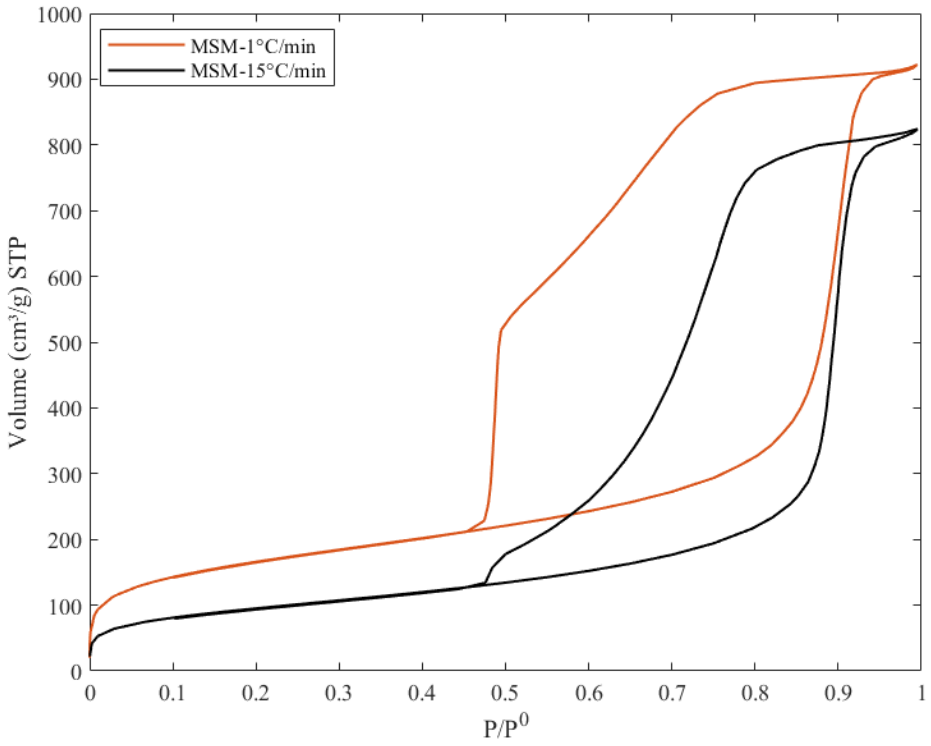

Figure 3.3 The nitrogen adsorption- desorption isotherm of MSM-1°C/min (orange curve) and MSM-15°C/min (black curve).

Table 3.1 SSA_{BET} and Pore volume of MSM-1°C/min and MSM-15°C/min.

Sample	SSA_{BET} (m^2/g)	Pore volume (cm^3/g)
MSM-1°C/min	591	0.91
MSM-15°C/min	342	1.27

The analysis of the results showed that the calcining heating rate influences the textural properties of MSM. As reported in table 3.1, the MSM-1°C/min sample showed a higher surface area with respect to the MSM-15°C/min one. These results are in agreement with the data reported in the literature where an increase in the surface area was observed in those materials that had been calcined at low heating rates [14–16].

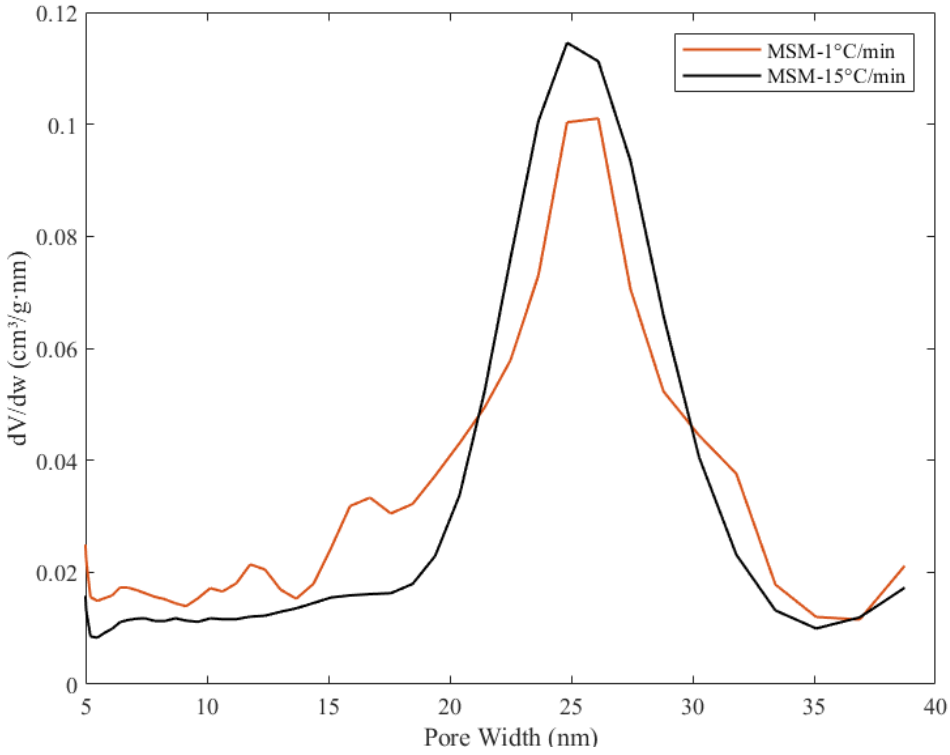

Figure 3.4 The DFT pore size distribution of MSM-1°C/min (orange curve) and MSM-15°C/min (black curve).

The influence of the calcination heating rate on the morphology of MSM-1°C/min and MSM-15°C/min was characterized by FESEM. Figure 3.5 reports the FESEM images, at low and high magnification, of MSM-1°C/min (figure 3.5a) and MSM-15°C/min (figure 3.5b). By comparing the images, it can be observed that both samples appear in the form of spheres with particle size ranging from 2 to 5 μm, so suggesting that the heating rate of calcination did not affect morphology of the particles.

(a)

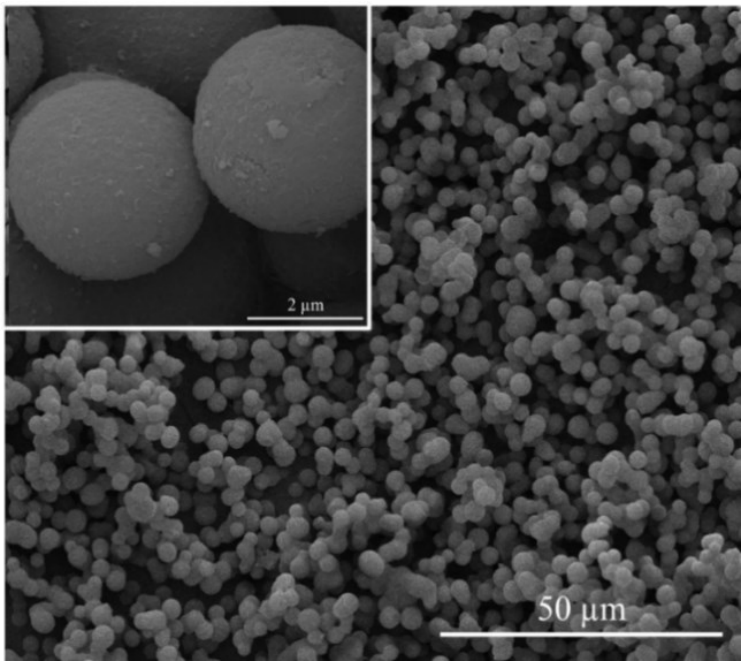

(b)

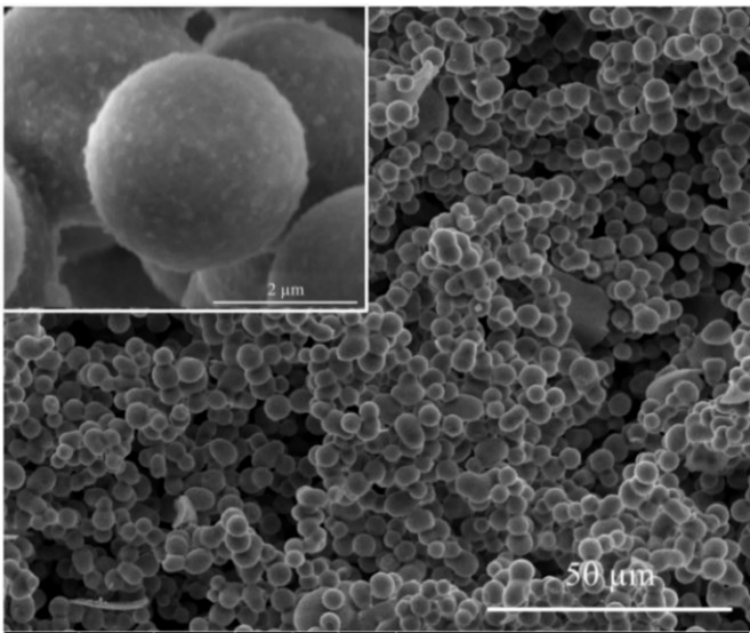

Figure 3.5 The FESEM images of (a) MSM-1°C/min and (b) MSM-15°C/min (magnification: 1.00 K X, 20.00 K X).

The FT-IR analysis was performed to investigate the effect of the heating rate of calcination on the surface properties of MSM. The FT-IR spectra of MSM-1°C/min and MSM-15°C/min are reported in figure 3.6. The infrared spectra of both samples exhibit the typical pattern of amorphous silica with two main bands: a narrow band at 3740 cm^{-1} due to the isolated silanols; and a broad absorption at about 3500 cm^{-1} due to silanols interacting via H-bonding [17]. However, the relative population of silanols types on the surface of the two samples appear to be affected by the heating rate of calcination. As far as the MSM-1°C/min sample is concerned, a lower relative abundance of H-bonded silanols, as well as a higher fraction of isolated silanols can be observed. The relative population of isolated and interacting silanols may affect the hydrophilicity of the silica surface, which is mainly ascribed to interacting silanols [18,19]. Thus, FT-IR evidences suggest that the surface of the MSM-15°C/min sample might be more hydrophilic than that of the MSM-1°C/min one [20]. This aspect is very important as the degree of hydrophobicity/hydrophilicity of the surface could influence the extent of the interaction of the particles with a biological medium as well as their toxicity [19–21].

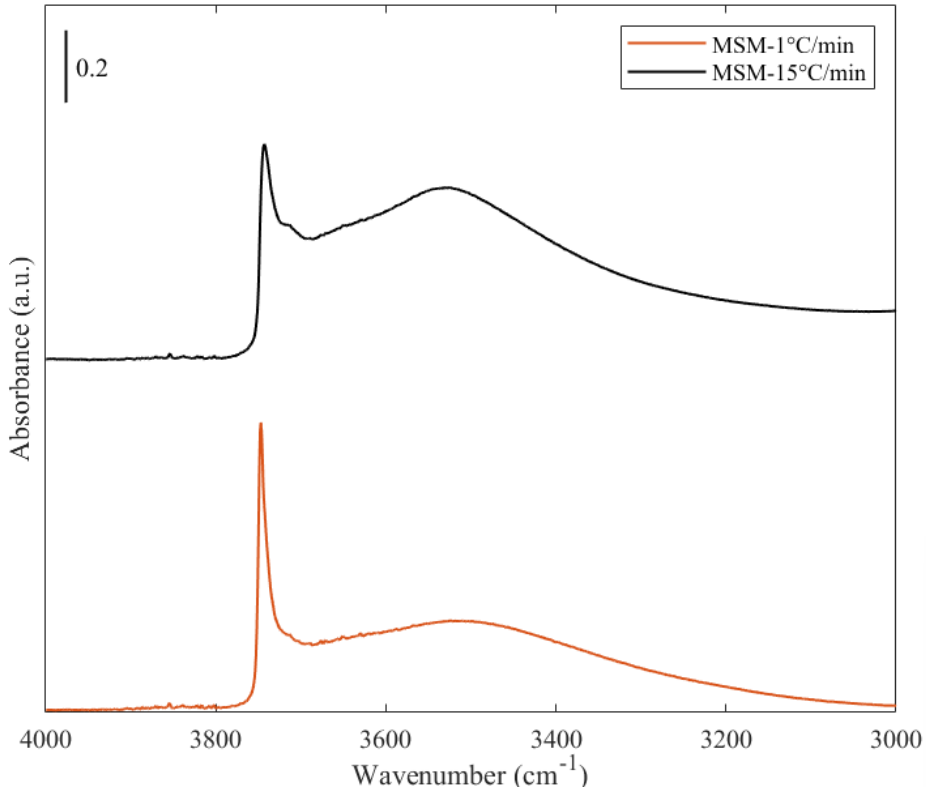

Figure 3.6 The FT-IR spectra of MSM-1°C/min and MSM-15°C/min

The X-ray diffraction patterns of both samples at low and wide angles are reported in figure 3.7. In the XRD patterns of MSM-1°C/min and MSM-15°C/min at low angles (figure 3.7 inset) no clear diffraction peaks due to ordered mesoporous structures are observed. This result suggests that the mesopores are disordered which is in accordance with the results gained from the nitrogen sorption analysis (figure 3.3). The XRD patterns of both samples at wide angles (figure 3.7) show the typical ill-defined scattering of amorphous silicas.

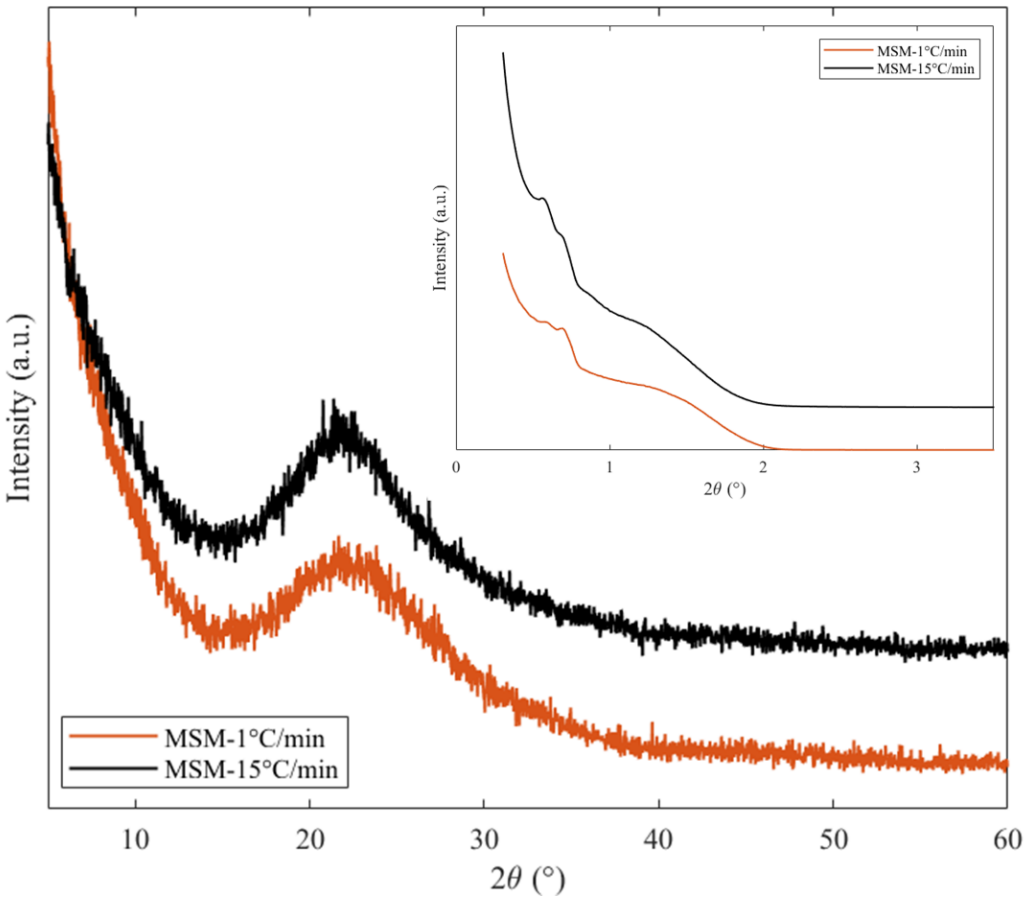

Figure 3.7 The XRD pattern of MSM-1°C/min and MSM-15°C/min at low (inset) and wide angles.

3.3.2 Characterization of SMSP

Nitrogen sorption measurement was used to evaluate the textural properties of SMSP. Figure 3.8 reports the nitrogen adsorption-desorption isotherms of SMSP. SMSP shows an isotherm type IV, according to the IUPAC classification, without hysteresis loop, and shows capillary condensation at a relative pressure in the 0.2-0.3 range, suggesting the presence of uniform mesopores. The pore size distribution (figure 3.8 inset) is unimodal and narrow with an average pore size of 2.4 nm.

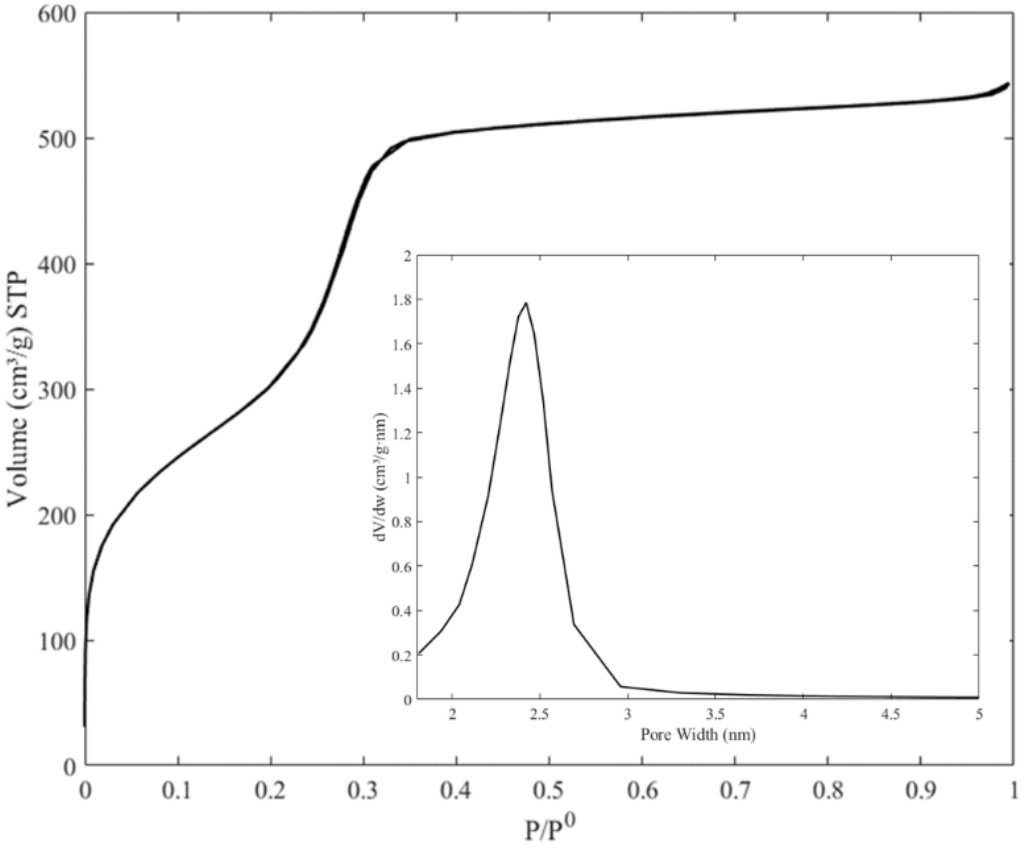

Figure 3.8 The nitrogen adsorption- desorption isotherm with BJH pore size distribution (inset) of SMSP.

The values of SSA_{BET} and pore volume are 1143 m^2/g and 0.82 cm^3/g, respectively.

The FESEM images, at low and high magnification, and particles size distribution of SMSP are reported in figures 3.9. The material appears composed of spheres (figure 3.9a) with a wide range of particle sizes, which ranges from 0.15

µm to 0.80 µm (figure 3.9b). The wide particle size distribution could be the result of the rapid precipitation and aggregation of the particles during the synthesis process, which leads to the formation of radially oriented mesopores [9].

(a)

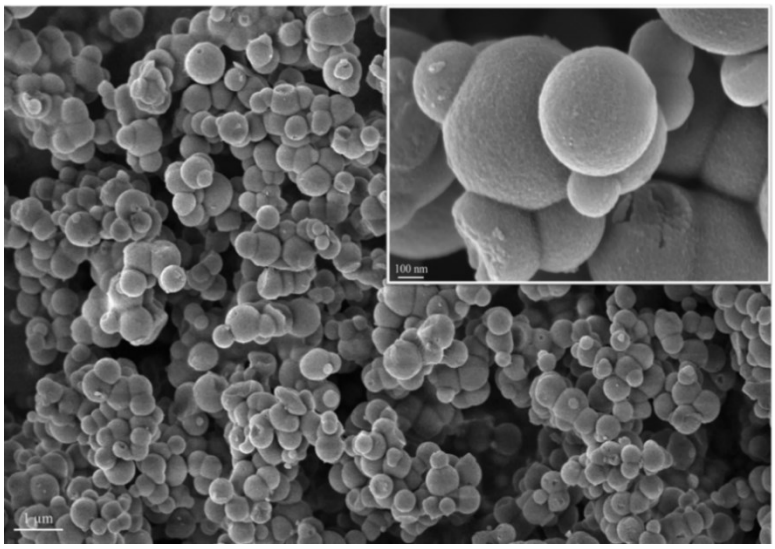

(b)

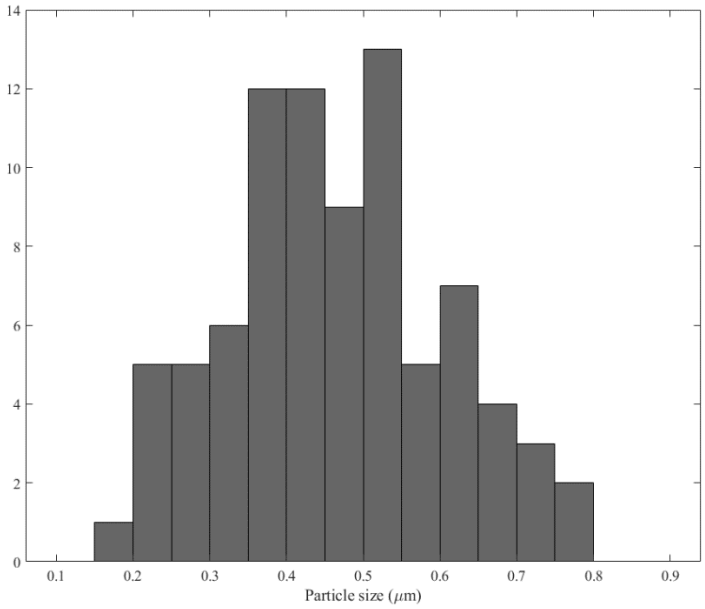

Figure 3.9 (a) The FESEM images (magnification: 25.00 K X, 250.00 K X) and (b) particles size distribution of SMSP.

Figure 3.10 shows the FT-IR spectrum of SMSP. The spectrum is typical of amorphous silica, with the narrow band at 3746 cm^{-1} due to the isolated silanols and a broad absorption at about 3530 cm^{-1} due to H-bonded silanols [17].

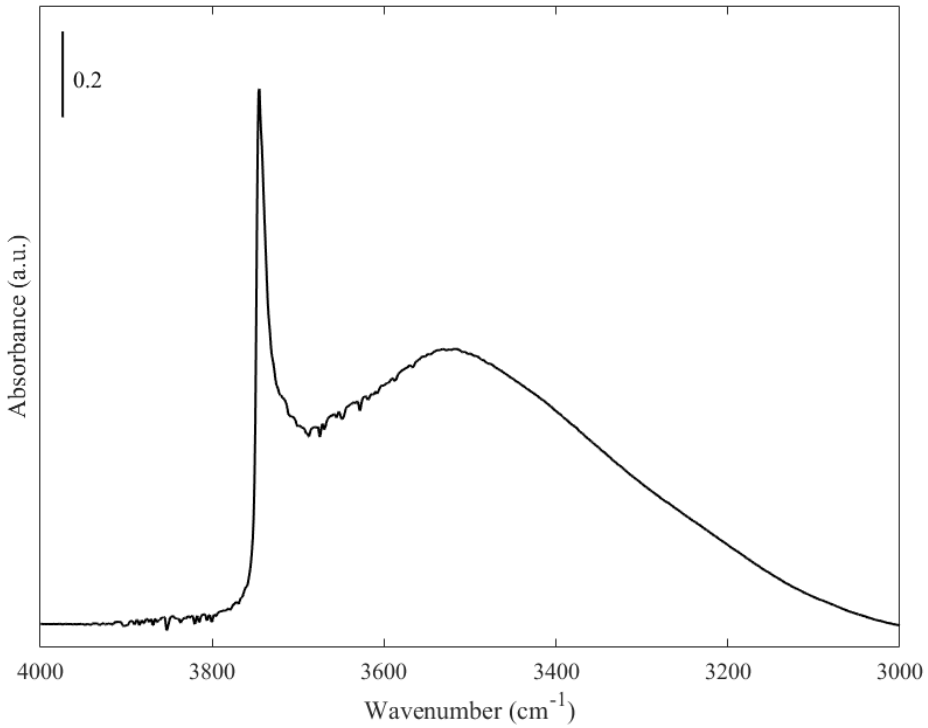

Figure 3.10 The FT-IR spectrum of SMSP

Figure 3.11 reports the X-ray diffraction pattern of SMSP at low (figure 3.11a) and wide angles (figure 3.11b). The XRD pattern at low angles presents a main characteristic peak due to the (100) reflection at 2.43° 2θ and an ill-defined scattering between 4° and 6°. The broad diffraction could be associated to the presence of small domains of ordered structure in the material with a radial orientation of the pore channels. This result suggests that a hexagonal arrangement, expected on the basis of the synthesis route [9] takes place on a local scale and that the deviation from the hexagonal symmetry occurs due to the spherical shape of the particles, which is in accordance with FESEM analysis (figure 3.9a) [22,23]. The XRD pattern at Wide angles shows the absence of crystalline peaks, which indicates that the material is amorphous.

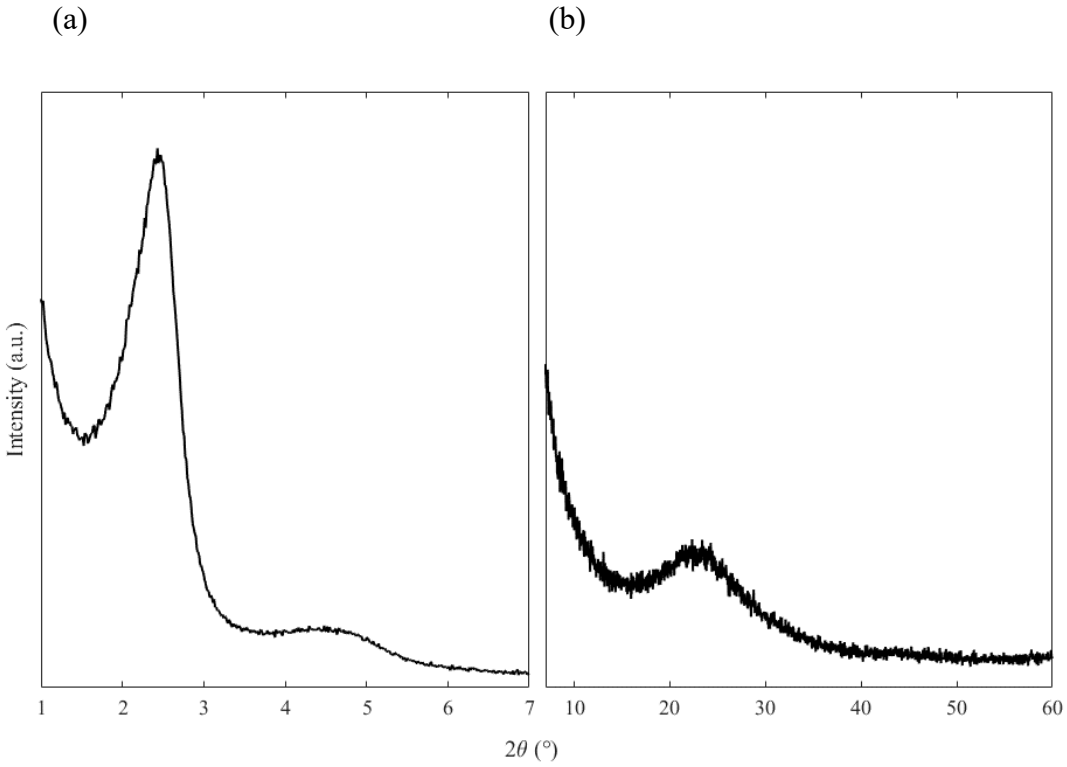

Figure 3.11 The XRD pattern of SMSP at low (a) and wide angles (b).

3.3.3 Clotting blood time test

The *in vitro* hemostatic efficiency of the samples was evaluated by a clotting blood time (CBT) test. This test measures the time that blood needs to form a clot. As shown in figure 3.12, it can be observed that the clotting times of SMSP, MSM-1°C/min and MSM-15°C/min were significantly shorter than the control (140 ± 8,67 s). Moreover, the results of the CBT suggest that silica particles with larger pores (i.e., MSM-1°C/min and MSM-15°C/min) might have better hemostatic performance with respect to those with smaller pore size (i.e., SMSP), which is in agreement with the data available in the literature [6,7]. In addition, the CBT of MSM-15°C/min was the shortest among all samples. This could be ascribed to the fact that the MSM-15°C/min sample presents a more hydrophilic surface than that of MSM-1°C/min, which might have enhanced its hemostatic performance by improving the fluid absorption and, consequently, by accelerating blood clotting [24,25]. Moreover, it cannot be ruled out the effect of a different reactivity of isolated

silanols and interacting silanols in the clotting process, with a higher efficacy of the latter.

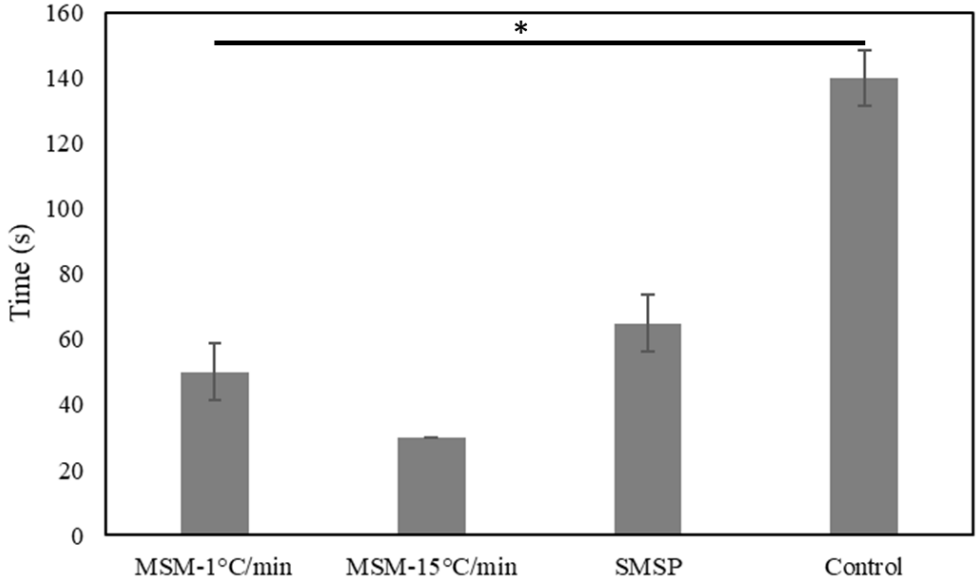

Figure 3.12 The CBT for MSM-1°C/min, MSM-15°C/min, SMSP and control. Data are represented as mean ± SD (n=3). * Significant difference ($p < 0.05$) analysed by one-way ANOVA.

3.3.4 Hemolysis assay

Besides being efficient, a hemostatic agent should not cause hemolysis. Herein, a hemolysis assay was performed to evaluate the blood compatibility of SMSP, MSM-1°C/min and MSM-15°C/min as it is known that silica-based materials could cause damage to red blood cells (RBCs) [26]. Figure 3.13 reports the hemolysis ratio of SMSP, MSM-1°C/min and MSM-15°C/min at two different concentrations (i.e., 100 and 500 µg/ml). The results of the hemolysis assay showed that all samples did not have any hemolytic activity, indicating that all materials are blood compatible.

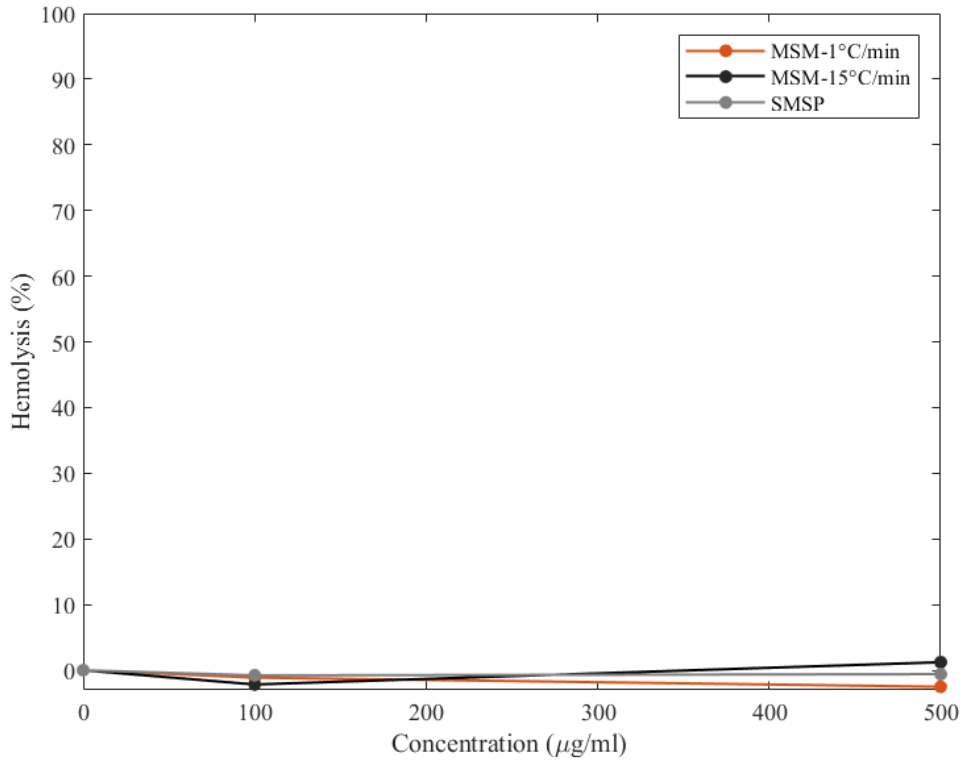

Figure 3.13 The hemolysis ratio for MSM-1°C/min, MSM-15°C/min and SMSP at two different concentrations (100 and 500 μg).

3.4 Conclusions

This chapter focused on the development of a hemostatic material that can exploit the hemostatic nature of mesoporous silica. MSM (with particle size ranging from 1 to 5 μm and an average pore diameter of 25 nm) and SMSP (with particle sizes ranging from 0.15 to 0.80 μm and an average pore diameter of 2.4 nm) were synthesized, characterized and their hemostatic performance was investigated. The results of the CBT tests revealed that the three samples were able to promote blood clotting, in accordance with the literature. More specifically, the MSM-15°C/min sample exhibited the best hemostatic ability, which was attributed to its larger pores and the hydrophilicity of the surface with respect to MSM-1°C/min. Moreover, the hemolysis assay carried out on MSM-1°C/min, MSM-15°C/min and SMSP at two different concentrations (i.e., 100 and 500 μg/ml) indicated that all samples possessed good hemocompatibility.

In conclusion, this study suggests that the clotting efficiency of mesoporous silica particles was influenced by the pore size as well as surface hydrophilicity. MSM-15°C/min showed the best hemostatic ability, which suggests that it could be used for the development of new materials for hemorrhage control.

3.5 References

1. Mohamed, S. S. Y. *et al.* The Role of the pH in the Impregnation of Spherical Mesoporous Silica Particles with L-Arginine Aqueous Solutions. *Int. J. Mol. Sci.* **22**, 13403 (2021).

2. Schreiber, M. A. & Neveleff, D. J. Achieving hemostasis with topical hemostats: Making clinically and economically appropriate decisions in the surgical and trauma settings. *AORN J.* **94**, S1–S20 (2011).

3. Pourshahrestani, S., Zeimaran, E., Djordjevic, I., Kadri, N. A. & Towler, M. R. Inorganic hemostats: The state-of-the-art and recent advances. *Mater. Sci. Eng. C* **58**, 1255–1268 (2016).

4. Pourshahrestani, S., Kadri, N. A., Zeimaran, E. & Towler, M. R. Well-ordered mesoporous silica and bioactive glasses: Promise for improved hemostasis. *Biomater. Sci.* **7**, 31–50 (2019).

5. Wang, C. *et al.* Tannic acid-loaded mesoporous silica for rapid hemostasis and antibacterial activity. *Biomater. Sci.* **6**, 3318–3331 (2018).

6. Baker, S. E. *et al.* Blood clot initiation by mesocellular foams: Dependence on nanopore size and enzyme immobilization. *Langmuir* **24**, 14254–14260 (2008).

7. Chen, Z. *et al.* Blood clot initiation by mesoporous silica nanoparticles: Dependence on pore size or particle size? *J. Mater. Chem. B* **4**, 7146–7154 (2016).

8. Wang, L., Qi, T., Zhang, Y. & Chu, J. Morphosynthesis route to large-pore SBA-15 microspheres. *Microporous Mesoporous Mater.* **91**, 156–160 (2006).

9. Ambati, J. *et al.* Engineered silica nanocarriers as a high-payload delivery vehicle for antioxidant enzymes. *Acta Biomater.* **8**, 2096–2103 (2012).

10. Mukhopadhyay, S. *et al.* Synthesis and compatibility evaluation of versatile mesoporous silica nanoparticles with red blood cells: an overview. *RSC Adv.* **9**, 35566–35578 (2019).

11. Deneyimi, A. Experience in Reducing Hemolysis in the Emergency Laboratory Acil Laboratuvarda Hemoliz Oranlar ı n ı. **19**, 71–76 (2021).

12. Fornaguera, C. & Solans, C. Methods for the In Vitro Characterization of Nanomedicines—Biological Component Interaction. *J. Pers. Med.* **7**, 2 (2017).

13. Thommes, M. *et al.* Physisorption of gases, with special reference to the evaluation of surface area and pore size distribution (IUPAC Technical Report). *Pure Appl. Chem.* **87**, 1051–1069 (2015).

14. Kumar, S., Malik, M. M. & Purohit, R. Synthesis of high surface area mesoporous silica materials using soft templating approach. *Mater. Today Proc.* **5**, 4128–4133 (2018).

15. Rahman, S. *et al.* The effect of calcination rate on the structure of mesoporous bioactive glasses. *J. Sol-Gel Sci. Technol.* **89**, 426–435 (2019).

16. Shih, C. J. *et al.* Synthesis and in vitro bioactivity of mesoporous bioactive glass scaffolds. *Mater. Sci. Eng. C* **30**, 657–663 (2010).

17. A. Rimola, D. Costa, M. Sodupe, J.-F. Lambert, P. U. Silica Surface Features and Their Role in the Adsorption of Biomolecules: Computational Modeling and Experiments. *Chem. Rev* **113**, 4216–4313 (2013).

18. Bolis, V., Fubini, B., Marchese, L., Martra, G. & Costa, D. Hydrophilic and hydrophobic sites on dehydrated crystalline and amorphous silicas. *J. Chem. Soc. Faraday Trans.* **87**, 497 (1991).

19. Catalano, F., Alberto, G., Ivanchenko, P., Dovbeshko, G. & Martra, G. Effect of Silica Surface Properties on the Formation of Multilayer or Submonolayer Protein Hard Corona: Albumin Adsorption on Pyrolytic and Colloidal SiO 2 Nanoparticles. *J. Phys. Chem. C* **119**, 26493–26505 (2015).

20. Croissant, J. G., Butler, K. S., Zink, J. I. & Brinker, C. J. Synthetic amorphous silica nanoparticles: toxicity, biomedical and environmental implications. *Nat. Rev. Mater.* **5**, 886–909 (2020).

21. Pavan, C. *et al.* Nearly free surface silanols are the critical molecular moieties that initiate the toxicity of silica particles. *Proc. Natl. Acad. Sci.*

117, 27836–27846 (2020).

22. Jiang, Y., Lee, C., Wang, Q., Deng, Y. & Fu, D. Monodisperse mesoporous silica nanospheres with radially oriented mesochannels and their size effect on cell uptake. *Microporous and Mesoporous Materials* vol. **181,** 248–253 (2013).

23. Liu, S. *et al.* The Influence of the Alcohol Concentration on the Structural Ordering of Mesoporous Silica: Cosurfactant versus Cosolvent. *J. Phys. Chem. B* **107**, 10405–10411 (2003).

24. Hunt, B. J., Parratt, R., Cable, M., Finch, D. & Yacoub, M. Activation of coagulation and platelets is affected by the hydrophobicity of artificial surfaces. *Blood Coagul. Fibrinolysis* **8**, 223–231 (1997).

25. Kopf, B. S., Ruch, S., Berner, S., Spencer, N. D. & Maniura-Weber, K. The role of nanostructures and hydrophilicity in osseointegration: In-vitro protein-adsorption and blood-interaction studies. *J. Biomed. Mater. Res. - Part A* **103**, 2661–2672 (2015).

26. Slowing, I. I., Wu, C. W., Vivero-Escoto, J. L. & Lin, V. S. Y. Mesoporous silica nanoparticles for reducing hemolytic activity towards mammalian red blood cells. *Small* **5**, 57–62 (2009).

Chapter 4
Mesoporous silica microspheres containing tranexamic acid

4.1 Introduction

The present chapter deals with the development of a hemostatic material based on mesoporous silica spheres loaded with tranexamic acid (TXA). This aims at combining the hemostatic ability of mesoporous silica particles (Chapter 3) with the antifibrinolytic properties of tranexamic acid, to be used in the management of massive bleeding in trauma settings. The aim was to develop a system able to promote the formation of blood clot by exploiting the hemostatic ability of MS, and to prevent any possible dissolution of the clot by releasing the TXA.

Tranexamic acid, trans-4-(aminomethyl) cyclohexanecarboxylic acid (figure 4.1), is a synthetic antifibrinolytic drug widely used to manage the excessive blood loss resulting from trauma, surgery, or bleeding disorders. It is a derivative of lysine, which inhibits the breakdown of fibrin clot by reversibly binding the lysine sites on plasminogen molecules thereby stabilizing the clot and preventing excessive bleeding caused by hyperfibrinolysis [1].

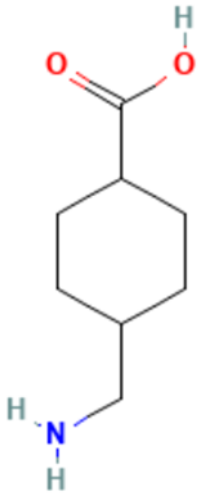

Figure 4.1 The chemical structure of tranexamic acid (TXA) [2].

The effect of early administration of TXA on death, vascular occlusive events, and the receipt of blood transfusion in trauma patients was studied in a large placebo-controlled double-blind randomized trial CRASH-2 (Clinical Randomization of an Antifibrinolytic in Significant Hemorrhage-2) [3]. The randomized trial included 20211 adult trauma patients with, or at risk of, significant bleeding recruited in 274 hospitals in 40 countries. The outcomes of the trial showed that the administration of TXA significantly reduced the occurrence of death due to bleeding without increasing the risk of a thrombotic onset. The greatest efficacy was achieved when the administration of TXA occurred within one hour after the traumatic event. A minor positive effect was found when the TXA was given between 1 and 3 hours. In contrast, the administration of TXA after 3 hours did not seem to have any beneficial effect.

Based on the outcomes of the above discussed CRASH-2 trial, it emerges that administration of TXA can be considered useful for bleeding management in trauma patients and that a timely treatment is essential to guarantee a correct action. However, the administration of TXA by means of conventional routes presents some disadvantages. Orally-administered TXA presents low bioavailability (30-50%) and it may cause gastrointestinal side effects while intravenous administration could cause hypotension due to the formation of intravenous boluses and it requires trained persons for the administration [4,5]. In addition also topical application presents some drawbacks since the permeability and retention of TXA are not optimal due to its hydrophilic nature (the water solubility is 167000 mg/L) and low

affinity with the lipidic composition of the skin [6]. An effective alternative approach to improve the efficacy of TXA is the use carriers to control its release [4,7–13].

Herein, mesoporous silica microspheres with large pores (MSM presented in Chapter 3) were synthesized and, for the first time, loaded with TXA to prepare a hemostat that combines the hemostatic efficiency of both excipients. In particular MSM-15°C/min was chosen as the carrier for the loading of TXA as it presented the best hemostatic performance with respect to the other ones (see Chapter 3). TXA was loaded by the incipient wetness impregnation method and the obtained sample was characterized by means of nitrogen sorption analysis, X-Ray diffraction (XRD), thermogravimetry analysis (TGA) and Fourier transform infrared (FT-IR) spectroscopy. The hemostatic performance of the loaded material was evaluated by means of a clotting blood time (CBT) test. Finally, a preliminary *in vitro* release test was performed in an isotonic solution (NaCl 0.9% w/v) to determine the release ability of the carrier.

4.2 Experimental

4.2.1 Tranexamic acid loading

TXA was loaded into MSM-15°C/min through the incipient wetness impregnation (IWI) technique and using water as a solvent. The IWI method is commonly used to load drugs into mesoporous materials. This process involves the addition of a known volume of a concentrated drug solution to the material. The added volume is approximately equal to the pore volume of the particles. In this way, the liquid quickly fills the pores by capillarity and the drug is adsorbed to the surface of the material [14]. The low volume of the employed solution makes this method quite suitable in the case of expensive drugs since it allows minimal quantities of the active principle to be used [15].

Given the absence of references in the literature where the impregnation of mesoporous silicas with tranexamic acid is reported, other cases of impregnation of TXA in different materials were analyzed [4,9,12,16]. From the analysis of the literature, it was found that the amount of loaded TXA ranged from 0.5 to10 % (w/w) and that most frequently amount of drug loaded in a solid carrier was equal to 2-3-%. Therefore, an intermediate value of 5 % (w/w), which is higher than the most frequent one, was chosen for investigating the loading of TXA into MSM-

15°C/min. For the impregnation, 15 mg of TXA were dissolved in 0.36 ml of water, then the solution was added dropwise to 285 mg of MSM so that the final drug content was equal to 5 % (w/w). The slurry was mixed vigorously using a spatula, and the sample was kept drying at room temperature overnight. The achieved material was named TXA@MSM-15°C/min.

4.2.2 Characterization

Thermogravimetric analysis (TGA) was carried using a SETARAM 92 instrument (Caluire, France) from 25 °C to 800 °C with a heating rate of 10 °C/min in air flow.

Nitrogen adsorption-desorption analysis was performed using a Micromeritics ASAP 2020 Plus Physisorption analyzer (Micromeritics, Norcross, GA, USA). Before the adsorption measurement, the TXA@MSM-15°C/min sample was outgassed at 70 °C for 2 h. the specific surface area was calculated using the Barret-Emmett-Teller (BET) method in the relative pressure range of 0.099 - 0.179. Pore size distribution was achieved through the density functional theory (DFT) method, and the average pore size was determined from the distribution. The total pore volume was determined at a relative pressure of about 0.99.

X-ray diffraction (XRD) patterns were obtained with a PANalytical X'Pert diffractometer (Malvern Panalytical, Almelo, The Neatherlands) using Cu Kα radiation (wavelength = 1.54187 Å). The data were collected from 5° to 60° (2θ) with a step size of 0.026° (2θ).

The FT-IR analysis was performed using a Bruker Equinox 55 spectrometer (Bruker, Billerica, MA, USA) on self-supported pellets, prepared by pressing the powder with a hydraulic press. For TXA, the powder was diluted in KBr. The samples were outgassed in high vacuum (residual pressure equal to 0.1 Pa) at room temperature for 1 h. The spectra were obtained from 4000 cm^{-1} to 600 cm^{-1} with a resolution of 2 cm^{-1}.

To evaluate if the presence of TXA molecules on the surface of MSM-15°C/min had any effect on its hemostatic ability, a CBT test was performed as described in Chapter 3 (subsection 3.2.4).

4.2.3 Preliminary in vitro release test

To understand the release behavior of TXA, a simple dissolution test was carried out using an isotonic solution (NaCl 0.9 % w/v) as the receiving medium. 10 mg of TXA@MSM-15°C/min were soaked in 10 ml of the isotonic solution. At predetermined time intervals (30 and 60 minutes), 0,75 ml of the receiving phase was withdrawn and replaced by an equal amount of fresh solution to maintain a constant volume. After 60 minutes, the powder was recovered by filtration, dried upon complete evaporation of the solvent, and analyzed by FT-IR spectroscopy. The analysis was performed on a self-supporting pellet, prepared by pressing the powder with a hydraulic press. Before the measurement the sample was outgassed in high vacuum (residual pressure of 0.1 Pa) at room temperature for 1 hour. Then, the obtained spectrum was compared with the spectrum of TXA@MSM-15°C/min, i.e., the sample before the dissolution test.

To further confirm the released amount of TXA, the receiving solution was analyzed for the TXA content after its derivatization with a ninhydrin solution by means of a spectrophotometric method based on the detection of the Ruhemann's purple. Derivatization was performed according to the procedure reported by *Ansari et al.* [17] as follows: 1 ml of a phosphate buffer (pH 8) and 2 ml of a ninhydrin solution (0.2 % in methanol) were added to 0.5 ml of the release medium. The mixture was heated for 20 min at 90 °C using paraffin oil. Then, the mixture was cooled and transferred into a 10 ml flask and the volume was made up to the mark with the isotonic solution. Absorbance was measured at 570 nm using a Lambda 25 Perkin Elmer spectrophotometer (the calibration line was obtained by applying the above cited method to TXA solutions with concentrations in the range of 1-5 μg/ml).

4.3 Results and Discussion

4.3.1 Characterization of TXA@MSM-15°C/min

The material was characterized after TXA loading by means of TGA, nitrogen sorption analysis, XRD, and FT-IR Spectroscopy. The results of the characterization are here discussed.

TGA curves of the unimpregnated (MSM-15°C/min) and impregnated (TXA@MSM-15°C/min) sample are reported in figure 4.2. The unloaded MSM-15°C/min sample shows an initial weight loss of 1.9 % up to 150 °C, which can be assigned to the loss of the water physically adsorbed on the material surface. The gradual and small weight loss (about 0.3 %) observed at temperatures higher than 200 °C could be ascribed to surface dihydroxylation [18]. The TGA curve of TXA@MSM-15°C/min shows an initial weight loss of about 1.4 % probably due to the presence of adsorbed water. A further weight loss can be observed from 200 °C to 800 °C, which can be ascribed to the TXA removal. The TXA amount in the TXA@MSM-15°C/min sample was determined from the weight loss between 200°C and 800°C after subtracting the weight loss measured in the same temperature range for MSM-15°C/min. This was found to be equal to about 4.7 % w/w, which can be considered in fair agreement with the TXA nominal content (5 % w/w).

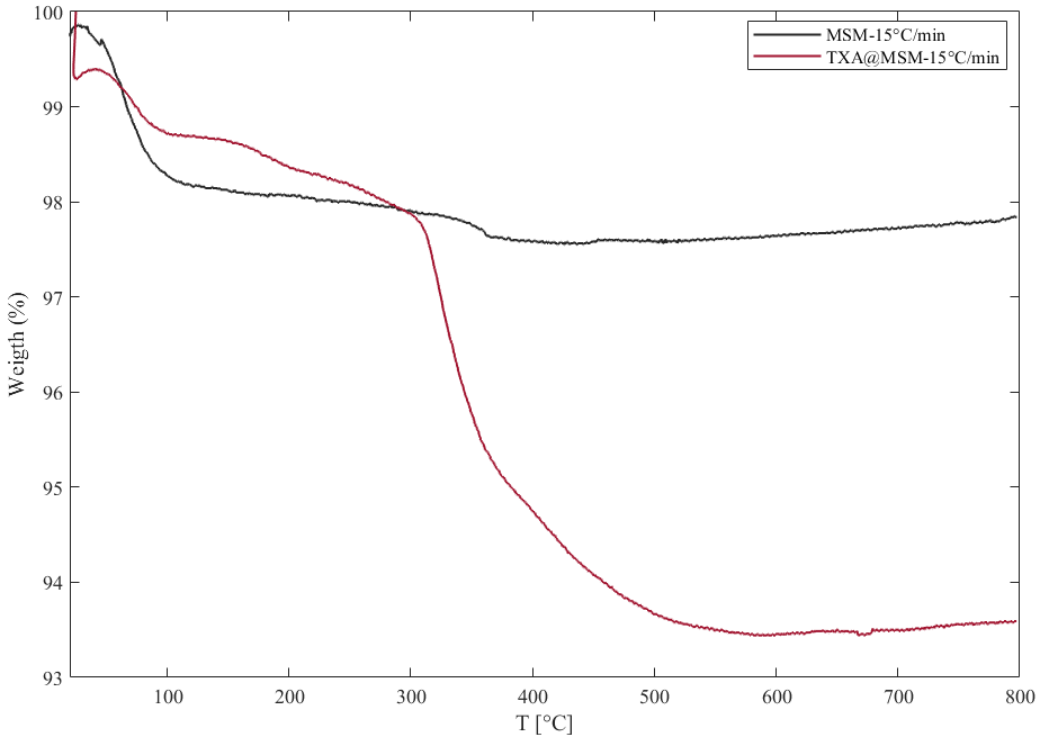

Figure 4.2 TGA curves of MSM-15°C/min and TXA@MSM-15°C/min.

The nitrogen adsorption-desorption isotherms of the MSM-15°C/min before and after the loading of TXA are shown in figure 4.3 (section a). The isotherm of

the drug loaded sample, TXA@MSM-15°C/min, is similar to that of MSM-15°C/min as such. The SSA_{BET} decreased from 342 m^2/g, for the as synthesized material, to 325 m^2/g after the loading of TXA, while the pore volume decreased from 1.27 to 1.22 cm^3/g. The pore size distributions obtained from the nitrogen adsorption-desorption isotherm are reported in figure 4.3 (section b). As far as TXA@MSM-15°C/min sample is concerned, no significant change could be observed when compared to MSM-15°C/min; the system still possesses a narrow pore size distribution with an average pore diameter of 25 nm. The above results suggest that TXA molecules are well dispersed and homogeneously distributed on the surface of the mesopores and that no pore occlusion occurred due to the presence of the drug molecules.

(a)

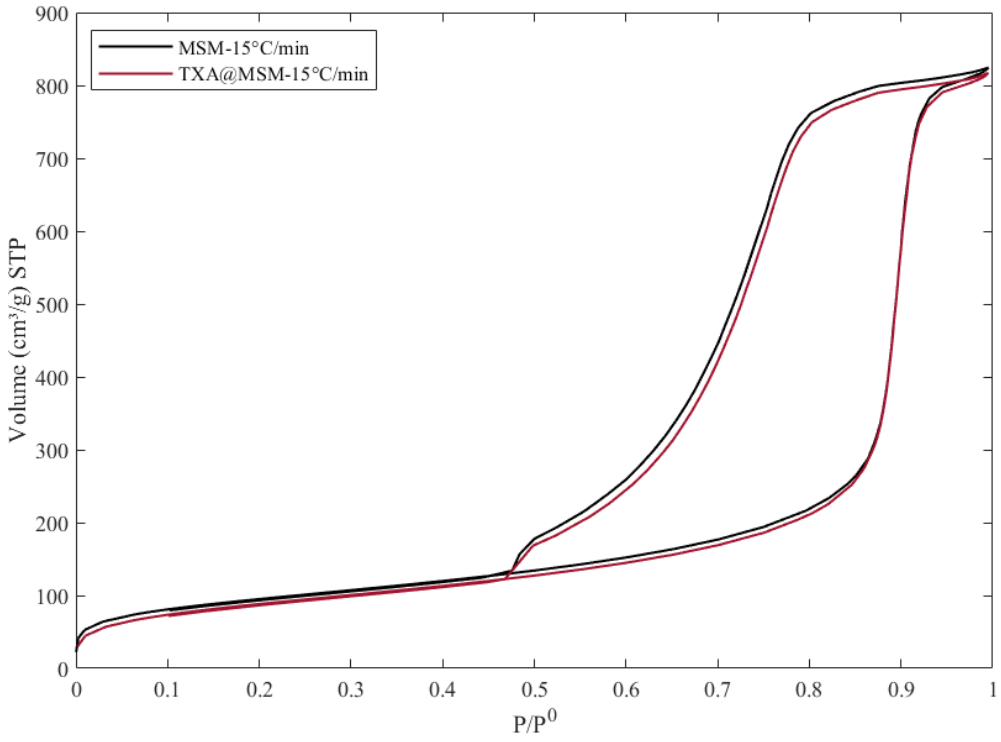

(b)

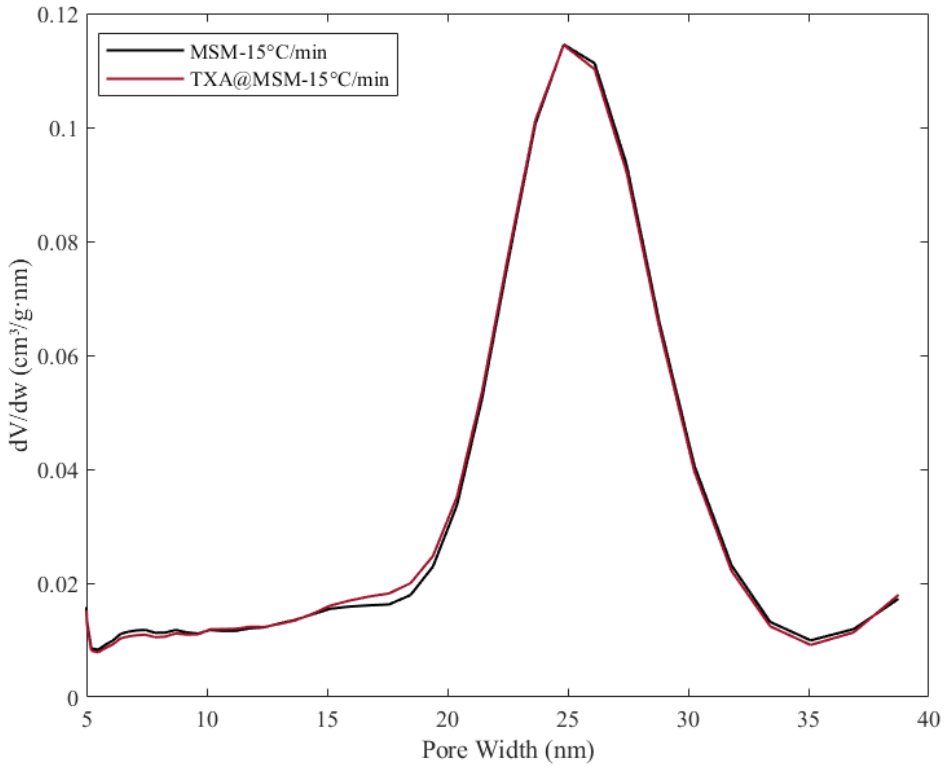

Figure 4.3 (a) Nitrogen adsorption-desorption isotherms and (b) PSD of MSM-15°C/min and TXA@MSM-15°C/min.

To investigate the physical state of TXA inside the pores, XRD analysis was carried out on the TXA@MSM-15°C/min sample. The XRD patterns of MSM-15°C/min, TXA@MSM-15°C/min and pure TXA are reported in figure 4.4. The XRD pattern of pure TXA presents well-defined peaks of the crystalline phase. The XRD patterns of MSM-15°C/min and TXA@MSM-15°C/min are typical of amorphous silica and no peaks due to crystalline TXA are observed in the TXA@MSM-15°C/min sample, so suggesting the presence of the amorphous form of TXA.

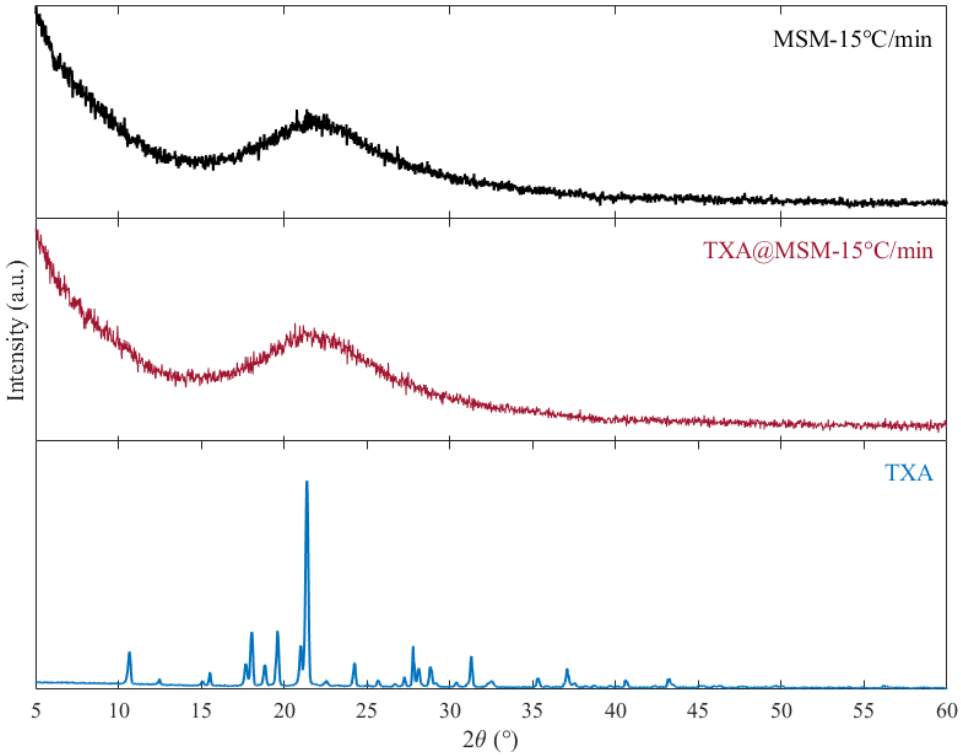

Figure 4.4 XRD patterns of MSM-15°C/min, TXA@MSM-15°C/min and pure TXA.

To characterize the TXA molecules in the sample, FT-IR spectroscopy was performed on TXA@MSM-15°C/min sample. The FT-IR spectra of MSM-15°C/min, TXA@MSM-15°C/min and pure TXA are shown in figure 4.5. As far as the spectrum of TXA@MSM-15°C/min is concerned, a reduction of the intensity of the peak associated to isolated silanols is observed. Moreover, a new broad absorption peak appears in the range 3500-2500 cm^{-1}, to which two narrower bands are superimposed. The decrease in the intensity of the peak ascribed to isolated silanols suggests that in TXA@MSM-15°C/min these are perturbed, probably by the H-bonding interaction with the TXA molecules, so forming the new broad absorption below 3500 cm^{-1}. The narrower bands at 2934 cm^{-1} and 2858 cm^{-1} are attributed to the vibrations of the $-CH_2-$ groups present in the alkyl ring of TXA, respectively [19]. Other several characteristic bands of TXA can be observed in the 1300 -1600 cm^{-1} range. In particular, an intense band at about 1541 cm^{-1} is observed, which is ascribed to the symmetric deformation mode of protonated amine groups $-NH_3^+$ [19,20]. A second intense band appears at about 1400 cm^{-1}, which can be attributed to both the bending vibrations of $-CH_2-$ groups [21] and the

symmetric stretching vibration of carboxylate -COO^- species [19,22]. The antisymmetric stretching vibration of the same COO^- groups, which is expected to appear in the spectrum above 1500 cm^{-1}, more likely contributes to the band observed between 1600 cm^{-1} and 1500 cm^{-1}. These results suggest that TXA is present on the silica surface in the zwitterionic form [4,20].

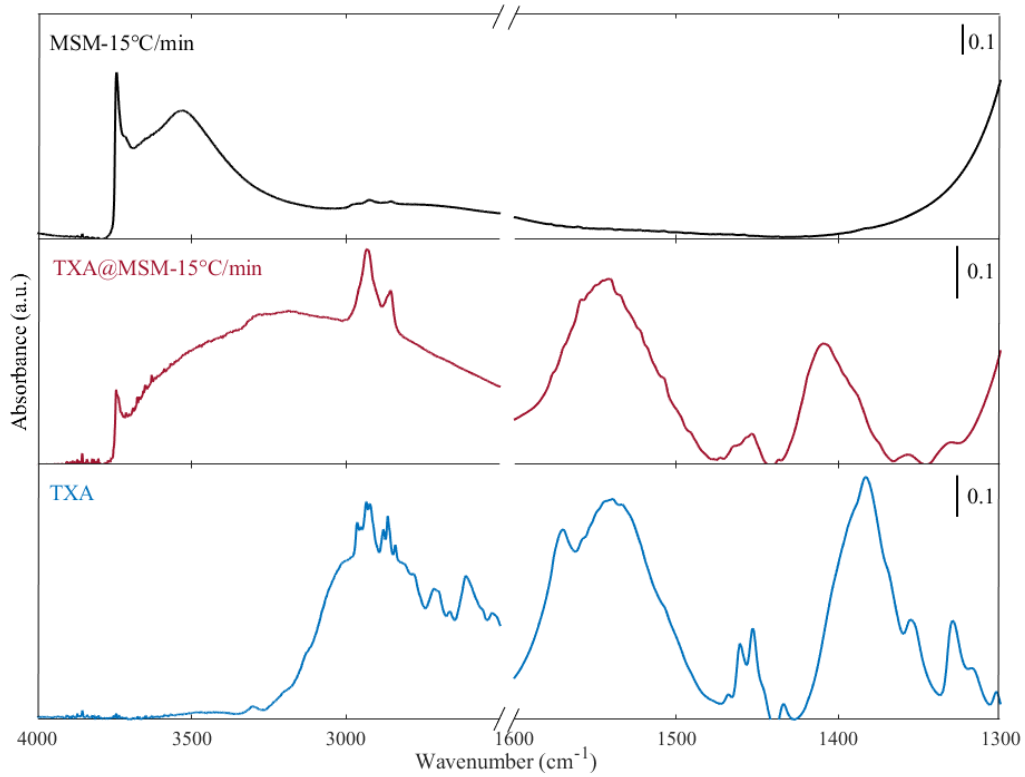

Figure 4.5 FT-IR spectra of MSM-15°C/min, TXA@MSM-15°C/min, and pure TXA.

The results of the CBT test for MSM-15°C/min and TXA@MSM-15°C/min are reported in figure 4.6 and indicate that both samples exhibited good hemostatic performance, and that the presence of TXA on the surface of the material did not affect the ability of MSM-15°C/min in inducing the activation of the coagulation cascade.

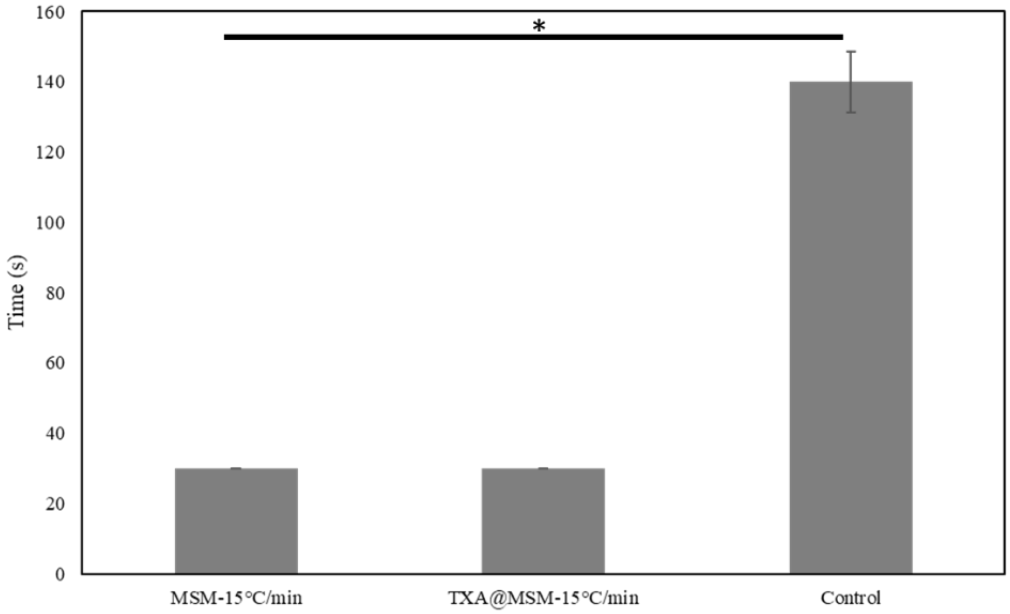

Figure 4.6 CBT for MSM-15°C/min, TXA@MSM-15°C/min and control. Data are represented as mean ± SD (n=3). * Significant difference ($p < 0.05$) analysed by one-way ANOVA.

4.3.2 A preliminary in vitro release test

The aim of the *in vitro* release study of TXA was to verify the possibility of a fast release of the drug from the microspheres since a fast release represents an important factor in bleeding control [3], as previously described.

The FT-IR spectrum performed on the powder recovered after the release test (60 minutes) is reported in figure 4.7. The spectrum of TXA@MSM-15°C/min-60 min did not show any band related to TXA, so suggesting its complete release within an hour. This result is very interesting since, as mentioned earlier, the maximum efficacy is achieved when the administration of TXA occurs within the first hour.

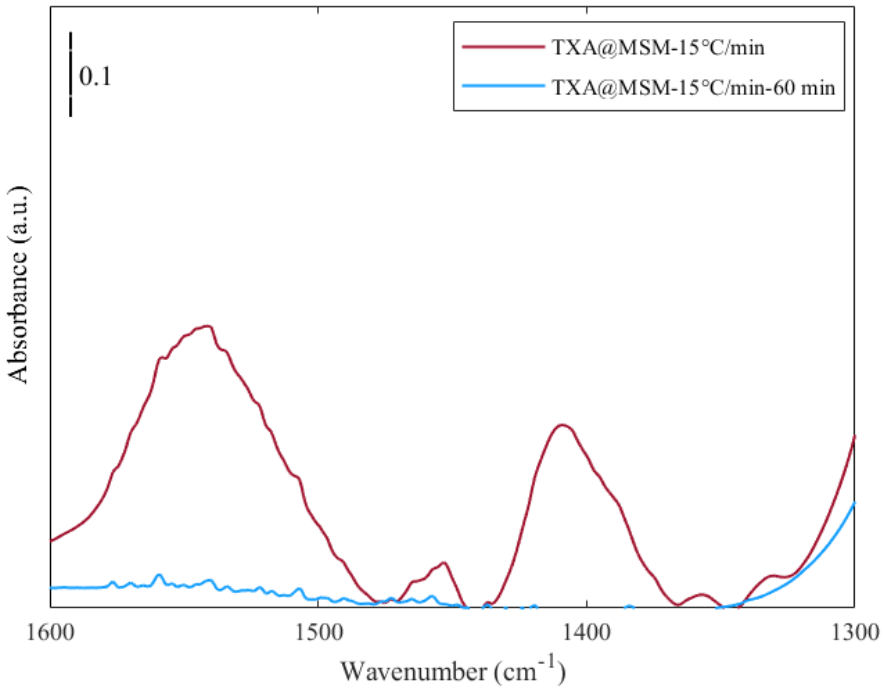

Figure 4.7 FT-IR Spectra of TXA@MSM-15°C/min before and after release test.

To further confirm this behavior, a UV-Vis analysis was carried out on the release solution. Figure 4.8 shows the release profile of TXA. Almost 70 % of the loaded TXA was released during the first 30 minutes and the released amount did not increase between 30 minutes and 1 hour. This result indicates a non-complete desorption of TXA after 60 minutes, which appears in contrast with evidence gained from the FT-IR analysis. This is ascribed to some uncertainty in the UV-vis analysis method due to the derivatization reaction.

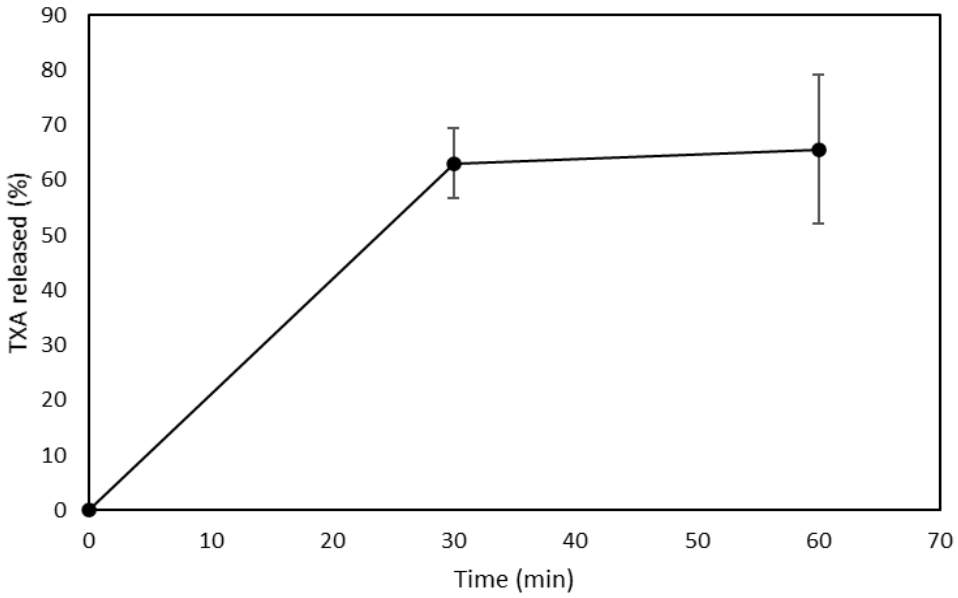

Figure 4.8 Release profile of TXA@MSM-15°C/min. Data are represented as mean ± SD (n=3).

In conclusion, the preliminary *in vitro* release test shows that MSM-15°C/min could be considered a good candidate for TXA delivery as they are able to release the drug in a rapid manner, which is suitable for its use for the management of bleeding in first aid situations.

4.4 Conclusions

A novel hemostatic material which combines the hemostatic ability of mesoporous silica with the antifibrinolytic activity of tranexamic acid, to be used for the control of hemorrhages in emergency, has been obtained. MSM (with particle sizes ranging from 1 μm to 5 μm and an average pore diameter of 25 nm) were for the first time loaded with TXA (with a final content of 4.7 %w/w) through incipient wetness impregnation technique by using water as a solvent. The XRD analysis revealed that TXA was distributed inside MSM in a non-crystalline form. The FT-IR analysis showed that TXA molecules were dispersed on the mesopore silica surface in the zwitterionic form. A CBT test performed on both unimpregnated and impregnated MSM indicated that both systems were able to activate the coagulation cascade. The preliminary in *vitro* release of TXA showed that the material was able to deliver

TXA to the release medium within one hour, as desired on the basis of CRASH-2 (Clinical Randomization of an Antifibrinolytic in Significant Hemorrhages-2) trial in order to achieve maximum efficiency.

Based on the above results, it can be concluded that the proposed systems are quite promising for the development of new hemostats for bleeding control in emergency situations.

4.5 References

1. McCormack, P. L. Tranexamic Acid: A review of its use in the treatment of hyperfibrinolysis. *Drugs* **72**, 585–617 (2012).

2. Tranexamic acid. https://pubchem.ncbi.nlm.nih.gov/compound/Tranexamic-acid.

3. Olldashi, F. *et al.* Effects of tranexamic acid on death, vascular occlusive events, and blood transfusion in trauma patients with significant haemorrhage (CRASH-2): A randomised, placebo-controlled trial. *Lancet* **376**, 23–32 (2010).

4. Sarda, S. *et al.* Adsorption of tranexamic acid on hydroxyapatite: Toward the development of biomaterials with local hemostatic activity. *Mater. Sci. Eng. C* **66**, 1–7 (2016).

5. A. Machekposhti, S., Soltani, M., Najafizadeh, P., Ebrahimi, S. A. & Chen, P. Biocompatible polymer microneedle for topical/dermal delivery of tranexamic acid. *J. Control. Release* **261**, 87–92 (2017).

6. Vijayakumar, A., Baskaran, R. & Yoo, B. K. Skin permeation and retention of topical bead formulation containing tranexamic acid. *J. Cosmet. Laser Ther.* **19**, 68–74 (2017).

7. Zhong, Q. K. *et al.* Preparation and properties of carboxymethyl chitosan/alginate/tranexamic acid composite films. *Membranes (Basel).* **9**, 11 (2019).

8. Catanzano, O., D'Esposito, V., Formisano, P., Boateng, J. S. & Quaglia, F. Composite Alginate-Hyaluronan Sponges for the Delivery of Tranexamic Acid in Postextractive Alveolar Wounds. *J. Pharm. Sci.* **107**, 654–661 (2018).

9. Li, D., Li, P., Zang, J. & Liu, J. Enhanced hemostatic performance of tranexamic acid-loaded chitosan/alginate composite microparticles. *J. Biomed. Biotechnol.* **2012**, 981321 (2012).

10. Wyrwa, R. *et al.* Electrospun mucosal wound dressings containing styptics

for bleeding control. *Mater. Sci. Eng. C* **93**, 419–428 (2018).

11. Bhattacharya, S. S. *et al.* Tranexamic acid loaded gellan gum-based polymeric microbeads for controlled release: In vitro and in vivo assessment. *Colloids Surfaces B Biointerfaces* **112**, 483–491 (2013).

12. Su, H., Wei, S., Chen, F., Cui, R. & Liu, C. Tranexamic acid-loaded starch hemostatic microspheres. *RSC Adv.* **9**, 6245–6253 (2019).

13. Sasmal, P. & Datta, P. Tranexamic acid-loaded chitosan electrospun nanofibers as drug delivery system for hemorrhage control applications. *J. Drug Deliv. Sci. Technol.* **52**, 559–567 (2019).

14. Trzeciak, K., Chotera-ouda, A., Bak-sypien, I. I. & Potrzebowski, M. J. Mesoporous silica particles as drug delivery systems—the state of the art in loading methods and the recent progress in analytical techniques for monitoring these processes. *Pharmaceutics* **13**, 950 (2021).

15. Seljak, K. B., Kocbek, P. & Gašperlin, M. Mesoporous silica nanoparticles as delivery carriers: An overview of drug loading techniques. *J. Drug Deliv. Sci. Technol.* **59**, 101906 (2020).

16. Saporito, F. *et al.* Freeze dried chitosan acetate dressings with glycosaminoglycans and traxenamic acid. *Carbohydr. Polym.* **184**, 408–417 (2018).

17. Ansari, T. M., Raza, A. & Rehman, A. U. Spectrophotometric determination of tranexamic acid in pharmaceutical bulk and dosage forms. *Anal. Sci.* **21**, 1133–1135 (2005).

18. Jadhav, S. A., Miletto, I., Brunella, V., Scalarone, D. & Berlier, G. Porous Silica Particles : Synthesis , Physicochemical Characterization and Evaluation of Suspension Stability. *Phys. Chem. An Indian J.* 1–11 (2017).

19. Socrates, G. *Infrared and Raman characteristic group frequencies. Tables and charts*. *Journal of Raman Spectroscopy* (2001).

20. Shaikh, T. *et al.* Tranexamic acid derived gold nanoparticles modified glassy carbon electrode as sensitive sensor for determination of nalbuphine. *Sensors Actuators B Chem.* **211**, 359–369 (2015).

21. Muthu, S. & Prabhakaran, A. Vibrational spectroscopic study and NBO analysis on tranexamic acid using DFT method. *Spectrochim. Acta - Part A Mol. Biomol. Spectrosc.* **129**, 184–192 (2014).

22. Meng, M., Stievano, L. & Lambert, J. F. Adsorption and thermal condensation mechanisms of amino acids on oxide supports. 1. Glycine on silica. *Langmuir* **20**, 914–923 (2004).

PART II

Chapter 5
Adsorption of arginine on mesoporous silicas

5.1 Introduction

Amino acids (AAs) are the fundamental building blocks of body proteins, and they serve as the nitrogenous backbones for many compounds such as neurotransmitters and hormones. From a chemical point of view, amino acids are organic molecules that contain a basic amino group (-NH_2), a carboxylic acid (-COOH) functional group (from here the name amino acid), and an organic variable side chain group (R-group), which determines the unique properties of each amino acid [1]. AAs are widely used in the food industry as nutritional supplements and ingredients in parenteral solutions, as well as building blocks for the production of pharmaceutical and agrochemical compounds [2,3].

To make them useful in the above-mentioned fields, AAs generally need to be placed in the form of well-ordered layers on the surface of a solid through adsorption [4]. In the last decades, the adsorption of AAs on the surface of metals or oxides has attracted a lot of attention since it is of great importance for various applications, such as solid-phase peptide synthesis, development of organic mass spectrometry, medical implants, and biomedical sensors. Besides that, the study of peptide bond formation mechanism and chain elongation on silica, alumina, or clay may contribute to a better understanding of the prebiotic chemical evolution. In fact, the above cited materials were abundant on the prebiotic earth crust after the formation of the hydrosphere and may have played an important role in the process of chemical evolution [3]. Furthermore, AAs are also interesting as model adsorbates

owing to their molecular size and zwitterionic nature [2]. In this context, the adsorption of AAs on the surface of different materials such as mesoporous carbon [5], zeolite [6], hydroxyapatite [7], zirconium phosphate [8], and silica [9] has been investigated in the literature.

Among the different materials, mesoporous silicas have been studied as adsorbents for AAs as their unique chemical and physical properties make them suitable for such application. Besides that, mesoporous silicas have many silanol groups, which could interact with the functional groups of amino acids in different ways (i.e. H-bonding and electrostatic interactions) [10,11]. In the literature, various researchers investigated the adsorption of amino acids from solutions with different pH values on MS particles. O'*Connor et al.* [2] studied the adsorption of lysin, a divalent basic amino acid, onto MCM-41 under different solution conditions. They found that the extent of the adsorption process depended on the pH and ionic strength of the adsorbate solution. This was due to a combination of ion exchange and electrostatic interactions, which both govern the adsorption process. *Vinu et al.* [12] investigated the adsorption of L-histidine (His) over various porous adsorbents such as CMK-3, SBA-15, and activated carbon. The results of their study indicated that His adsorption was pH dependent, and the maximum adsorption was achieved near the isoelectric point of the amino acid (pI = 7.59). In particular, CMK-3 adsorbed a larger amount of His with respect to the other materials. The different adsorption capacity was ascribed to stronger hydrophobic interactions between the non-polar side chains of the amino acids and the hydrophobic surface of the mesoporous carbon when compared to mesoporous silica. Similar results were obtained by *Goscianska et al.* [10] who studied the adsorption of l-phenylalanine onto ordered mesoporous silicas such as SBA-3, SBA-15, SBA-16 and KIT-6. The authors observed that the maximum sorption capacity was obtained at pH 5.6, which is close to the isoelectric point of l-phenylalanine (pI = 5.48). Moreover, the adsorption capacities of the different ordered silica samples decreased in the following order: KIT-6 > SBA-15 > SBA-16 > SBA-3. The lowest sorption capacity was found for SBA-3 may be due to that fact that part of its pores can be inaccessible to l-phenylalanine molecules. *Gao et al.* [11] studied the adsorption of five amino acids on a SBA-15-type mesoporous materials. The results of their study showed that for both acidic and basic amino acids the adsorption on SBA-15 was mainly driven by electrostatic interactions. On the other hand, the adsorption of neutral amino acids was mainly driven by hydrophobic interactions, and thus their

adsorption amounts could be enhanced by improving the hydrophobicity of the mesoporous materials.

Since a part of this PhD activity aimed at investigating the use of MS as a carrier for ARG for future wound healing applications, the present chapter provides an overview on ARG and on its role in wound healing. Moreover, the chapter also focuses on the adsorption of ARG on MS.

5.2 Arginine

2-amino-5-guanidinovaleric acid, also known as L-arginine (ARG), is a natural amino acid present in the proteins of mammalians and all life forms. It was first isolated in 1886 by *E. Schulze* and *E. Steiger*. ARG presents an amino group (-NH_2), a carboxylic acid group (-COOH) and a guanidine group ($H_2NC(=NH)NH_2$) in its side chain (figure 5.1), which confers basic properties to the amino acid [13]. ARG has an important role in several cellular processes, which include protein synthesis, cell proliferation, vasodilation, immunity, and wound healing. Moreover, it acts as a precursor for the synthesis of several biomolecules such as nitric oxide, urea, ornithine, proline, creatine phosphate and polyamines, which have pharmacologic effects on multiple systems in the body and, specifically, on wound healing [14,15].

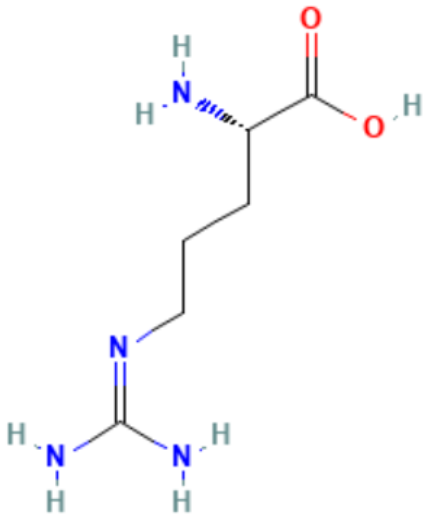

Figure 5.1 The chemical structure of L-arginine (ARG) [16].

The importance of ARG on wound healing was first noted by *Seifter et al.* in 1978 [17]. ARG and its metabolites have been recognized as important mediators for tissue repair of acute and chronic wounds. In wound healing, ARG is mainly metabolized through two different pathways (figure 5.2): the arginine-NO pathway and the arginine-arginase pathway. Both pathways act in a sequential manner. During the early phase of the wound healing process, ARG is converted into nitric oxide (NO) and citrulline via the arginine-NO pathway by the action of NOS. NO is a free radical which plays an essential role in the different phases of the wound healing process. As a radical, it acts as a protective agent by creating a cytotoxic wound environment for pathogens in order to maintain a sterile wound space. In addition, NO increases the blood flow to the wound site and stimulates the proliferation of endothelial cells and the re-epithelialization. It also enhances the angiogenesis and the collagen deposition at the wound site and affects wound contraction. In the second pathway, which occurs after 72 hours of the beginning of the process, ARG is converted into ornithine by the arginase I and II enzymes. Ornithine is the precursor polyamines and proline, molecules involved in the wound healing process. Proline is an important amino acid for the synthesis of collagen, a major component that acts as a matrix to promote cell growth and differentiation. On the other hand, polyamines are important for blood vessel formation [15,18].

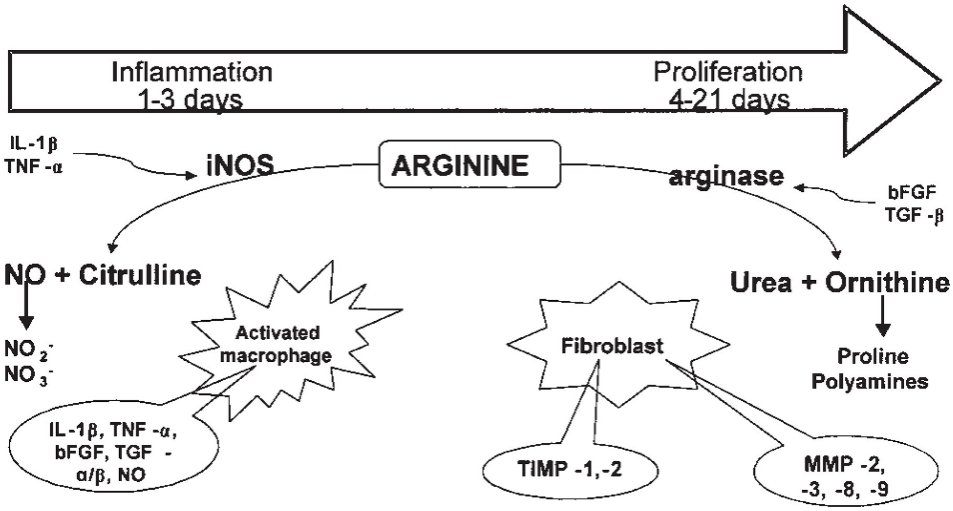

Figure 5.2 Arginine metabolism in wounds [15].

ARG is classified as a semi-essential or conditionally essential amino acid for adults as it can be synthesized by the body in sufficient amount to meet the physiological needs. However, under certain conditions such as children growth, stress, pregnancy, and wound healing, the body could not provide an adequate amount of ARG to satisfy all the metabolic needs, making ARG supplementation essential for wound treatment [13,15].

Table 5.1 reports an overview of different studies that show the benefits of ARG supplementation during wound healing.

Table 5.2 Summary of studies showing the effect of arginine supplementation on wound-healing [15].

Reports	Samples and model	Supplemental arginine	Combined with other therapies on wound healing	Effect of arginine supplementation			
				Healing rate	Collagen formation	Wound breaking	Remark
Maria B. Witte *et al.*, 2002	Diabetic Sprague-Dawley rats	1 g kg^{-1} twice daily	Polyvinyl alcohol (PVA) sponges		Improved	Enhanced	NO pathway
Han Ping Shi *et al.*, 2007	Lewis rats under trauma/hemorrhagic shock	1 g kg^{-1} d^{-1}	PVA sponges		Improved 40%	Enhanced 29%	
S. Brewer *et al.*, 2010	Spinal-cord-injured patients	9 g d^{-1}		Improved			
Xiao-jun Zhang *et al.*, 2011	New Zealand white rabbits	1.24 g kg^{-1} d^{-1}					Increased DNA synthesis
Kouji Masumoto *et al.*, 2011	Pediatric patients with wound dehiscence caused by surgical site infection	100 to 150 mg kg^{-1} d^{-1}	Negative pressure wound therapy	Improved			Decreased the infection
Brooke R. Chapman *et al.*, 2011	Pressure ulcers in patients with spinal cord injuries	9 g d^{-1}	Additional protein, zinc and vitamin C	2.5-Fold greater rate of healing			
B. Leigh *et al.*, 2012	Inpatients with pressure ulcers	9 g d^{-1}		2-Fold improvement			Decrease in pressure ulcer severity
Lori A. Coburn *et al.*, 2012	$NOS^{-/-}$ C57BL/6 mice with dextran sulfate sodium colitis			Improved			Improved colon weight and reduced colonic permeability and inflammatory reaction
D. A. De Luis *et al.*, 2015	Postsurgical cancer patients	18.9 g per d^{-1}		Improved			Decreased length of hospital stay and fistula wound complications
Ferhan Yaman *et al.*, 2016	Rats with a calvarial defect	1.81 g kg^{-1} of arginine	Silicate inositol complex (arginine 49.5%, silicon 8.2%, and inositol 25%)				Improved bone tissue healing

Various studies demonstrated the beneficial effect of ARG on the healing of both acute and chronic wounds in animals as well as in humans[19–23]. *Varedi et al.* [19] studied the effect of local administration of ARG on the healing of cutaneous excisional wounds in rats. The results of their study indicated that wounds treated with ARG showed an increase in the rate of wound closure. Regarding the influence of ARG on the treatment of chronic wounds, *Shi et al.* [20] studied the effect of ARG supplementation on the healing of diabetic wounds and showed that ARG could improve both normal and diabetic wound healing. In another study, the contribution of the oral or topical route of administration of ARG in a surgical wound healing process was evaluated by *Jerônimo et al.* [21]. The authors suggested that either the oral or the topical administration of ARG could be considered an important factor in restoring the tissue integrity after injury. Moreover, the topically applied ARG seemed to be more effective in accelerating the wound healing process.

As mentioned earlier, ARG is involved in different phases of the healing process and its concentration could significantly decrease in the wound site as it is rapidly metabolized by NOS and arginase enzymes. Low ARG levels limit the NO production so hindering the formation of new tissues and consequently wound healing [18]. Furthermore, the half-life of NO is extremely short (0.009 to 2 seconds)

[24]. Therefore, the exogenous administration of ARG becomes necessary to compensate its deficiency at the wound site. To obtain an enhanced therapeutic effect, a controlled release of ARG is required in order to avoid its rapid metabolism and an excessive synthesis of NO, which could impair the healing process [25]. One approach is based on the use of suitable carriers for the delivery of ARG. These arginine-loaded systems represent a good strategy since they can supplement ARG in situ and control its release in the wound site.

Many studies suggested the use of nano-systems based on lipids, polymers, and inorganic materials for the delivery of ARG for different applications. *Yazdani-Arazi et al.* [26] studied the encapsulation of ARG into a nanostructured lipidic carrier (NLC) for the treatment of alopecia, showing that topically applied ARG-loaded NLC had a more efficient performance than an ARG aqueous solution. *Kim et al.* [27] studied the formulation of ARG loaded biodegradable poly(lactide-co-glycolide) nanospheres as a local sustained delivery system for the prevention of restenosis, showing that the ARG release was sustained and reduced vascular smooth cell proliferation.

As far as wound healing applications are concerned, *Matsumoto et al.* [28] investigated the effect of wound dressings composed of Hyaluronic acid and ARG on wound healing. Different spongy sheets, which were based on high-molecular-weight hyaluronic acid (HMWHA), were prepared and then immersed in an aqueous low-molecular-weight HA solution without or with different amounts of ARG. The final materials were divided into five groups: the HMWHA (group I), the HMWHA/LMWHA (group II) and the HMWHA/LMWHA/ARG (group III-group V). *In vivo* tests performed on a surgical wound showed that all sheets improved wound healing when compared to the control (commercial polyurethane film dressing). This suggests that both HA and ARG are essential for a fast and successful healing process (figure 5.3).

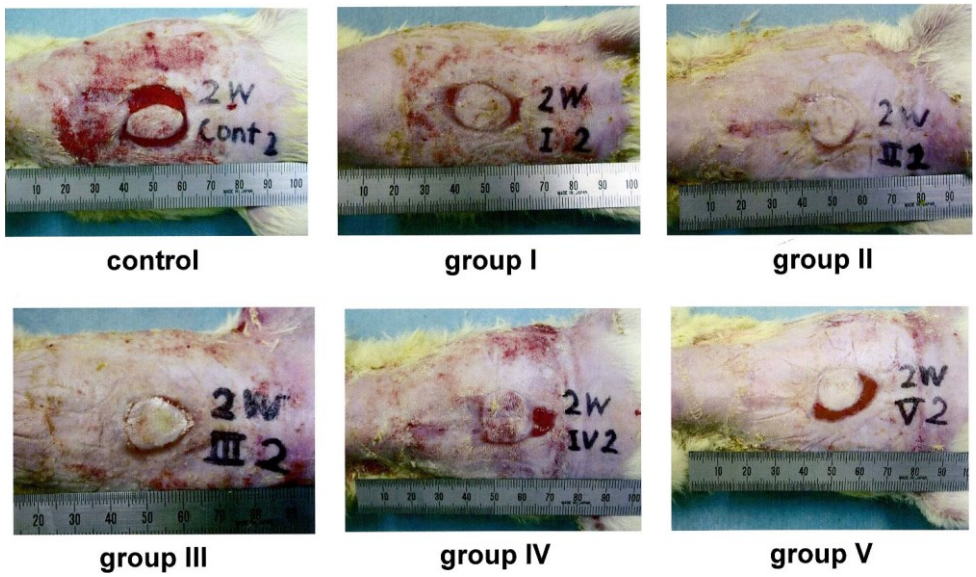

Figure 5.3 Macroscopic appearance of the surgical wound surface after 2 weeks [28].

In another work, *Reesi et al.* developed a gel, which was based on lignin nanofibers (lig-NFs) and modified with ARG molecules via electrostatic interaction, for the treatment of both acute and chronic wounds. The results of the study suggested that the gel could be a good candidate for the treatment of wounds as it can sustain the release of ARG, accelerate wound closure and increase re-epithelialization, collagen deposition, and angiogenesis (figure 5.4) [29].

(a)

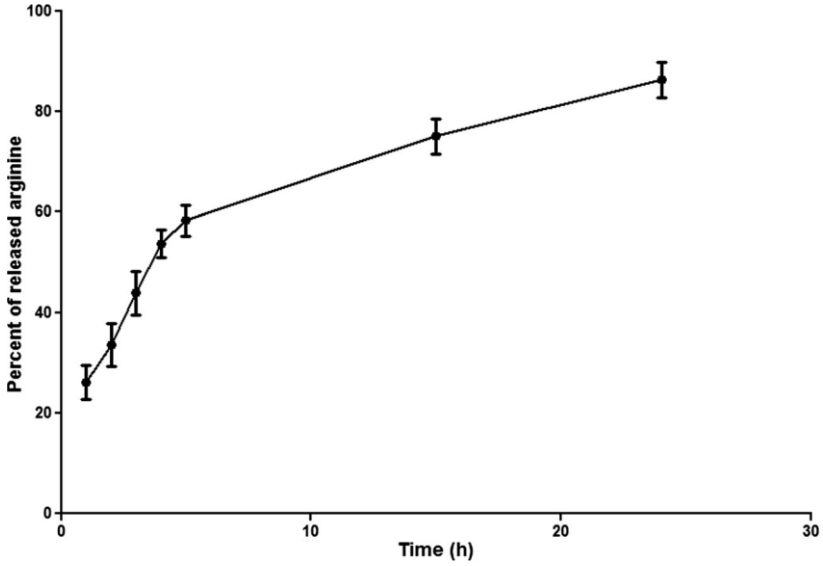

(b)

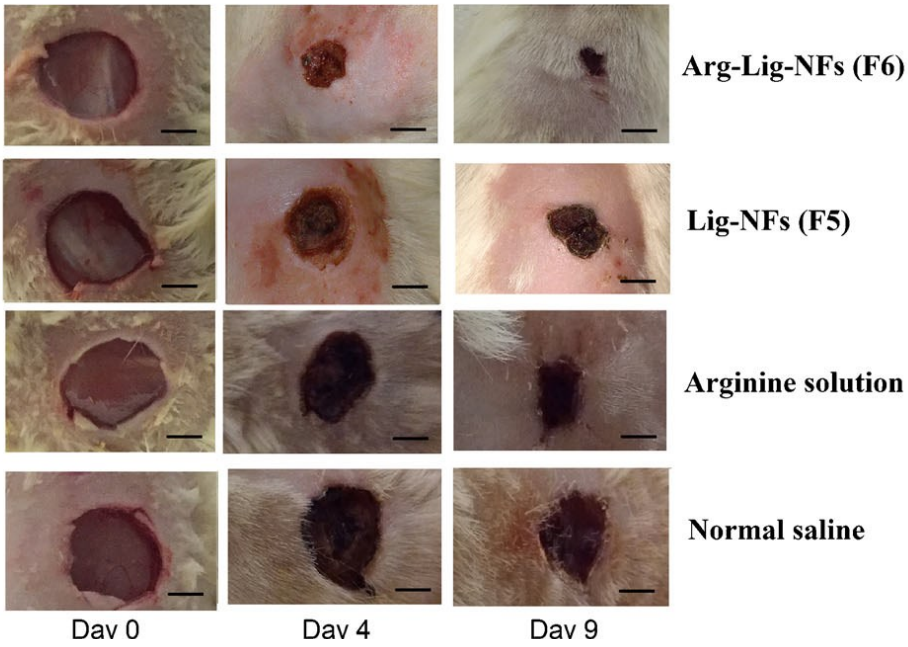

Figure 5.4 The release profile of arginine from Arg-Lig-NF (F5) gel in phosphate buffer pH 7.4 (a) and (b) Photographs of macroscopic appearance of wounds treated with Arg-Lig-NF gel (F6), Lig-NF gel (F5), arginine solution, and normal saline; on the surgery day (0), 4 and 9 days [29].

In a recent work, *Shikida et al.* [30] prepared arginine-conjugated chitosan nanoparticles (CHITARG) and loaded them with ARG, to achieve a system that combines the antimicrobial properties of the matrix and may sustain the release of ARG. The *in vitro* release profile showed an initial burst release of ARG after the first 2 h, which was ascribed to the release of the amino acid molecules adsorbed on the nanoparticles surface. This was followed by a slow and constant release, probably related to the encapsulation of ARG in the form of clusters which appear to have more affinity for the matrix than for the release medium (figure 5.5).

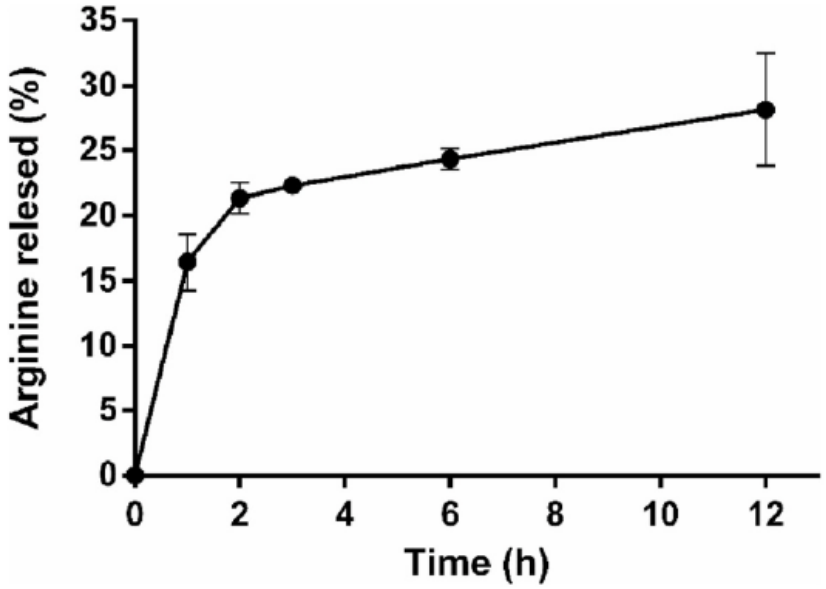

Figure 5.5 ARG in vitro release profile from ARG-loaded CHITARG [30].

5.3 The adsorption of arginine on mesoporous silica

Only a few studies can be found the literature on the adsorption of ARG on silica. *Vlasova et al.* [31] studied the interaction of ARG with the surface of highly dispersed silica particles in an aqueous suspension. Considering that when the pH of the solvent medium is varied ARG may present different forms (cations, zwitterions or anions, figure 5.6a), the adsorption of ARG on the surface of silica was performed at different pH values (in the 2-8 range). The result of the adsorption study showed that the adsorption of ARG began at pH > 5, and it increased with the pH value. The largest extent of ARG adsorption was observed at pH ≈ 8. Moreover, after the addition of a background electrolyte (i.e. a 0.01 M or a 0.1 M NaCl aqueous solution) the adsorption of ARG decreased significantly (figure 5.6b). The authors suggested that the formation of a complex between the silanol groups of the silica surface and ARG was driven by electrostatic interaction. In fact, at pH > 5 the amount of negatively charged SiO^- groups on the silica surface increase and a lot of ARG particles with a positive charge can be found in the water suspension. Therefore, electrostatic interactions between the dissociated silanols and ARG

molecules are favored so resulting in an increased adsorption of ARG on the silica surface.

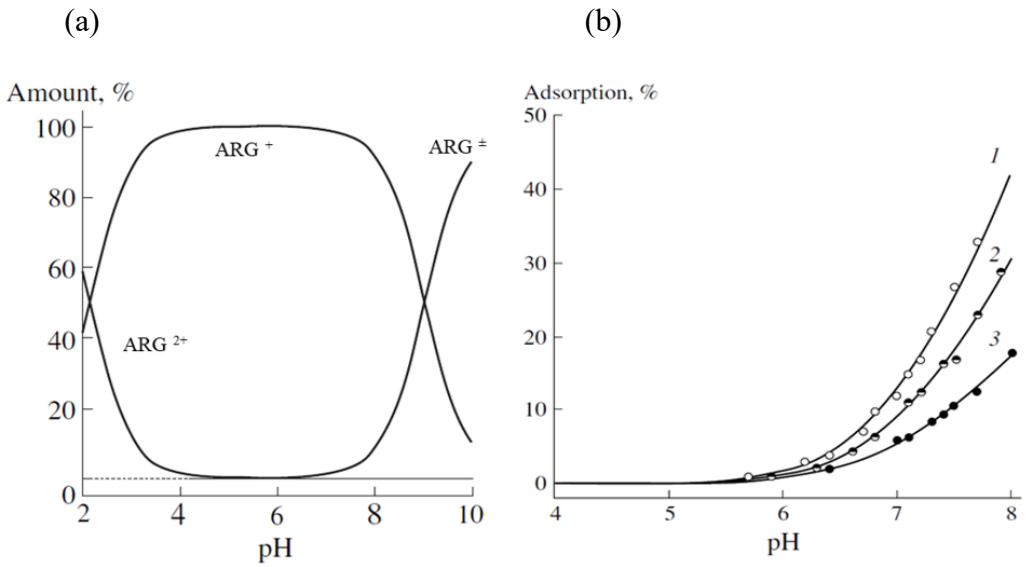

Figure 5.6 (a) Distribution of different protonated forms of ARG, and (b) adsorption of ARG on the surface of highly dispersed silica from (*1*) water, (*2*) 0.01 and (*3*) 0.1 M NaCl solutions [31].

A similar result was found by *Gao et al.* [11]. In their work, the adsorption behavior of ARG on SBA-15-type mesoporous materials was investigated in aqueous solutions with adjustable amino acid concentration, ion strength, and pH to understand the main interaction between ARG and the silica surface. The results of the study showed that the amount of adsorbed ARG monotonously increased throughout the investigated pH range (figure 5.7a). At pH < 2.5, the adsorption amount of ARG was negligible because both ARG and the surface of SBA-15 were all positively charged. However, by increasing pH, the adsorption amount of ARG quickly increased because while ARG was still positively charged the SBA-15 surface became more and more negatively charged. Based on these observations, the authors concluded that the adsorption of ARG was mainly driven by electrostatic forces. To investigate the influence of the ionic strength of the solution on adsorption, a set of experiments was performed at pH 10 by gradually increasing the concentration of NaCl. The results of the experiment indicated that the amount of adsorbed ARG strongly decreased when the concentration of NaCl was increased

(figure 5.7b). The poor adsorption of ARG was ascribed to the electrostatic shielding of Na^+ ions towards the charged SBA-15 surface. This result further confirms that the electrostatic interactions have an important role in the adsorption of ARG on silica surface.

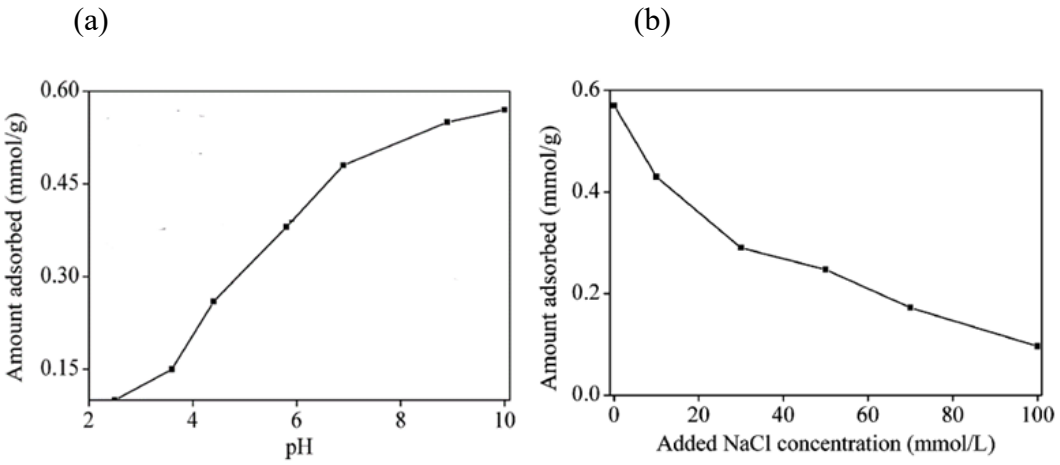

Figure 5.7 (a) Adsorption amounts of ARG on SBA-15 at different pH, and (b) ARG adsorption on SBA-15 at pH 10 with different added NaCl concentrations [11].

In another work, *Solanki et al.* [32] reported the encapsulation of different amounts of ARG into MCM-48 by incipient wetness impregnation and investigated its release behavior in simulated body fluids under different pH conditions (pH 1.2 and pH 7.4). The study showed that at pH 1.2 the release of ARG was slow while at pH 7.4 the release was fast (figure 5.8).

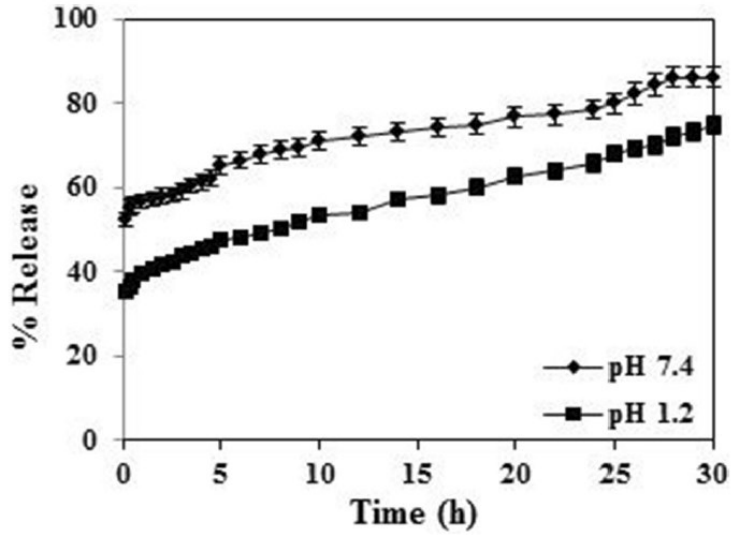

Figure 5.8 The release profile of ARG/MCM-48 at pH 1.2 and 7.4 [32].

Similar results were obtained for the release of ARG from an MCM-41 support functionalized with Tungstophosphoric acid, under different pH condition (pH 2 and pH 7.4). It has been found that the release of ARG was pH dependent. In acidic conditions the release of ARG was slow while at pH 7.4 the release was fast (figure 5.9) [33].

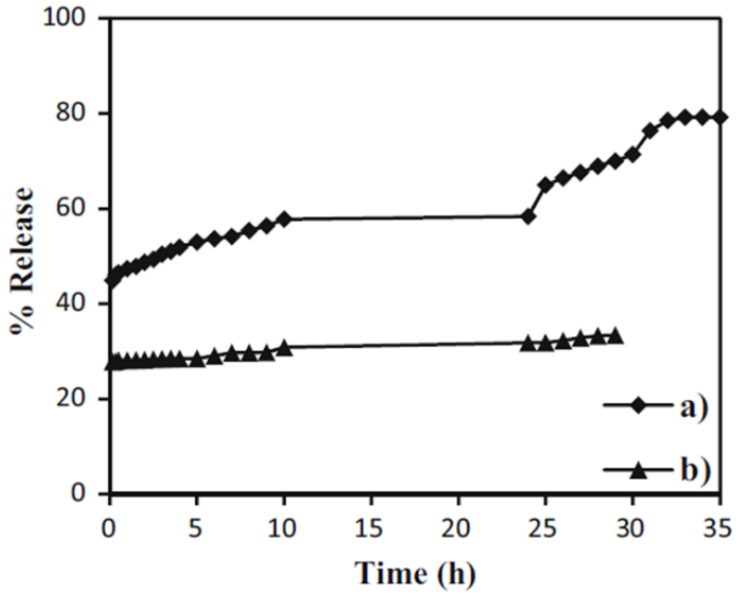

Figure 5.9 The release profile of ARG/TPA-MCM-41 (a) at pH 7.4 and (b) pH 2 [32].

5.4 Conclusions

This chapter has dealt with a brief overview of the role of arginine in wound healing and the adsorption of this amino acid on mesoporous silica-based materials. Moreover, data concerning the release of arginine from mesoporous silica-based materials have been also summarized.

It has been found that the extent of adsorption of amino acids depends mainly depends on the pH of the adsorbate solution probably due to electrostatic interactions governing the adsorption process. Moreover, several studies suggested that the maximum degree of adsorption of amino acids on mesoporous silicas is achieved at a pH near their isoelectric point. Indeed, as far as ARG adsorption is concerned, it emerged that the maximum amount was obtained at a pH of about 11.

Concerning the release of ARG, it has been found that its release rate depends on the pH of the receiving medium. In acidic conditions (pH ≈1.2) the release of ARG was reported to be slower than in conditions close to neutrality (pH ≈7.4).

From the analysis of the literature, it has appeared that although several research studies have been conducted with the purpose of understanding the mechanisms involved in the adsorption of ARG from aqueous solution onto silica particles, no specific studies have been conducted to investigate the stability of these carriers during or after the loading process. In order to fill this gap, the following chapters of this PhD dissertation are devoted to understand how the impregnation process may affect the structure of two different types of mesoporous silica particles.

5.5 References

1. Lopez MJ, M. S. Biochemistry, Essential Amino Acids. . In: StatPearls [Internet]. Treasure Island (FL): StatPearls Publishing; 2021 Jan. Available from: https://www.ncbi.nlm.nih.gov/books/NBK557845/.
2. O'Connor, A. J. *et al.* Amino acid adsorption onto mesoporous silica molecular sieves. *Sep. Purif. Technol.* **48**, 197–201 (2006).
3. Meng, M., Stievano, L. & Lambert, J. F. Adsorption and thermal condensation mechanisms of amino acids on oxide supports. 1. Glycine on silica. *Langmuir* **20**, 914–923 (2004).
4. Goscianska, J., Olejnik, A. & Pietrzak, R. Comparison of ordered mesoporous materials sorption properties towards amino acids. *Adsorption* **19**, 581–588 (2013).
5. Vinu, A., Hossain, K. Z., Satish Kumar, G. & Ariga, K. Adsorption of l-histidine over mesoporous carbon molecular sieves. *Carbon N. Y.* **44**, 530–536 (2006).
6. Munsch, S., Hartmann, M. & Ernst, S. Adsorption and separation of amino acids from aqueous solutions on zeolites. *Chem. Commun.* 1978–1979 (2001).
7. El Shafei, G. M. S. & Moussa, N. A. Adsorption of Some Essential Amino Acids on Hydroxyapatite. *J. Colloid Interface Sci.* **238**, 160–166 (2001).
8. El Shafei, G. M. S. Effect of Pore Structure on Surface Characteristics of Zirconium Phosphate-Modified Silica. *J. Colloid Interface Sci.* **250**, 394–399 (2002).
9. Palit, D. & Moulik, S. P. Adsorption Behaviors of l-Histidine and dl-Tryptophan on Cholesterol, Silica, Alumina, and Graphite. *J. Colloid Interface Sci.* **239**, 20–26 (2001).
10. Goscianska, J., Olejnik, A. & Pietrzak, R. Adsorption of l-phenylalanine onto mesoporous silica. *Mater. Chem. Phys.* **142**, 586–593 (2013).
11. Gao, Q. *et al.* Amino acid adsorption on mesoporous materials: Influence of types of amino acids, modification of mesoporous materials, and solution conditions. *J. Phys. Chem. B* **112**, 2261–2267 (2008).
12. Vinu, A., Hossain, K. Z., Kumar, G. S., Sivamurugan, V. & Ariga, K.

Adsorption of amino acid on mesoporous molecular sieves. *Nanoporous Mater. IV* **156**, 631–636 (2005).

13. Sudar-Milovanovic, E. *et al.* Benefits of L-Arginine on Cardiovascular System. *Rev. Med. Chem.* **16**, 94–103 (2016).

14. Gad, M. Z. Anti-aging effects of L-arginine. *J. Adv. Res.* **1**, 169–177 (2010).

15. Stechmiller, J. K., Childress, B. & Cowan, L. Arginine supplementation and wound healing. *Nutr. Clin. Pract.* **20**, 52–61 (2005).

16. https://pubchem.ncbi.nlm.nih.gov/compound/Arginine#section=Structures.

17. Seifter, E., Rettura, G., Barbul, A. & Levenson, S. M. Arginine: an essential amino acid for injured rats. *Surgery* **84**, 224–230 (1978).

18. Gould, A. N. & Candy, G. P. The Role of l-Arginine in Wound Healing. in *L-Arginine in Clinical Nutrition* 577–588 (Springer International Publishing, 2017).

19. Varedi, M., Akbari, Z., Dehghani, G. A. & Tabei, S. Z. Local Administration of L-Arginine Accelerates Wound Closure. *Iran. Journlal Basic Med. Sci.* **12**, 173–178 (2009).

20. Shi, H. P., Most, D., Efron, D. T., Witte, M. B. & Barbul, A. Supplemental L-arginine enhances wound healing in diabetic rats. *Wound Repair Regen.* **11**, 198–203 (2003).

21. Jerônimo, M. S. *et al.* Oral or topical administration of L-arginine changes the expression of TGF and iNOS and results in early wounds healing. *Acta Cir. Bras.* **31**, 586–596 (2016).

22. Frias Soriano, L. *et al.* The effectiveness of oral nutritional supplementation in the healing of pressure ulcers. *J. Wound Care* **13**, 319–322 (2004).

23. Heyman, H., Van De Looverbosch, D. E. J., Meijer, E. P. & Schols, J. M. G. A. Benefits of an oral nutritional supplement on pressure ulcer healing in long-term care. *J. Wound Care* **17**, 476–480 (2008).

24. Vong, L. B. & Nagasaki, Y. Nitric Oxide Nano-Delivery Systems for Cancer Therapeutics: Advances and Challenges. *Antioxidants* **9**, 791 (2020).

25. Park, J. E., Abrams, M. J., Efron, P. A. & Barbul, A. Excessive nitric oxide impairs wound collagen accumulation. *J. Surg. Res.* **183**, 487–492 (2013).

26. Yazdani-Arazi, S. N., Ghanbarzadeh, S., Adibkia, K., Kouhsoltani, M. &

Hamishehkar, H. Histological evaluation of follicular delivery of arginine via nanostructured lipid carriers: a novel potential approach for the treatment of alopecia. *Artif. Cells, Nanomedicine Biotechnol.* **45**, 1379–1387 (2017).

27. Kim, S. E. *et al.* Controlled Release of L-Arginine from Poly(lactide-co-glycolide) Nanoparticles for the Inhibition of Vascular Smooth Muscle Cell Proliferation. *Biomater. Res.* **4**, 85–91 (2000).

28. Matsumoto, Y., Arai, K., Momose, H. & Kuroyanagi, Y. Development of a wound dressing composed of a hyaluronic acid sponge containing arginine. *J. Biomater. Sci. Polym. Ed.* **20**, 993–1004 (2009).

29. Reesi, F., Minaiyan, M. & Taheri, A. A novel lignin-based nanofibrous dressing containing arginine for wound-healing applications. *Drug Deliv. Transl. Res.* **8**, 111–122 (2018).

30. Shikida, D. N. R., Dalmolin, L. F., Fumagalli, F., da Silva Emery, F. & Lopez, R. F. V. Arginine-conjugated chitosan nanoparticles for topical arginine release in wounds. *J. Drug Deliv. Sci. Technol.* **61**, 102115 (2021).

31. Vlasova, N. N. & Golovkova, L. P. The Adsorption of Amino Acids on the Surface of Highly Dispersed Silica. *Colloid J.* **66**, 733–738 (2004).

32. Solanki, P. & Patel, A. In vitro release of l-arginine and cysteine from MCM-48: a study on effect of size of active biomolecules on release rate. *J. Porous Mater.* **25**, 1489–1498 (2018).

33. Patel, A. & Solanki, P. 12-Tungstophosphoric acid functionalized MCM-41 : synthesis , characterization and study of controlled in vitro release of L - arginine. *J. Porous Mater.* **23**, 1113–1123 (2016).

Chapter 6
Impregnation of spherical mesoporous silica particles with l-arginine: the effect of the pH of the impregnating solutions on the stability of the carrier

Part of the information reported in this chapter has been previously published in *Mohamed et al*. **2021**, *Journal of Molecular Sciences,* 22, 13403 [1].

6.1 Introduction

The present chapter concerns the development of a system based on spherical mesoporous silica particles for the delivery of ARG for future applications in wound healing. As stated earlier, MS-based systems have gained much attention in the field of skin care and dermal drug delivery due to their compatibility with skin cells and their ability to enhance drug permeation through the skin [2]. Indeed, they have been proposed for the treatment of several skin disorders, such as skin cancer, psoriasis, acne, photoprotection, and wound healing [3]. In the field of wound healing, different scientists suggested the use of silica to manufacture more effective

dressings for the treatment of wounds. On one hand, MS could act like a drug, by releasing silicic acid which promotes wound closure. On the other hand, silica particles can act like vehicles for the delivery of therapeutic molecules for wound treatment [4,5]. Therefore, based on these considerations, the aim of this work is to develop a multifunctional material to be applied in devices for wound management, which combines the physicochemical and biological properties of MS particles with the pharmacological effect of ARG.

The loading of ARG on MS has been reported by various researchers[6–9]. However, no information regarding the stability of these carriers during or after the loading process could be found in the literature. This aspect should deserve more attention as it is known that silica-based materials could dissolve under basic pH conditions [10,11] and ARG solutions are alkaline (pH about 11) [12]. To fill this gap, the present chapter focused on the impregnation of SMSP with aqueous ARG solutions at different pHs. The main objective was to investigate the effect of the different pH of the impregnating solutions on the structure of the carrier.

6.2 Experimental

6.2.1 Synthesis of spherical mesoporous silica particles (SMSP)

SMSP were synthesized through a base-catalyzed reaction by a sol–gel process involving the use of hexadecyltrimethylammonium bromide (CTAB) as a surfactant and tetraethyl orthosilicate (TEOS) as a silica precursor, according to the procedure reported in chapter 3 (subsection 3.2.2).

6.2.2 The loading of ARG

The incorporation of ARG was performed using water as a solvent by the wet impregnation method, according to the procedure reported by *Solanki et al.* [9]. For this purpose, 200 mg of SMSP were impregnated with 2 ml of an aqueous solution of ARG (10 mg/ml) so that the nominal ARG content was about 10 % w/w. The pH of the solution was measured using pH-sensitive litmus paper and was about 11. The material was then dried at 60 °C in an oven till complete evaporation of the solvent. The achieved material was designed as ARG-11@SMSP.

The loading of ARG at different pH values was performed with the same procedure. The pH of the ARG/H_2O impregnating solutions was adjusted to the desired value (5, 9 and 10) with the addition of HCl (1 % w/w).

The obtained materials were designed as ARG-x@SMSP, where x indicates the pH value of the ARG/H_2O impregnating solution.

6.2.3 Instrumental characterization

The characterization of SMSP loaded with ARG was performed using several techniques.

Thermogravimetric analysis (TGA) was carried using a Linseis STA PT 1600 (TGA-DSC) instrument from 30 °C to 800 °C at the heating rate of 10 °C/min in air.

Nitrogen adsorption-desorption analysis was performed using a Micromeritics ASAP 2020 Plus Physisorption analyser (Micromeritics, Norcross, GA, USA). Before the adsorption measurement, ARG-x@SMSP samples were outgassed at 70 °C for 2 h. The specific surface area was calculated using the Barret-Emmett-Teller (BET) method in the relative pressure range of 0.099 - 0.179. The pore size distribution was obtained, using the Barlett-Joyner-Halenda (BJH) method, from the desorption branch of the isotherm. The total pore volume was determined at a relative pressure of about 0.93.

FESEM images were recorded with a FESEM ZEISS Merlin instrument (Oxford Instruments, Abingdon-on-Thames, UK). The samples were mounted on a metal stub with double-sided adhesive tape and coated with platinum before the analysis.

X-ray diffraction (XRD) patterns were obtained with PANalytical X'Pert diffractometer (Malvern Panalytical, Almelo, The Neatherlands) using Cu-Kα radiation (wavelength = 1.54187 Å). The data were collected from 5° to 60° (2θ) with a step size of 0.026° (2θ).

FT-IR analysis was performed using a Bruker Equinox 55 spectrometer (Bruker, Billerica, MA, USA). The FT-IR spectra of ARG-x@SMSP were obtained on self-supported pellets, prepared by pressing the powder with a hydraulic press. As far as ARG is concerned, the powder was diluted in KBr. All samples were

outgassed in high vacuum (residual pressure 0.1 Pa) at room temperature for 1 h. The spectra were obtained from 4000 cm^{-1} to 600 cm^{-1} with a resolution of 2 cm^{-1}.

6.2.4 Preliminary desorption test

A preliminary desorption test was performed by soaking the ARG-x@SMSP samples in water at 35 °C under continuous stirring. Different batches were prepared by soaking ARG-x@SMSP in water (1 mg/ml). At prefixed times (10 and 60 minutes), the samples were recovered by filtration, dried upon complete evaporation of the solvent, and analyzed for ARG content. The pH of the solutions was measured before the analysis and no modifications was observed due to the ARG desorption.

To estimate the ARG content, samples recovered from the desorption test (ARG-x@SMSP-ymin, where y indicates the time at which the powder was collected) were analyzed by FT-IR spectroscopy. The achieved spectra were compared with those of the ARG-x@SMSP samples, which allowed a semi-quantitative analysis of the ARG content in the samples to be carried out. The comparison was based on the detection of the most intense absorption band of ARG, at 1670 cm^{-1}, which corresponds to the stretching vibration of the guanidine group. To estimate the amount of ARG inside the samples, the height of the band at 1670 cm^{-1} was measured before and after desorption. Considering that before desorption 100 % ARG is present inside the carrier, the percentage of ARG still present in the carriers at different desorption times was estimated through a proportion ($H_{ARG\text{-}x@SMSP\text{-}ymin} : H_{ARG\text{-}x@SMSP} = M : 100$, where H is the height of the band and M is the ARG amount). For a better comparison, the FT-IR spectra were normalized with respect to the intensity of the bands at 2000 cm^{-1} and 1860 cm^{-1}, which relate to the vibrational modes of SiO_4 tetrahedra present in the silica structure. After the amount ARG still present in the samples was evaluated, the amount of desorbed ARG was simply deduced from the complement to 100 %.

6.3 Results and Discussion

6.3.1 Characterization of ARG-11@SMSP

The characterization of the SMSP after the loading of ARG, which was conducted by means of TGA, nitrogen sorption analysis, FESEM, XRD, and Fourier Transform Infrared Spectroscopy, is discussed in the present section.

A TGA was performed on the SMSP before impregnation and on the ARG-11@SMSP sample (figure 6.1). SMSP shows an initial weight loss of 8.2 % up to 150 °C, which can be assigned to the loss of water physically adsorbed on the material surface. The gradual and small weight loss observed at temperatures higher than 200 °C (about 2.6 %) could be ascribed to surface dihydroxylation [13]. The TGA curve of ARG-11@SMSP shows an initial weight loss of about 7.1 % due to the removal of adsorbed water. Further weight loss is observed from 200 °C to 800 °C, which can be ascribed to ARG removal. The ARG content in the ARG-11@SMSP sample was determined from the weight loss between 200°C and 800°C after subtracting the weight loss measured in the same temperature range for the unimpregnated SMSP. The measured ARG content in the ARG-11@SMSP sample resulted to be about 9.1 % w/w, which can be considered in good agreement with its nominal content (10% w/w).

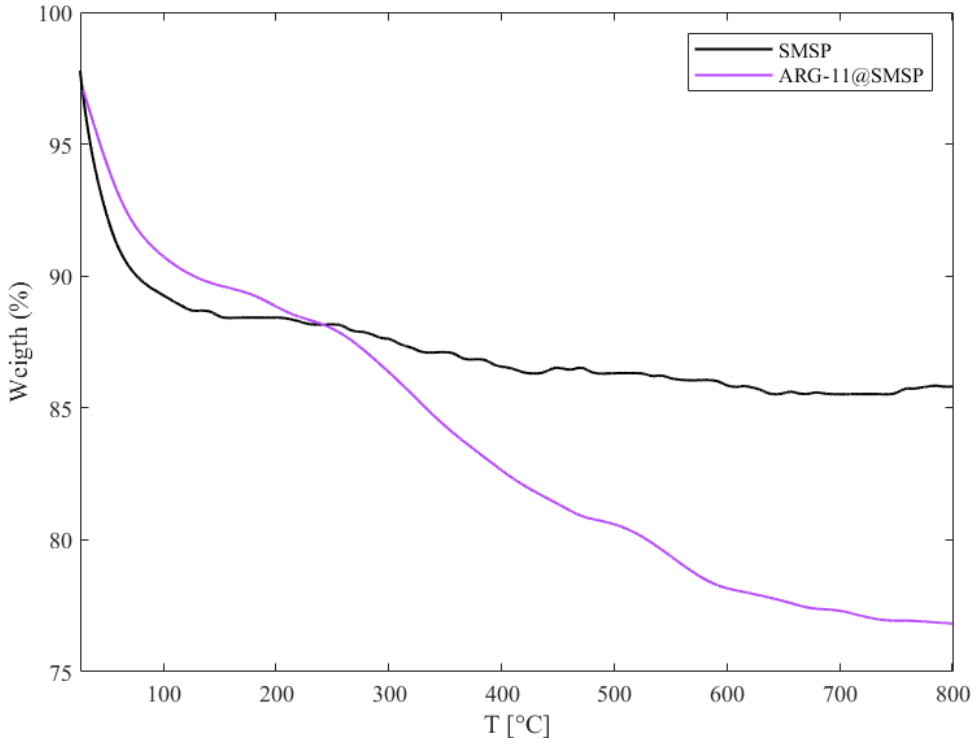

Figure 6.1 The TGA curves of SMSP (black curve) and ARG-11@SMSP (purple curve).

Figure 6.2 shows the nitrogen adsorption-desorption isotherms and pore size distributions of SMSP before and after the ARG loading at pH≈11 (ARG-11@SMSP). The values of the SSA_{BET} and pore volume are summarized in table 6.1. As far as sample ARG-11@SMSP is concerned, the isotherm (figure 6.2a) presents a type H2 hysteresis loop at relative pressures p/p^0 above 0.4, which is characteristic of materials with disordered porosity and ink-bottle pores [14]. A significant change can also be observed in the pore size distribution (figure 6.2b) when compared to SMSP as such. After impregnation the original family of pores with a diameter of 2.4 nm dramatically decreased in volume and its average pore size shifted to 2.0 nm, Moreover, a new family of larger pore with an average diameter of about 3.6 nm appeared. These changes suggest that the exposure to an alkaline solution (i.e., the ARG solution at pH 11) during the impregnation process had a remarkable effect on the textural properties of the carrier.

(a)

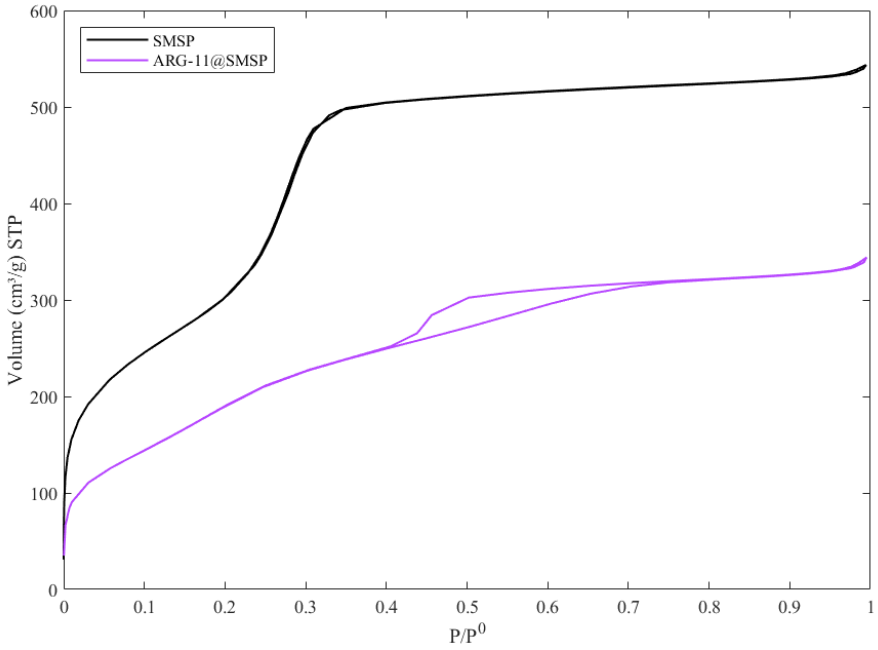

(b)

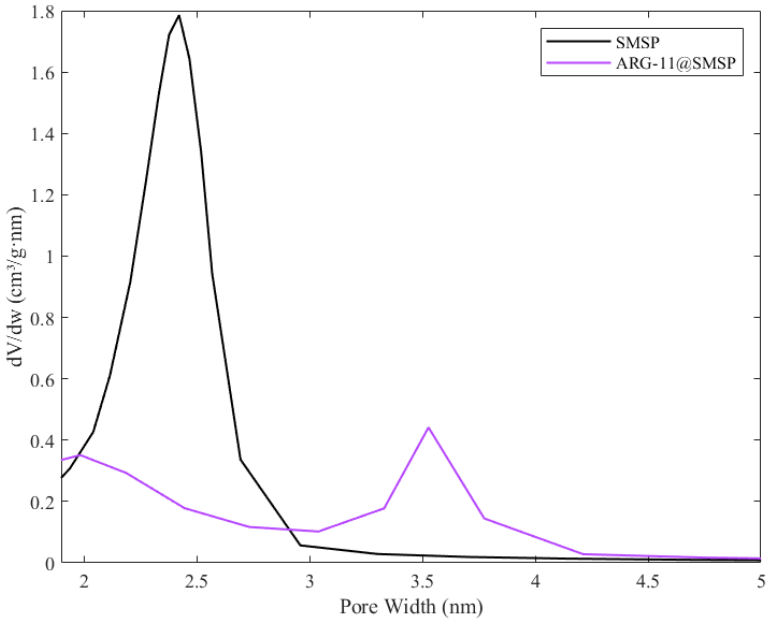

Figure 6.2 (a) The nitrogen adsorption-desorption isotherms and (b) The PSD of SMSP (black curve) and ARG-11@SMSP (purple curve).

A similar effect was previously observed for different silica-based materials after treatment with basic solutions or after immersion in aqueous media [15–18]. According to the authors, the variation of porosity was caused by the dissolution of the silica walls between the pores (figure 6.3), which led to the formation of larger pores and the generation of soluble silica species that redeposited on the material so resulting in a decrease of the diameter of the pores [15–18].

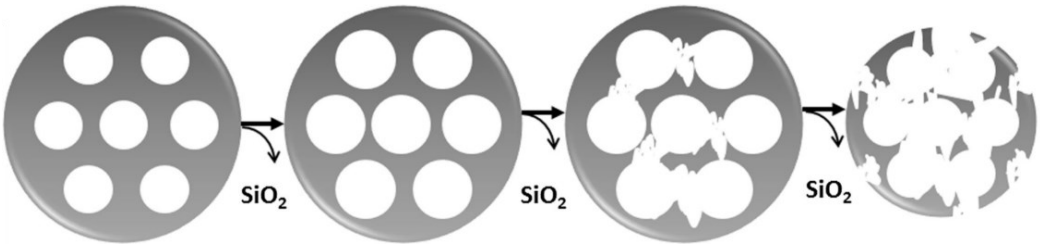

Figure 6.3 Schematic representation of the dissolution process of MSP in aqueous solution [19].

The results of the nitrogen sorption measurement suggest that a similar phenomenon could have occurred during the loading process in this work since the ARG solution was alkaline, as expected [12]. During the impregnation step, a gradual dissolution of the silica walls may have occurred so leading to the opening of the interconnections between the pores, which resulted, then, in the formation of new pores with an average diameter of 3.6 nm. Besides that, the decrease of both the volume and the size of the original pores of the as-synthesized material (2.4 nm) may be associated to the redeposition of soluble silica species on the pore surface and at the pore mouth. However, the pore size reduction as well as the decrease of the SSA_{BET} and pore volume (Table 6.1) may partially be due also to the presence of ARG molecules on the silica surface.

Table 6.1 SSA_{BET} and Pore volume of SMSP and ARG-11@SMSP

Sample	SSA_{BET} (m^2/g)	Pore volume (cm^3/g)
SMSP	1143	0.82
ARG-11@SMSP	786	0.51

In order to verify that the change in the textural properties was due to the exposure to the alkaline pH during impregnation, an as-synthesized SMSP sample was simply treated both with distilled water and a basic solution (i.e. an NH_4OH solution at pH≈11) following the same procedure used for impregnation. After, nitrogen sorption analysis was carried out on both samples. As far as the sample treated with water is concerned (named SMSP-H_2O), the isotherm (figure 6.4) was type IV without hysteresis as observed for the untreated SMSP. Instead, a significant change in the isotherm of the sample treated with NH_4OH (named SMSP-NH_4OH, figure 6.4) was observed, with the appearance of a type H2 hysteresis. These results suggested that the degradation of SMSP depends on the pH of the impregnated solutions.

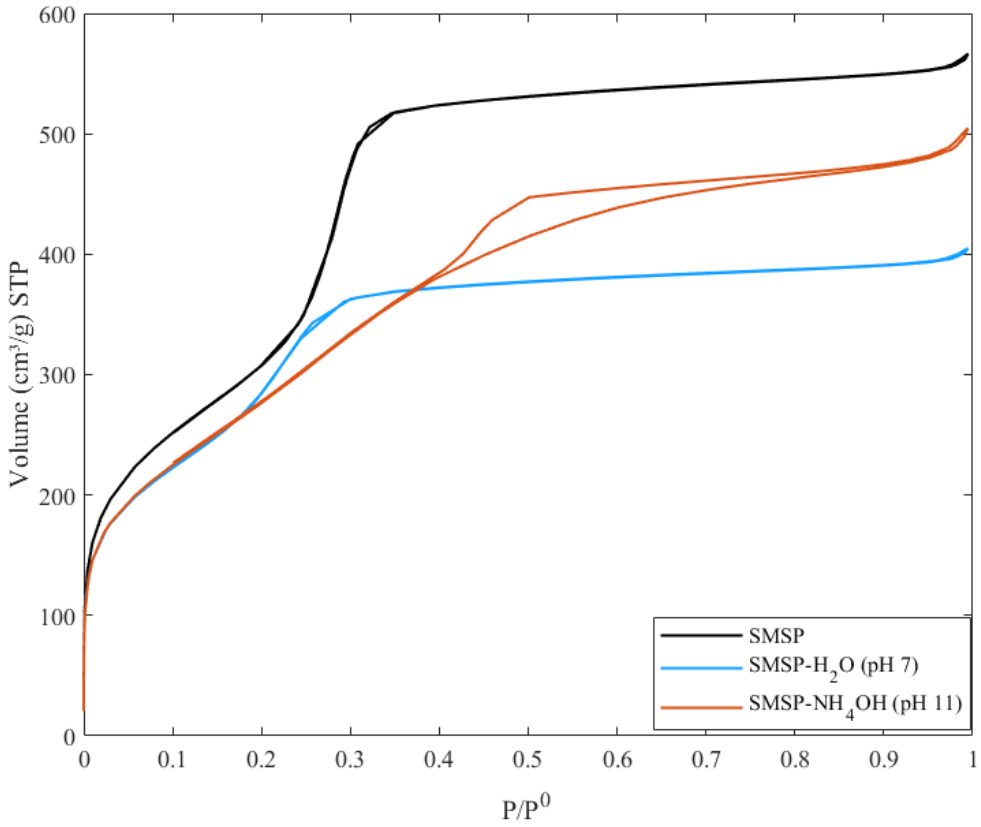

Figure 6.4 The nitrogen adsorption-desorption isotherms of SMSP (black curve), SMAP-H_2O (sky-blue curve) and SMSP-NH_4OH (brown curve).

The FESEM images of SMSP and ARG11@SMSP are reported in figure 6.5. As far as the ARG-11@SMSP sample (figure 6.5b) is concerned, no remarkable changes were observed in the morphology when compared to the as-synthesized material (figure 6.5a), i.e., the particles appeared spherical. However, a rough surface was observed, which was not present in the unimpregnated SMSP. This evidence is consistent with those obtained through the nitrogen sorption analysis, indicating that SMSP are unstable to the loading process and suffer degradation.

(a) (b)

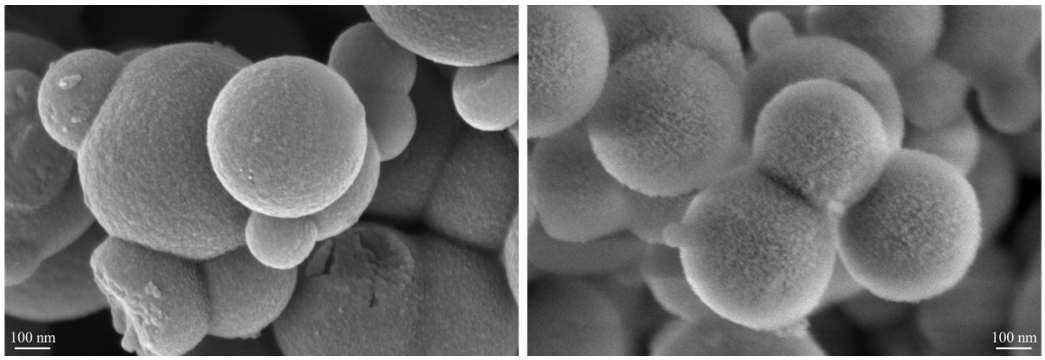

Figure 6.5 The FESEM images of SMSP and ARG-11@SMSP (magnification 250.00 K X).

To investigate the pysical state of ARG inside the SMSP pores, an XRD analysis was performed on the ARG-11@SMSP sample. The XRD patterns of SMSP, ARG-11@SMSP and pure ARG are reported in figure 6.6. The XRD pattern of pure ARG presents well-defined peaks of the crystalline phase. The XRD patterns of SMSP and ARG-11@SMSP are typical of amorphous silica and no peaks due to crystalline ARG are observed in the ARG-11@SMSP sample, indicating the presence of ARG in its amorphous form.

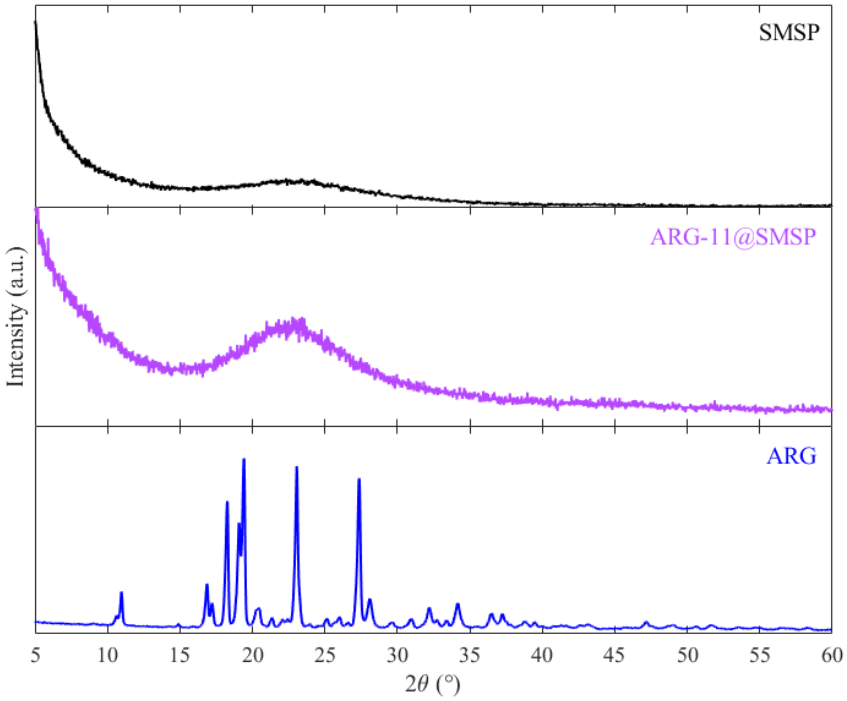

Figure 6.6 The XRD patterns of SMSP (black), ARG-11@SMSP (purple) and pure ARG (blue).

To confirm the successful loading of ARG, FT-IR spectroscopy was carried out on the ARG-11@SMSP sample. Figure 6.7 reports the FT-IR spectra of SMSP as such, ARG-11@SMSP and pure ARG. The spectrum of the as-synthesized SMSP is typical of amorphous silica, with the narrow band at 3746 cm^{-1} due to the isolated silanols and a broad absorption at about 3530 cm^{-1} due to the H-bonded silanols [20]. As far as the spectrum of ARG-11@SMSP is concerned, a reduction of the intensity of the peak associated to the isolated silanols is observed. Moreover, a new broad absorption band appears in the 3500-2500 cm^{-1} range, to which several narrower bands are superimposed. The lower intensity of the peak due to the isolated silanols suggests that in ARG-11@SMSP these are perturbed, probably by the H-bonding interaction with the ARG molecules, so forming the new broad absorption band below 3500 cm^{-1}. The narrower bands in the 3500-3100 cm^{-1} range and below 3000 cm^{-1} are ascribed to the NH stretching and CH stretching modes of the ARG molecules, respectively. Other several bands due to the adsorbed ARG molecules are observed in the 1700-1300 cm^{-1} range. In particular, the two bands at 1670 cm^{-1} and at 1630 cm^{-1} correspond to the antisymmetric and symmetric stretching of the guanidine group, respectively [21]. A shoulder is observed at about 1560 cm^{-1}, which

can be assigned to the antisymmetric stretching of the COO^- carboxylate groups [22]. The above results suggest the presence of the zwitterionic form of ARG in the ARG-11@SMSPsample, which is in accordance with the ionization state of the amino acid (figure 6.8) in the impregnation solution at a pH value of about 11 [7].

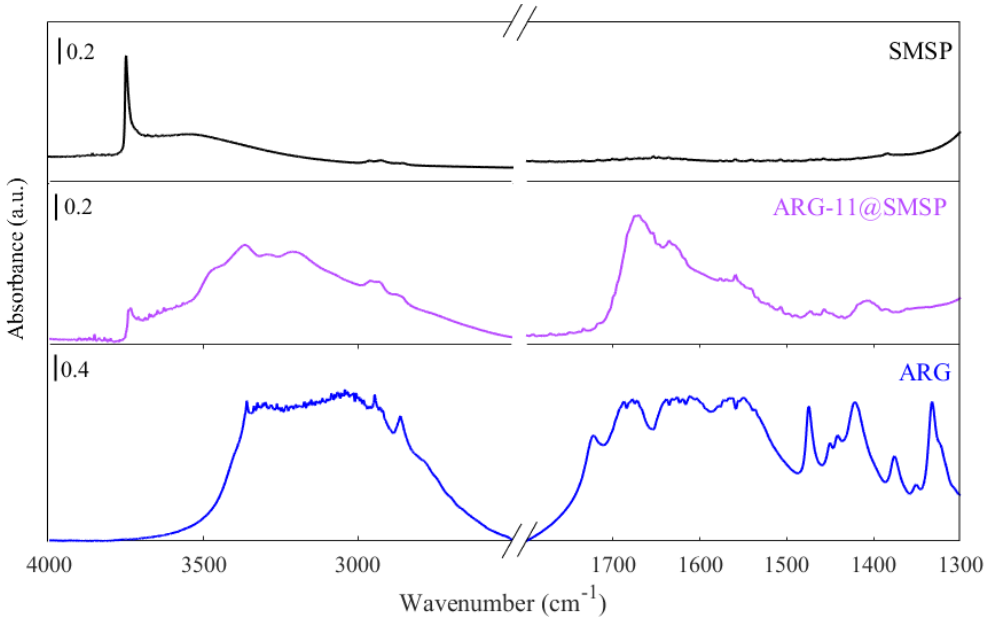

Figure 6.7 The FT-IR spectra of SMSP (in black), ARG-11@SMSP (in purple) and pure ARG (blue).

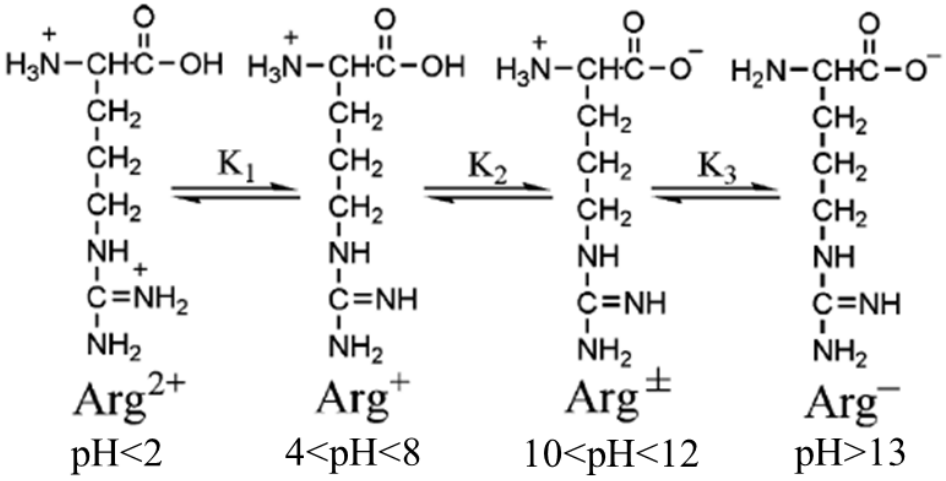

Figure 6.8 Ionization States of ARG in aqueous solution (adapted from [7]).

6.3.2 Characterization of ARG-x@SMSP

In order to understand the effect of the pH of the impregnating solution in the degradation of the SMSP, the loading process was performed at different pH values with the same amount of ARG.

Figure 6.9 shows the nitrogen adsorption-desorption isotherms and pore size distributions of all samples. By decreasing the pH of the impregnating solution, the shape of the isotherms (figure 6.9a) changes and the hysteresis loop disappears. The isotherm of the sample impregnated at acidic pH (ARG-5@SMSP) is similar to that of SMSP as such. The SSA_{BET} decreased from 1143 m^2/g, for the as-synthetized material, to 792 m^2/g, after the ARG loading, instead the pore volume decreased from 0.82 cm^3/g to 0.46 cm^3/g, and this is ascribed to the presence of the loaded ARG molecules.

Also, the pore size distribution (figure 6.9b) changed after decreasing the pH of the impregnating solution. The family of pores with a diameter of 3.6 nm almost disappeared for ARG-9@SMSP and the pore size distribution of ARG-5@SMSP was unimodal with an average pore size of 2.2 nm. As stated earlier for the SSA_{BET} and pore volume values, the lower average pore size of the ARG-5@SMSP sample (2.2 nm) with respect to the SMSP as such (2.4 nm) can be ascribed to the presence of ARG molecules inside the mesopores or at the pores mouth.

(a)

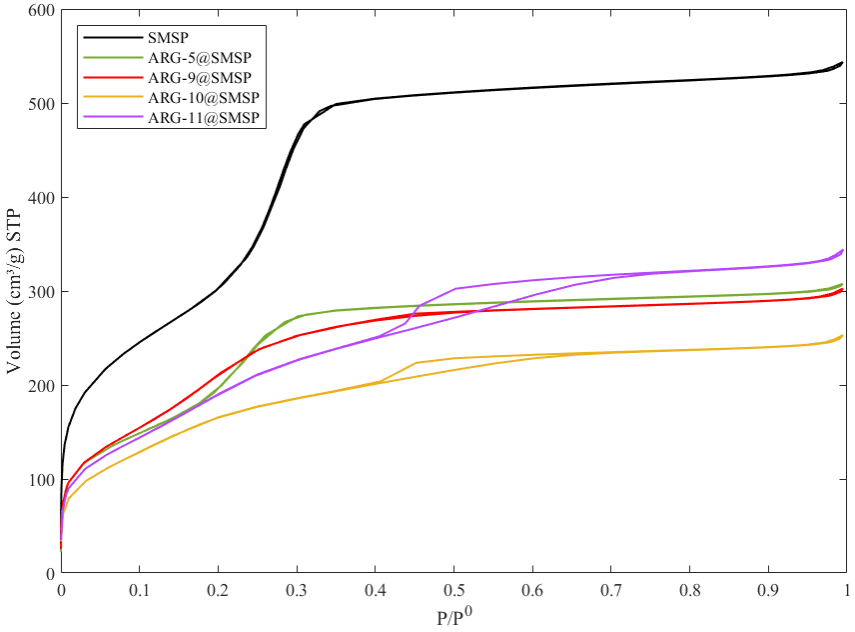

(b)

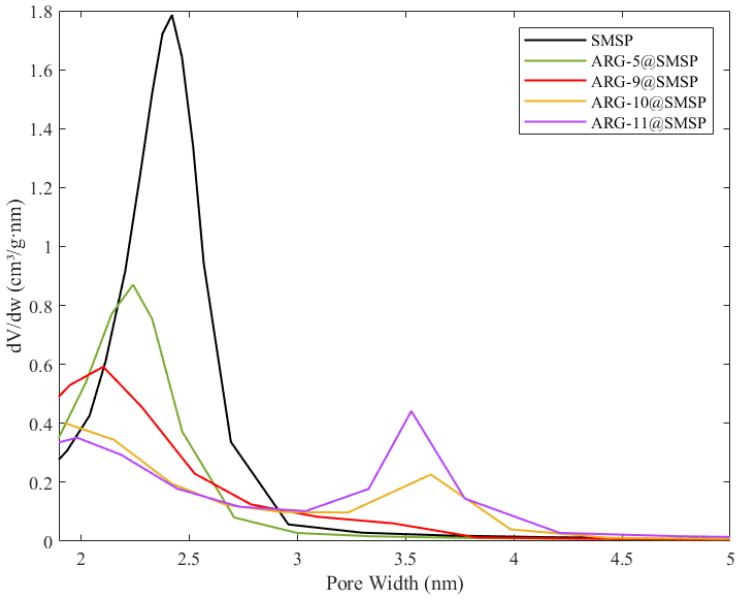

Figure 6.9 (a) The nitrogen adsorption-desorption isotherms and (b) PSD of SMSP (black curve), ARG-5@SMSP (green curve), ARG-9@SMSP (red curve), ARG-10@SMSP (yellow curve) and ARG-11@SMSP (purple curve).

All results indicate that the degradation of SMSP is due to the pH of the ARG solution employed for the impregnation process and is not related to the interaction of the silica with ARG. In particular, this degradation, which affects the porosity, occurs at pH values included between 9 and 11. The SMSP are not inert towards the ARG loading process by means of wet impregnation when water is used as a solvent. This occurs even though only a small amount of solution is employed as it happens in the present case, where about 2 ml of impregnating solution are in contact with 200 mg of silica support. On the other hand, the impregnation at pH 5, which occurs at the same ARG concentration, allows the integrity of the SMSP carrier to be maintained.

The FESEM images of SMSP and ARG-5@SMSP are reported in figure 6.10. Contrary to what observed for the ARG-11@SMSP sample (figure 6.5b), neither a morphology change nor an increase in roughness of the particle surface can be observed for the ARG-5@SMSP sample (figure 6.10b) when compared to SMSP as such (figure 6.10a). This result further confirms that the impregnation process performed using an acidic ARG solution does not cause any degradation of SMSP. This agrees t with the results obtained from the nitrogen sorption analysis (figure 6.9) and data reported in the literature regarding the stability of mesoporous silica in acidic solutions [10,11].

(a) (b)

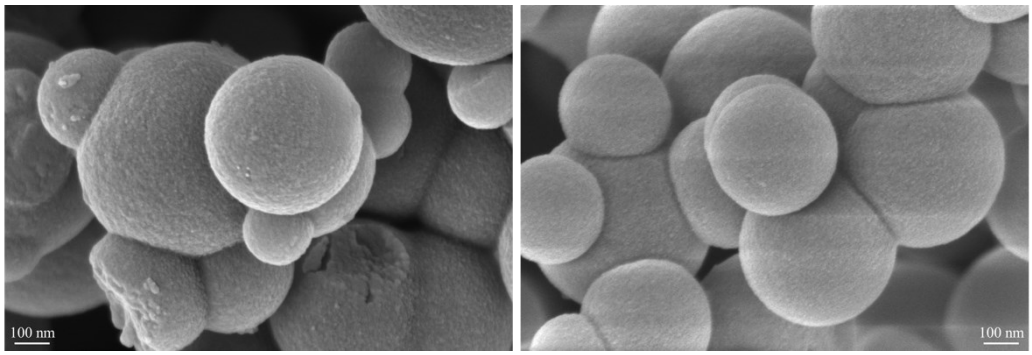

Figure 6.10 The FESEM image of SMSP and ARG-5@SMSP (magnification 250.00 K X).

Figure 6.11 compares the XRD patterns of SMSP, ARG-5@SMSP, ARG-9@SMSP and ARG-10@SMSP. In all the patterns, no peaks ascribed to crystalline ARG are observed, revealing the presence of ARG in its amorphous form, as observed for ARG-11@SMSP.

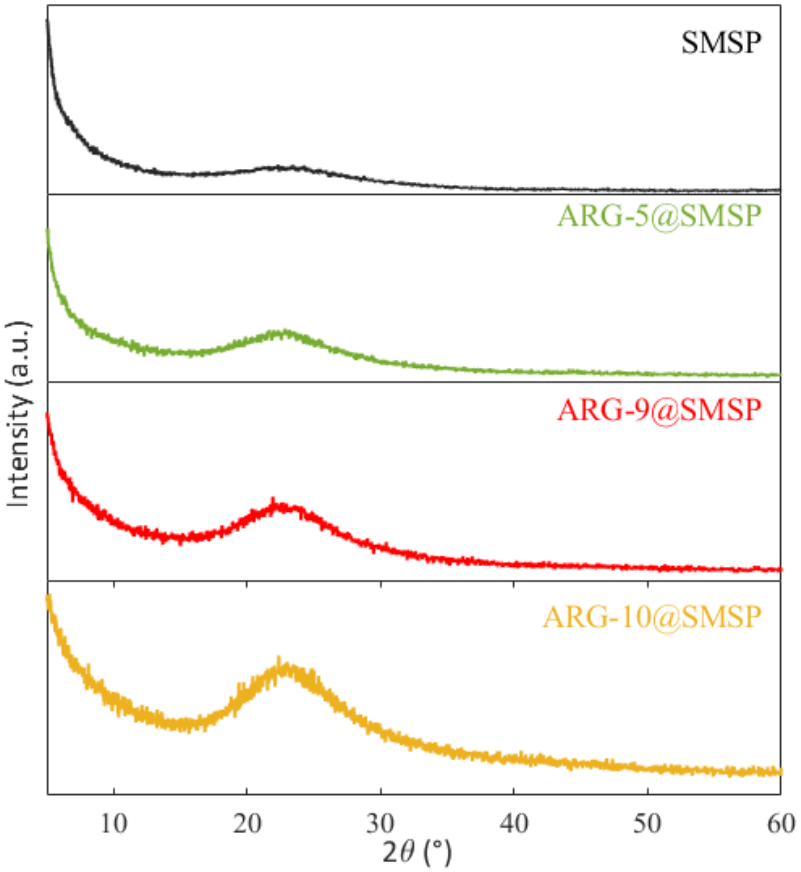

Figure 6.11 The XRD patterns of SMSP (black), ARG-5@SMSP (green), ARG-9@SMSP (red) and ARG-10@SMSP (yellow).

Figure 6.12 shows the FT-IR spectra of SMSP, ARG-5@SMSP, ARG-9@SMSP and ARG-10@SMSP. In the spectra of ARG-5@SMSP, ARG-9@SMSP and ARG-10@SMSP the low intensity of the band due to the isolated silanols at 3746 cm^{-1} and the broad absorption band between 3500 cm^{-1} and 2500 cm^{-1} reveal the occurrence of H-bonding interactions between the silica surface and the ARG molecules. For the ARG-9@SMSP and ARG-10@SMSP samples, the spectra in the 1700 -1300 cm^{-1} range are very similar to that reported for ARG-11@SMSP (figure 6.7), suggesting the presence of the zwitterionic form of ARG. Instead, in

the spectrum of ARG-5@SMSP the antisymmetric stretching of COO^- at about 1560 cm^{-1} disappeared, revealing the protonation of the carboxylate groups in the sample impregnated at pH 5, as expected for the ARG molecules dissolved in an aqueous solution in the 4-8 pH range (figure 6.8) [7].

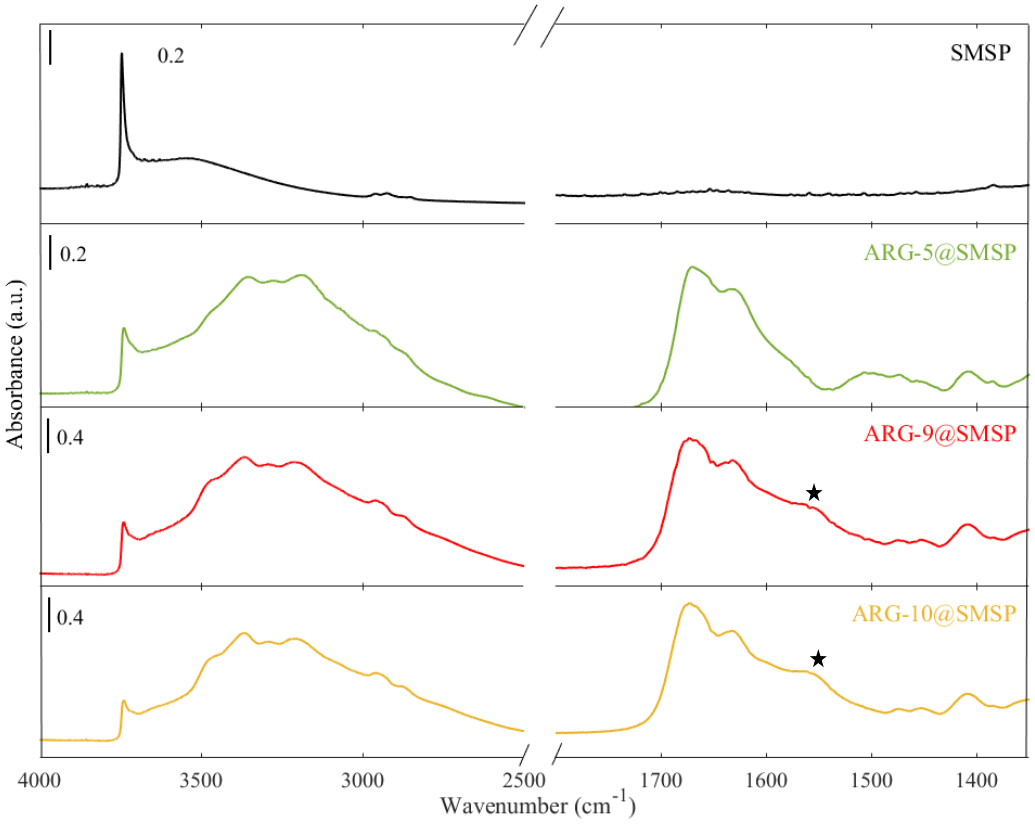

Figure 6.12 The FT-IR spectra of SMSP (in black), ARG-5@SMSP (in green), ARG-9@SMSP (in red) and ARG-10@SMSP (in yellow).

6.3.3 Preliminary desorption test

The desorption test aimed at evidencing if the partial degradation of the carrier and the modification of its porosity could affect its release capability. To this purpose, the tests were performed on the ARG-11@SMSP and the ARG-5@SMSP samples. ARG-11@SMSP was selected because the carrier underwent significant degradation, while in the ARG-5@SMSP no evidence of degradation was observed.

The FT-IR spectra of the powders recovered after the desorption test (10 minutes and 60 minutes) are reported in figure 6.13. The FT-IR spectra of ARG-

5@SMSP-10 min and ARG-5@SMSP-60 min (figure 6.13a) did not show any band related to ARG, so confirming its total desorption. Instead, the characteristic bands ascribed to ARG were still observed for ARG-11@SMSP-10 min and ARG-11@SMSP-60 min (figure 6.13b), which confirms the presence of residual ARG in the carrier. The results of the analysis are summarized in table 6.2.

(a)

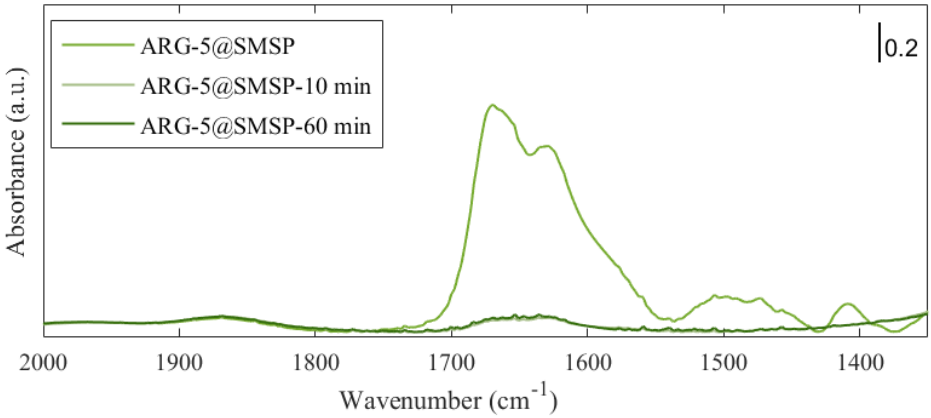

(b)

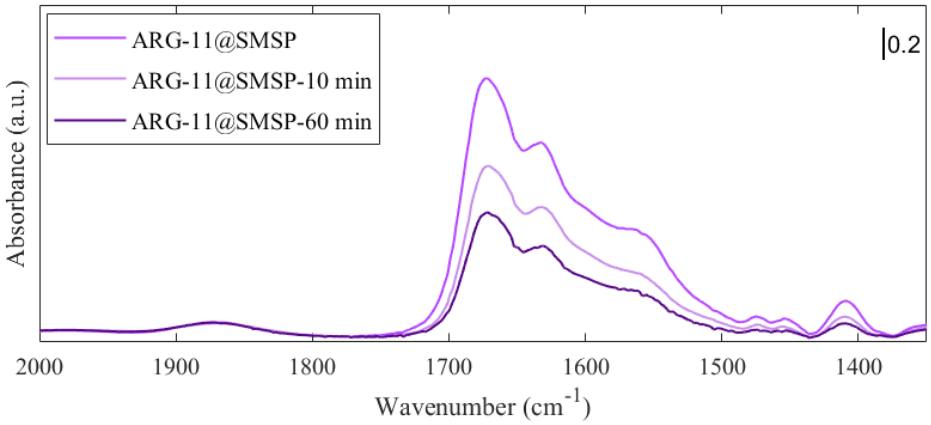

Figure 6.13 The FT-IR Spectra of (a) ARG-5@SMSP and (b) ARG-11@SMSP at different desorption times.

Table 6.2 Results of the desorption test of ARG-5@SMSP and ARG-11@SMSP.

Sample	Time (min)	ARG in the carrier (%)	ARG desorbed (%)
ARG-5@SMSP	0	100	0
	10	0	100
	60	0	100
ARG-11@SMSP	0	100	0
	10	66	34
	60	48	52

The desorption of a significant lower amount of ARG from the ARG-11@SMSP sample may be ascribed to a slower diffusion of the ARG molecules from the SMSP carrier to the receiving solution due to the presence of a disordered porosity with ink-bottle pores. Moreover, the interaction of the ARG molecules with the silica surface in ARG-11@SMSP may also contribute to this behavior. It may be speculated that the zwitterionic form of ARG present in ARG-11@SMSP, which is characterized by the delocalized negative charge of the carboxylic groups, may establish stronger dispersion interactions with the silica surface with respect to the protonated form of ARG (which is positively charged) [7] present in ARG-5@SMSP. Indeed, dispersion interactions have already been found to play a crucial role, together with H-bonding, in the interaction strength of drug molecules with the silica surface [23].

Moreover, H-bonding interactions between silanols and negatively charged carboxylate groups are expected to be stronger than those between silanols and carboxylic groups (present in the protonated ARG). This could also contribute to a stronger interaction between ARG molecules and the silica surface in ARG-11@SMSP than in ARG-5@SMSP.

In conclusion, the desorption tests revealed that ARG could be desorbed in water by both systems, i.e., SMSP impregnated at pH 11 and at pH 5. A complete desorption was observed from the SMSP impregnated at pH 5, whereas the

desorption appeared to be less extensive from the silica impregnated at the original basic conditions.

6.4 Conclusions

SMSP (with particle sizes ranging from 0.15 μm to 0.80 μm and average pore diameter of 2.4 nm) have been loaded with ARG (with a final content of 9.1 %w/w) through the wet impregnation technique by using water as a solvent. From the nitrogen sorption and FESEM analyses it can be concluded that the impregnation performed at the original basic pH of the ARG solution (i.e., pH ≈ 11) induced a significant modification of the porosity and of the surface of the particles, due to degradation ascribed to partial silica dissolution and reprecipitation. Instead, the impregnation performed by adjusting the pH of the ARG solution to acidic conditions (about 5) did not affect the carrier. The ARG was present in the SMSP carrier in its amorphous form in all samples. From the FT-IR analysis, it emerged that the ARG molecules were present as zwitterionic species in the samples impregnated at basic pHs and as positive protonated species in the sample impregnated at acidic pH.

The preliminary desorption tests showed that, despite the degradation of the carrier, also the SMSP impregnated at the original basic pH of the ARG solution were able to desorb ARG. Nevertheless, the desorption appeared less extensive than that observed for the carrier impregnated at acidic pH. This suggests that the desorption was inhibited by the disordered porosity with ink bottle pores formed by degradation and, possibly, also by the stronger interactions between the zwitterionic ARG molecules and the silica surface.

6.5 References

1. Mohamed, S. S. Y. *et al.* The Role of the pH in the Impregnation of Spherical Mesoporous Silica Particles with L-Arginine Aqueous Solutions. *Int. J. Mol. Sci.* **22**, 13403 (2021).

2. Sanjay, C., Ghate, V. M. & Lewis, S. A. Mesoporous silica particles for dermal drug delivery: A review. *Int. J. Appl. Pharm.* **10**, 23–26 (2018).

3. Arriagada, F., Nonell, S. & Morales, J. Silica-based nanosystems for therapeutic applications in the skin. *Nanomedicine* **14**, 2243–2267 (2019).

4. Quignard, S., Coradin, T., Powell, J. J. & Jugdaohsingh, R. Silica nanoparticles as sources of silicic acid favoring wound healing in vitro. *Colloids Surfaces B Biointerfaces* **155**, 530–537 (2017).

5. Nethi, S. K., Das, S., Patra, C. R. & Mukherjee, S. Recent advances in inorganic nanomaterials for wound-healing applications. *Biomater. Sci.* **7**, 2652–2674 (2019).

6. Vlasova, N. N. & Golovkova, L. P. The Adsorption of Amino Acids on the Surface of Highly Dispersed Silica. *Colloid J.* **66**, 733–738 (2004).

7. Gao, Q. *et al.* Amino acid adsorption on mesoporous materials: Influence of types of amino acids, modification of mesoporous materials, and solution conditions. *J. Phys. Chem. B* **112**, 2261–2267 (2008).

8. Patel, A. & Solanki, P. 12-Tungstophosphoric acid functionalized MCM-41 : synthesis , characterization and study of controlled in vitro release of L - arginine. *J. Porous Mater.* **23**, 1113–1123 (2016).

9. Solanki, P. & Patel, A. In vitro release of l-arginine and cysteine from MCM-48: a study on effect of size of active biomolecules on release rate. *J. Porous Mater.* **25**, 1489–1498 (2018).

10. Landau, M. V. *et al.* Wetting stability of Si-MCM-41 mesoporous material in neutral, acidic and basic aqueous solutions. *Microporous Mesoporous Mater.* **33**, 149–163 (1999).

11. Choudhary, V. R. & Sansare, S. D. Thermal, hydrothermal and acid-base

stability of highly siliceous MCM-41 mesoporous material. *Proc. Indian Acad. Sci. Chem. Sci.* **109**, 229–233 (1997).

12. Ninni, L. & Meirelles, A. J. A. Water activity, ph and density of aqueous amino acids solutions. *Biotechnol. Prog.* **17**, 703–711 (2001).

13. Jadhav, S. A., Miletto, I., Brunella, V., Scalarone, D. & Berlier, G. Porous Silica Particles : Synthesis , Physicochemical Characterization and Evaluation of Suspension Stability. *Phys. Chem. An Indian J.* 1–11 (2017).

14. Thommes, M. *et al.* Physisorption of gases, with special reference to the evaluation of surface area and pore size distribution (IUPAC Technical Report). *Pure Appl. Chem.* **87**, 1051–1069 (2015).

15. Bass, J. D. *et al.* Stability of mesoporous oxide and mixed metal oxide materials under biologically relevant conditions. *Chem. Mater.* **19**, 4349–4356 (2007).

16. Chen, G., Teng, Z., Su, X., Liu, Y. & Lu, G. Unique biological degradation behavior of stöber mesoporous silica nanoparticles from their interiors to their exteriors. *J. Biomed. Nanotechnol.* **11**, 722–729 (2015).

17. He, Q., Shi, J., Zhu, M., Chen, Y. & Chen, F. The three-stage in vitro degradation behavior of mesoporous silica in simulated body fluid. *Microporous Mesoporous Mater.* **131**, 314–320 (2010).

18. Escax, V. *et al.* Modifying the porosity of SBA-15 silicas by post-synthesis basic treatments. *Microporous Mesoporous Mater.* **102**, 234–241 (2007).

19. Paris, J. L., Colilla, M., Izquierdo-Barba, I., Manzano, M. & Vallet-Regí, M. Tuning mesoporous silica dissolution in physiological environments: a review. *J. Mater. Sci.* **52**, 8761–8771 (2017).

20. A. Rimola, D. Costa, M. Sodupe, J.-F. Lambert, P. U. Silica Surface Features and Their Role in the Adsorption of Biomolecules: Computational Modeling and Experiments. *Chem. Rev* **113**, 4216–4313 (2013).

21. Venyaminov, S. Y. & Kalnin, N. N. Quantitative IR spectrophotometry of peptide compounds in water (H2O) solutions. I. Spectral parameters of amino acid residue absorption bands. *Biopolymers* **30**, 1243–1257 (1990).

22. Wolpert, M. & Hellwig, P. Infrared spectra and molar absorption coefficients of the 20 alpha amino acids in aqueous solutions in the spectral range from 1800 to 500 cm-1. *Spectrochim. Acta - Part A Mol. Biomol. Spectrosc.* **64**, 987–1001 (2006).

23. Gignone, A., Delle Piane, M., Corno, M., Ugliengo, P. & Onida, B. Simulation and Experiment Reveal a Complex Scenario for the Adsorption of an Antifungal Drug in Ordered Mesoporous Silica. *J. Phys. Chem. C* **119**, 13068–13079 (2015).

Chapter 7
Impregnation of Mesoporous Silica Microspheres with l-arginine

7.1 Introduction

In this chapter the work presented in Chapter 6 is extended to a second type of mesoporous silica particles as carriers for ARG. As stated in chapter 6, SMSP suffered from degradation during the loading of ARG. The degradation could be favored by the fact that SMSP probably present thin pore walls, on the basis of the preparation process carried out at room temperature and due to the template used in the synthesis [1]. Thin pore walls could, in fact, be more vulnerable to degradation after their exposure to an alkaline environment. Indeed, MCM-41-type mesoporous silicas usually present wall thickness of about 1 nm [1,2].

In the attempt to overcome this limitation, MSM was considered for impregnation with ARG solution. As described in Chapter 3, MSM were prepared using Pluronic as the template and a hydrothermal treatment during the synthesis, similarly to the procedure used for the synthesis of SBA-15 [3]. It is known that SBA-15 type silica present higher stability due to their thicker walls (3.1 to 6.4 nm) as well as larger pores (from 4.6 to 30 nm) when compared to MCM-41 silicas [4].

For this purpose, sample MSM-1°C/min was chosen for the loading of ARG as it presents higher surface area and pore volume. The ARG loading was performed through the wet impregnation method at different pH values of the impregnating solution, as described in Chapter 6 for SMSP. The characterization of the physicochemical properties of the material after ARG incorporation was carried out

using the same techniques used for SMSP, i.e. nitrogen sorption analysis, Field Emission Scanning Electron Microscopy (FESEM), X-ray diffractometry (XRD) and Fourier transformed infrared spectroscopy (FT-IR). Furthermore, a preliminary desorption test was performed in water to investigate the effect of the pH of the impregnation process on the desorption ability of the carrier.

7.2 Experimental

7.2.1 MSM synthesis and ARG loading

The synthesis of MSM-1°C/min sample was performed following the procedure reported in chapter 3 (subsection 3.3.2). The loading of ARG was carried out at pH 5 and pH 11 according to the same procedure described in Chapter 6 (subsection 6.2.2) of this thesis. The obtained materials were named ARG-x@MSM-1°C/min, where x indicates the pH value of the ARG/H_2O impregnating solution.

7.2.2 Instrumental characterization

The nitrogen sorption analysis was performed using a Quantachrome AUTOSORB-1 instrument. Before the adsorption measurements, MSM-1°C/min was outgassed for 2 h at 150 °C, while the samples loaded with ARG were outgassed at 70 °C for 2 h. The BET specific surface areas (SSA_{BET}) were calculated in the relative pressure range of 0.04 - 0.1. Pore size distribution was achieved by the DFT method from the desorption branch of the isotherm and the average pore size was determined from the distribution. The total pore volume was determined at a relative pressure of about 0.99.

The FESEM images were recorded with a Fei Quanta 200F instrument. The X-ray diffraction (XRD) patterns were obtained with a PANalytical X'Pert diffractometer (Cu Kα radiation, wavelength = 1.54187 Å). The data were collected from 5° to 60° (2θ) with a step size of 0.026° (2θ).

The FT-IR analysis was performed using a Bruker Equinox 55 spectrometer. The FT-IR spectra of materials were obtained on self-supported pellets, prepared by pressing the powder with a hydraulic press. All samples were outgassed in high vacuum (residual pressure equal to 0.1 Pa) at room temperature for 1 h. The spectra were obtained from 4000 cm^{-1} to 600 cm^{-1} with a resolution of 2 cm^{-1}.

7.2.3 Preliminary desorption test

A preliminary desorption test was performed by soaking the ARG-x@MSM-1°C/min samples in water at 35 °C and under continuous stirring. Different batches were prepared by soaking 10 mg of ARG-x@MSM-1°C/min in 10 ml of water. The final pH of the medium was about 7 and it remained constant during the test.

At prefixed times (10 and 60 minutes) samples were recovered from the desorption test (ARG-x@MSM-1°C/min-ymin, where y indicates the time at which the powder was collected) and analyzed by FT-IR spectroscopy. The obtained spectra were compared with the spectra of ARG-x@MSM-1°C/min and a semi-quantitative analysis of ARG content present in the samples was carried out considering the most intense absorption band of ARG, at 1670 cm^{-1}, which corresponds to the stretching vibration of the guanidine, as described in chapter 6 (subsection 6.2.4).

7.3 Results and Discussion

7.3.1 Characterization of ARG-x@MSM-1°C/min

Figure 7.1 shows the nitrogen adsorption-desorption isotherm of MSM-1°C/min and pore size distribution before and after the loading of ARG. The values of SSA_{BET} and pore volume are summarized in table 7.1.

The isotherms (figure 7.1a) of the samples loaded with ARG (i.e. ARG-5@MSM-1°C/min and ARG-11@MSM-1°C/min) are both similar to that of MSM-1°C/min as such. In addition, no significant change could be observed in the pore size distribution (figure 7.1b) for both sample ARG-5@MSM-1°C/min and sample ARG-11@MSM-1°C/min when compared to the as synthesized material (MSM-1°C/min).

At variance with what previously observed for sample ARG-11@SMSP, where a significant change in the adsorption-desorption isotherms occurred upon ARG loading at basic pH (Chapter 6 subsection 6.3.1), these results suggest that the impregnation process did not affect the porosity of the carrier.

(a)

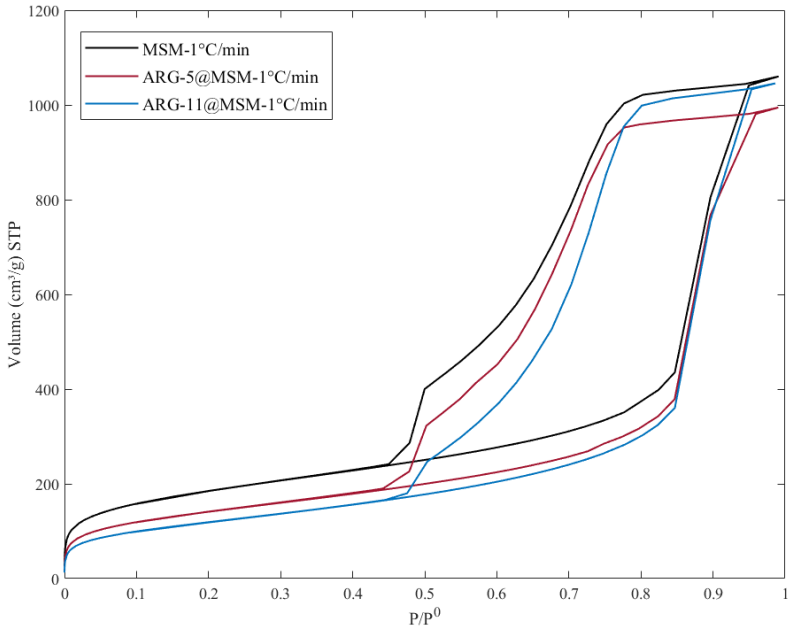

(b)

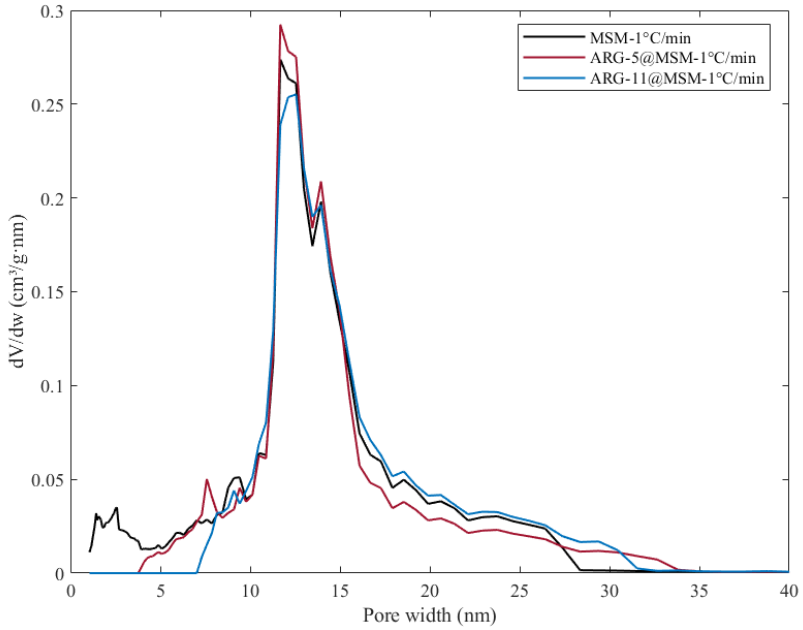

Figure 7.1 (a) The nitrogen adsorption-desorption isotherms and (b) PSD of MSM-1°C/min, ARG-5@MSM-1°C/min and ARG-11@MSM-1°C/min.

As illustrated in table 7.1 a decrease in the SSA_{BET} and pore volume could be observed for samples ARG-5@MSM-1°C/min and ARG-11@MSM-1°C/min with respect to the as-synthesized MSM. This is ascribed to the adsorption of the ARG molecules on the surface of the MSM-1°C/min material.

Table 7.1 SSA_{BET} and Pore volume of MSM-1°C/min, ARG-5@ MSM-1°C/min and ARG-11@ MSM-1°C/min.

Sample	SSA_{BET} (m^2/g)	Pore volume (cm^3/g)
MSM-1°C/min	674	1.64
ARG-5@ MSM-1°C/min	515	1.54
ARG-11@ MSM-1°C/min	433	1.62

FESEM images of MSM, ARG-5@MSM-1°C/min and ARG-11@MSM-1°C/min are reported in figure 7.2. No remarkable changes in the morphology or roughness of particles surface can be observed for both samples ARG-5@MSM-1°C/min (figure 7.2b) and ARG-11@MSM-1°C/min (figure 7.2c) when compared to the MSM-1°C/min (figure 7.2a) as such. As far as sample ARG-11@MSM-1°C/min is concerned, connections and junctions between the spheres are visible in the FESEM image (figure 7.2c), which may be due to partial dissolution and reprecipitation of silica. Nevertheless, the above result suggests that MSM-1°C/min are more stable toward the loading of ARG than SMSP (Chapter 6), in accordance with the results obtained from the nitrogen sorption analysis (figure 7.1). This behaviour may be ascribed to a higher stability of MSM-1°C/min in alkaline environment, as expected for an SBA-15-type silica when compared to an MCM-41-type one.

(a)

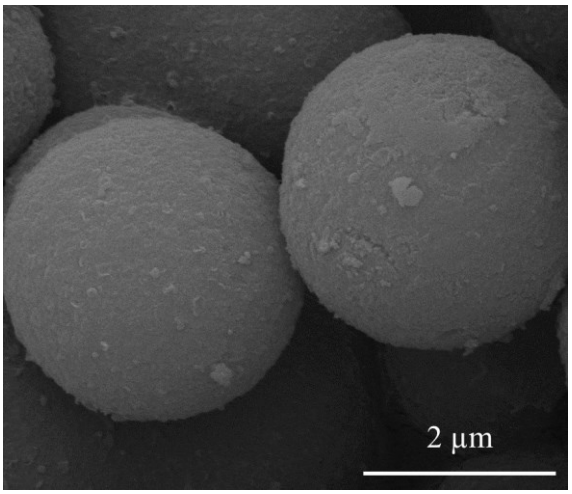

(b) (c)

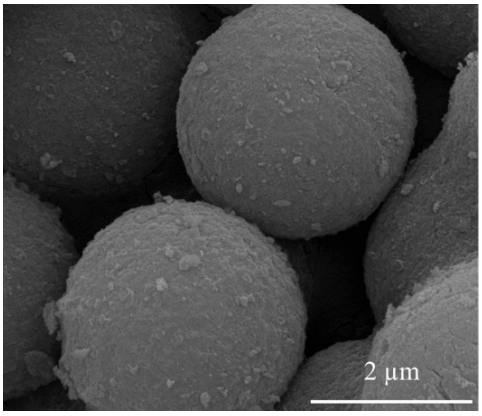

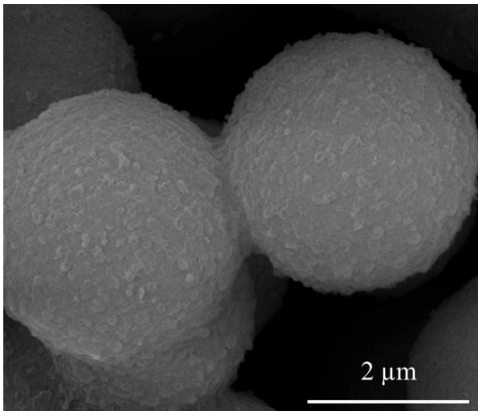

Figure 7.2 The FESEM images of (a) MSM-1°C/min, (b) ARG-5@ MSM-1°C/min and (c) ARG-11@ MSM-1°C/min (magnification 20.00 K X).

In order to characterize the physical state of ARG inside the MSM-1°C/min pores, an XRD analysis was performed on samples ARG-5@MSM-1°C/min and ARG-11@MSM-1°C/min. The XRD patterns of MSM-1°C/min, ARG-5@MSM-1°C/min and ARG-11@MSM-1°C/min and pure ARG are shown in figure 7.3. The XRD patterns of MSM-1°C/min (for comparison), ARG-5@MSM-1°C/min and ARG-11@MSM-1°C/min are typical of amorphous silica and no peaks due to crystalline ARG are observed in ARG-5@MSM-1°C/min and ARG-11@MSM-1°C/min samples, suggesting the presence of ARG in its amorphous form.

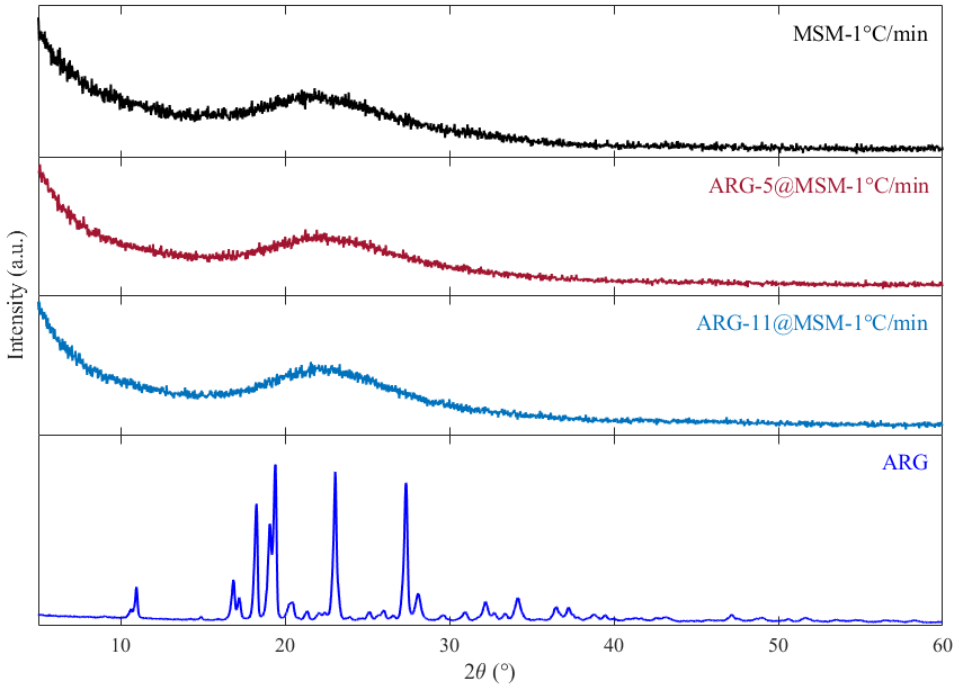

Figure 7.3 The XRD patterns of MSM-1°C/min, ARG-5@MSM-1°C/min, ARG-11@MSM-1°C/min and pure ARG.

The characterization of the ARG molecules inside ARG-5@MSM-1°C/min and ARG-11@MSM-1°C/min was carried out by means of FT-IR spectroscopy. Figure 7.4 reports the FT-IR spectra of MSM (for comparison), ARG-5@MSM, ARG-11@MSM and pure ARG. As previously discussed (Chapter 3 subsection 3.3.1), the spectrum of the MSM-1°C/min as such is typical of amorphous silica, with the narrow band at 3740 cm^{-1} due to the isolated silanols and a broad absorption band at about 3500 cm^{-1} due to H-bonded silanols [5]. As far as samples ARG-5@MSM-1°C/min and ARG-11@MSM-1°C/min are concerned, a decrease in the intensity of the band due to the isolated silanols at 3740 cm^{-1} and a broad absorption band between 3500 cm^{-1} and 2500 cm^{-1} are observed, revealing the occurrence of H-bonding interactions between the silica surface and the ARG molecules, as for the ARG-x@SMSP samples. For sample ARG-11@MSM-1°C/min, the spectrum in the 1700-1300 cm^{-1} range is very similar to that reported for ARG-11@SMSP (Chapter 6 subsection 6.3.1): two bands at 1670 cm^{-1} and at 1630 cm^{-1}, which correspond to the antisymmetric and symmetric stretching of the guanidine group, respectively, and a shoulder at about 1560 cm^{-1} ascribed to the antisymmetric stretching of COO^- carboxylate groups can be observed, suggesting

the presence of the zwitterionic form of ARG [6,7]. Instead, in the spectrum of ARG-5@MSM-1°C/min the antisymmetric stretching of COO^- at about 1560 cm^{-1} disappeared, indicating the protonation of the carboxylate groups in the sample impregnated at pH 5, as observed for sample ARG-5@SMSP (Chapter 6 subsection 6.3.2) [8].

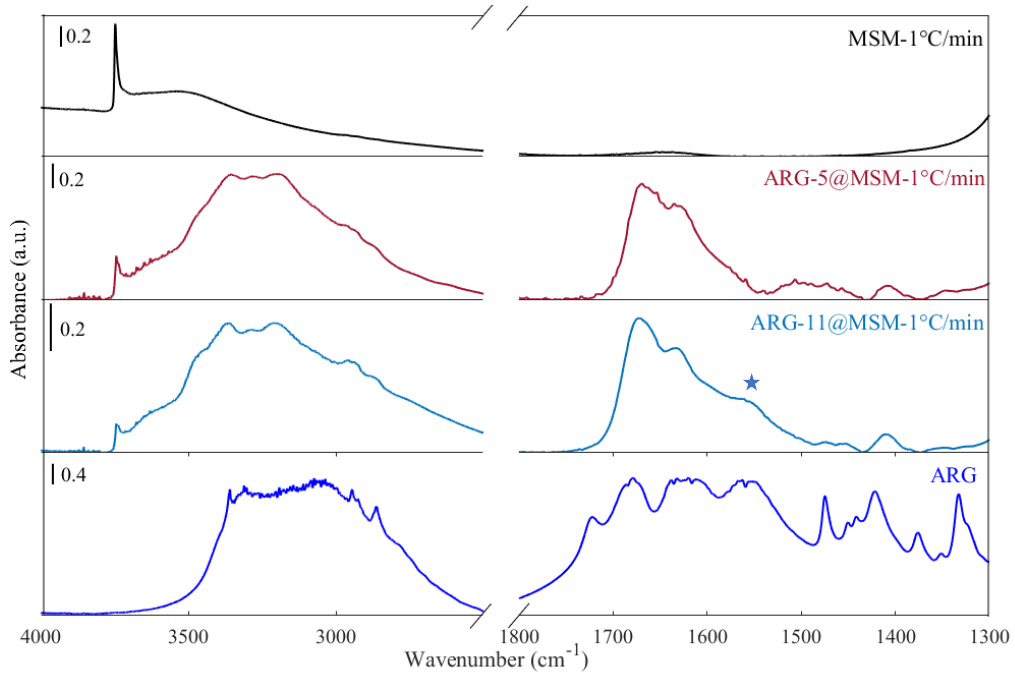

Figure 7.4 FTIR spectra of MSM-1°C/min, ARG-5@MSM-1°C/min, ARG-11@ MSM-1°C/min and pure ARG.

7.3.2 Preliminary desorption test of ARG

The aim of the desorption test was to evidence if the pH of the impregnating solution could affect the desorption of ARG as previously observed for the ARG-x@SMSP samples (Chapter 6 subsection 6.3.3). The FT-IR spectra of the powders recovered after the desorption tests (10 minutes and 60 minutes) are reported in figure 7.5. As far as sample ARG-5@ MSM-1°C/min is concerned, a complete release within 10 minutes was observed. On the other hand, about a half of the original ARG amount was released in the same time interval by the ARG-11@MSM-1°C/min sample. A similar behavior was also observed for samples

ARG-5@SMSP and ARG-11@SMSP (Chapter 6 subsection 6.3.3). The results of the analysis are summarized in table 7.2.

(a)

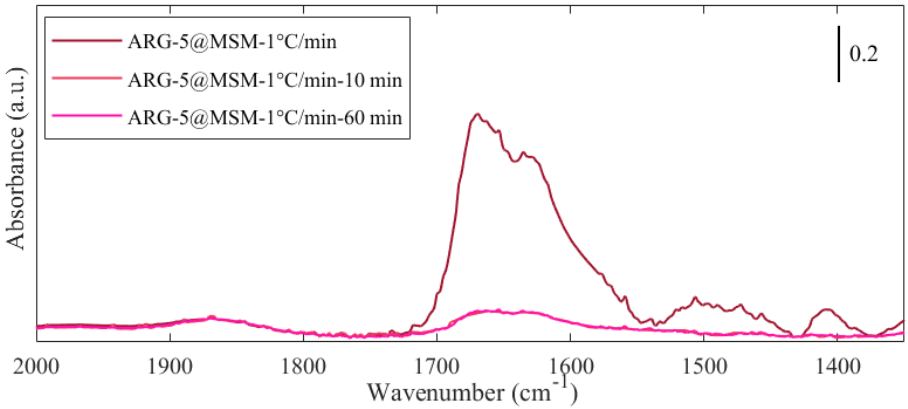

(b)

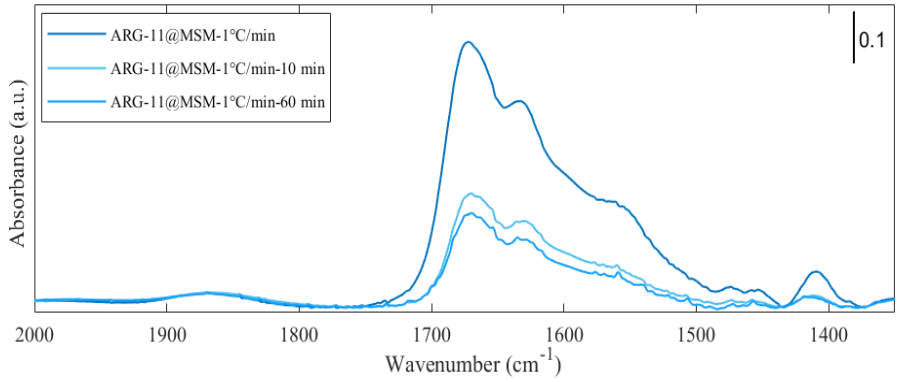

Figure 7.5 FT-IR Spectra of (a) ARG-5@MSM-1°C/min and (b) ARG-11@MSM-1°C/min at different desorption times.

Table 7.2 Results of the desorption test of ARG-5@MSM-1°C/min and ARG-11@MSM-1°C/min.

Sample	Time (min)	ARG in the carrier (%)	ARG desorbed (%)
ARG-5@MSM-1°C/min	0	100	0
	10	0	100
	60	0	100
ARG-11@MSM-1°C/min	0	100	0
	10	42	58
	60	35	65

From the analysis of the data obtained from the desorption tests, it could be concluded that the desorption behavior is affected by the pH of the ARG solutions used for the impregnation. Indeed, both silica samples (SMSP and MSM-1°C/min) impregnated at acidic pH (i.e. ARG-5@SMSP and ARG-5@MSM-1°C/min), showed a complete desorption of the ARG molecules within 10 minutes. On the other hand, the samples impregnated at pH 11 (i.e., ARG-11@SMSP and ARG-11@MSM-1°C/min) still contain some ARG molecules after 1 hour of contact with water. Due to the large pores present in the MSM carrier, this difference is eventually ascribed to the different interaction between the ARG molecules and the silica surface.

Generally, three kinds of interactions may arise between amino acids and a silica surface: (1) electrostatic forces between the amino acid ions and charged $SiOH^+$ and SiO^-; (2) hydrogen bonds between the amino acid molecules and/or ions and SiOH; (3) hydrophobic interactions between the side chain of the amino acid and the Si-O-Si groups [8].

As discussed in Chapter 6 (subsection 6.3.3) it may be speculated that the zwitterionic form of ARG present in ARG-11@SMSP and ARG-11@MSM-1°C/min, which is characterized by the delocalized negative charge of the carboxylic groups, may establish stronger dispersion interactions with the silica surface with respect to the protonated form of ARG (which is positively charged [8]

and is present in ARG-5@SMSP and ARG-5@MSM-1°C/min). Indeed, dispersion interactions have already been found to play a crucial role, together with H-bonding, in the interaction strength of drug molecules with the silica surface [9].

Moreover, H-bonding interactions between silanols and the negatively charged carboxylate groups are expected to be stronger than those between silanols and carboxylic groups (present in the protonated ARG). This could also contribute to a stronger interaction between ARG molecules and the silica surface in the samples impregnated at basic pH.

Besides all the above considerations, a certain degree of occlusion of the ARG molecules in both mesoporous silicas impregnated at basic pH, due to the partial dissolution and reprecipitation of silica, cannot be ruled out, so accounting for the desorption of only a fraction of the loaded arginine molecules.

7.4 Conclusions

MSM (with particle sizes in the 2 - 5 μm range and average pore diameter of 12 nm) were loaded with ARG through the wet impregnation technique by using water as a solvent. The nitrogen sorption analysis and FESEM analysis evidenced that the impregnation process carried out at acidic pH (i.e., pH ≈ 5) and basic pH (i.e., pH ≈ 11) did not induce any significant change in the porosity and in the surface of the particles. Nevertheless, a certain degree of dissolution and reprecipitation of silica cannot be ruled out, since evidence of connections and junctions among MSM particles loaded at basic pH was revealed by the FESEM images.

The XRD analysis revealed that ARG was present in the carrier in its amorphous form in all samples. FT-IR spectroscopy showed that the ARG molecules were present as zwitterionic species in the samples impregnated at basic pHs and as positive protonated species in the sample impregnated at acidic pH.

The preliminary desorption tests showed that both samples were able to desorb the loaded ARG. The desorption of ARG from the sample impregnated at basic pH (ARG-11@MSM-1°C/min) was more limited than that observed for the carrier impregnated at acidic pH (ARG-5@MSM-1°C/min) so evidencing that the desorption was affected by the pH of the impregnating solutions. In particular, the results of the tests revealed that the sample impregnated at pH 5 released the total

amount of the loaded ARG within 10 minutes while the sample impregnated at pH 11 released a smaller amount (about 58 %) in the same time interval.

7.5 References

1. Kumar, D., Schumacher, K., du Fresne von Hohenesche, C., Grün, M. & Unger, K. . MCM-41, MCM-48 and related mesoporous adsorbents: their synthesis and characterisation. *Colloids Surfaces A Physicochem. Eng. Asp.* **187**–**188**, 109–116 (2001).

2. Mokaya, R. Improving the Stability of Mesoporous MCM-41 Silica via Thicker More Highly Condensed Pore Walls. *J. Phys. Chem. B* **103**, 10204–10208 (1999).

3. Wang, L., Qi, T., Zhang, Y. & Chu, J. Morphosynthesis route to large-pore SBA-15 microspheres. *Microporous Mesoporous Mater.* **91**, 156–160 (2006).

4. Sacramento, R. A., Cysneiros, O. M. S., Silva, B. J. B. & Silva, A. O. S. Synthesis and characterization of mesoporous materials with SBA and MCM structure types. *Cerâmica* **65**, 585–591 (2019).

5. A. Rimola, D. Costa, M. Sodupe, J.-F. Lambert, P. U. Silica Surface Features and Their Role in the Adsorption of Biomolecules: Computational Modeling and Experiments. *Chem. Rev* **113**, 4216–4313 (2013).

6. Venyaminov, S. Y. & Kalnin, N. N. Quantitative IR spectrophotometry of peptide compounds in water (H2O) solutions. I. Spectral parameters of amino acid residue absorption bands. *Biopolymers* **30**, 1243–1257 (1990).

7. Wolpert, M. & Hellwig, P. Infrared spectra and molar absorption coefficients of the 20 alpha amino acids in aqueous solutions in the spectral range from 1800 to 500 cm-1. *Spectrochim. Acta - Part A Mol. Biomol. Spectrosc.* **64**, 987–1001 (2006).

8. Gao, Q. *et al.* Amino acid adsorption on mesoporous materials: Influence of types of amino acids, modification of mesoporous materials, and solution conditions. *J. Phys. Chem. B* **112**, 2261–2267 (2008).

9. Gignone, A., Delle Piane, M., Corno, M., Ugliengo, P. & Onida, B. Simulation and Experiment Reveal a Complex Scenario for the Adsorption of an Antifungal Drug in Ordered Mesoporous Silica. *J. Phys. Chem. C* **119**,

13068–13079 (2015).

Conclusions and Outlooks

During the last decades, mesoporous silica (MS) has gained much interest in the dermatological field owing to its unique physicochemical properties and its ability in promoting blood clotting as well as wound healing.

In this PhD thesis MS spheres were chosen as materials to develop novel drug carriers for the delivery of therapeutic molecules for the treatment of wounds.

The first part of this research project focused on the development of a novel hemostatic material based on mesoporous silica (MS) loaded with tranexamic acid (TXA), which can exploit the hemostatic ability of the carrier (i.e. MS) and prevent any possible dissolution of the clot by releasing the TXA. TXA was chosen as a drug in this research activity due to its antifibrinolytic effect. To the best of my knowledge, this was the first attempt to use MS as a carrier for TXA. For this purpose, the hemostatic ability of two mesoporous silica materials with different physicochemical properties was investigated and TXA was then loaded into the carrier with the best hemostatic performance.

In particular, MSM (with an average pore diameter of 25 nm and particle size ranging from 1 to 5 μm) and SMSP (with an average pore diameter of 2.4 nm and particle sizes ranging from 0.15 to 0.80 μm) were synthesized, characterized and their hemostatic ability was assessed through a clotting blood time test. The hemostatic performance of the materials was successfully confirmed, suggesting their potential use during the management of bleeding. In particular, the study evidenced that the MSM-15°C/min sample, characterized by the largest pores and the most hydrophilic surface possessed the best hemostatic ability, in accordance with the literature. Moreover, the hemolysis assay showed that all the samples presented good hemocompatibility.

TXA was loaded into MSM-15°C/min sample, which presented the best hemostatic ability, through an incipient wetness impregnation technique. The clotting blood time test confirmed that the presence of TXA on the surface of the material did not affect its ability in inducing the activation of the coagulation

cascade. A preliminary in *vitro* release test showed that the material was able to deliver TXA to the release medium within one hour, which makes this carrier suitable to control hemorrhages during emergencies as requested by the CRASH-2 (Clinical Randomization of an Antifibrinolytic in Significant Hemorrhages-2) trial.

In conclusion, the achieved results evidence that the prepared material is promising for the development of new topical hemostats for bleeding management in emergency. However, future outlooks should consider:

- an insight into the safety of mesoporous silica-based materials in the hemostasis field, since the literature offers variable data and interpretations on this issue;
- the release of TXA in more complex systems mimicking the application conditions;
- *in vivo* test on animal models.

The second part of this PhD thesis focused on the study of the impregnation of mesoporous silica with arginine (ARG), with the goal to develop a multifunctional material for wound treatment, which combines the beneficial action of both MS and ARG. ARG, in fact, is an amino acid that may have a beneficial role in tissue repair of acute and chronic wounds.

In particular, the research work focused on the effect of the pH of the impregnating solution on the stability of the MS carrier. To this purpose, SMSP were loaded with ARG through the wet impregnation technique at different pHs (i.e., 5, 9, 10 and 11). From the results it emerged that the impregnation performed at the original basic pH of the ARG solution (i.e., pH ≈ 11) induced a significant change in the porosity and in the surface of the particles, probably due to degradation ascribed to partial silica dissolution and reprecipitation. On the other hand, the impregnation performed adjusting the pH of the ARG solution to acidic conditions (about 5) did not affect the carrier.

In order to overcome this degradation issue, MSM, which should present higher stability when compared to SMSP, was considered as an alternative carrier for the impregnation with ARG solutions (at pH 5 and 11). The results revealed that the impregnation process performed at both acidic (i.e., pH ≈ 5) and basic pH (i.e., pH ≈ 11) did not induce any significant modification of the porosity and of the surface of the particles. However, a low degree of dissolution and reprecipitation of

MSM impregnated at basic pH cannot be excluded, since the FESEM images evidenced the formation of connections and junctions between the particles.

Finally, the release of ARG was studied from both carries (i.e. SMSP and MSM) impregnated at acidic pH (i.e., pH ≈ 5) and basic pH (i.e., pH ≈ 11). The desorption tests carried out in water evidenced that ARG could be desorbed in water by all systems. A complete desorption was observed from both samples (SMSP and MSM) impregnated at pH 5, whereas the desorption appeared to be less extensive from the samples impregnated at basic conditions.

In conclusion, the outcomes indicate that MS spheres are not inert toward the loading of ARG. However, the integrity of the carrier can be controlled by controlling the pH of the impregnating solution. Future research should consider:

- the study of the *in vitro* release of ARG from the different carriers in more complex systems mimicking the application conditions;
- the investigation of the dissolution of SMSP and MSM and the delivery of orthosilicic acid $Si(OH)_4$ in simulated physiological conditions;
- the study of the ability of ARG loaded SMSP and MSM in improving the wound treatment with suitable cellular models.